DOMAIN WALLS, DEMAGNETIZING FIELDS AND ANISOTROPY IN THIN FERROMAGNETIC FILMS

Thesis by

René Clément Collette

In partial Fulfillment of the Requirements

For the Degree of

Doctor of Philosophy

California Institute of Technology

Pasadena, California

1964

ACKNOWLEDGMENTS

I thank Dr. C. H. Wilts for his most constructive advice during the course of this research and the writing of the thesis. I am also grateful to several other members of the Faculty and particularly to Dr. J. N. Franklin, Dr. F. B. Humphrey and Dr. G. D. McCann, Jr.

I owe much to the Rotary Foundation, the Belgian American Educational Foundation, the California Institute of Technology, the University of Liège, General Precision Incorporated and the Jet Propulsion Laboratory for their financial support during my stay at the Institute.

ABSTRACT

The so-called Néel walls separating antiparallel domains in very thin ferromagnetic films are found, on the basis of accurate calculations, to have a shape differing significantly from the linear rotation model suggested by Néel. In this 180° rotation, three regions can be distinguished: a central one where the magnetization $\vec{M}$ rotates rapidly (positive demagnetizing energy) and two adjacent regions extending in the neighboring domains where the rotation is very much slower. In these "tail" portions of the curve, the direction of $\vec{M}$ is determined mostly by a balance between the anisotropy torque and the torque due to the internal field. The calculations have been performed for permalloy films with thicknesses ranging from 0 to 200 Å. The walls extend up to several microns, in each of the adjacent domains (of the order of 15μ at a thickness of 200 Å).

As a continuation of the study of infinite Néel walls, the case of double walls (360° rotation) and of cross-tie walls is also analysed on a semiquantitative basis. The main characteristics of these two configurations can be explained on the basis of the new model found for the pure Néel walls.

In a second section, the internal demagnetizing field H_i is calculated as a function of the shape, the thickness and the

edge profile of the film. Along the edges perpendicular to the easy direction, the growth of peaks of reverse magnetization is studied when the external field varies. Also the detailed configuration of the internal field at the edge is found to depend strongly on the profile of the latter. By varying the slope of a tapered edge, it is shown that $(H_i)_{max}$ can be reduced to such a small value that nucleation will take place only at an external field larger in absolute value than the normal coercive force of the film. Thus the hysteresis curve along the easy direction is noticeably altered and very square.

In a third section, an instrument is presented for the study of the magnetic anisotropy in the plane of the film. This apparatus is particularly suitable for determining the anisotropy field, the single domain state being preserved at all times.

TABLE OF CONTENTS

TABLE OF CONTENTS (continued)

1. INTRODUCTION

The principles of domain theory in ferromagnetism have been established by Weiss (1) more than half a century ago. Later, Bloch (2) showed that two adjacent domains are separated by a region of finite thickness, called a wall, where the magnetization must rotate continuously (actually, in small finite steps from one lattice site to the next) from its direction inside one domain to its direction inside the other. Direct experimental observation, with the Bitter technique (3) for instance, has been very difficult for bulk material since phenomena could only be viewed at the surface. Not only is the preparation of one sample long and delicate, but surface rather than volume effects are observed, the former being quite influenced by demagnetizing fields.

In 1955, however, Blois (4) reported the method he had developed to prepare ferromagnetic thin films. Since then, at least in these films, our understanding of detailed processes such as wall motion, flux reversal, variations of domain configuration, and others has greatly improved, principally because the shape and the surface

of the sample are such that direct observation is very much facilitated. Such a contribution to our scientific knowledge is in itself worth the work invested. Furthermore, Permalloy 80 exhibits particularly interesting properties and intensive research has been conducted with the hope of reaching promising industrial applications. The speed of magnetization reversal was found to be of the order of a few nanoseconds (10^{-9} sec) with a drive field of only a few oersteds (5, 6). Such a switching time would permit the design of computer memories and logical circuits significantly faster than those using ferrite cores and requiring at the same time a moderate power to drive the lines. Furthermore, the building of memory arrays made of superimposed circuits would then be possible through successive evaporations of conducting, insulating and ferromagnetic materials. Such fabrication process could be highly automated. Compactness and light weight would also be attained. Worldwide efforts, carried out during these last eight years, have already produced commercial and experimental memories made of ferromagnetic films.

Much experimental work has been accumulated, but, from the scientific point of view, data still present appreciable scattering so as to render difficult quantitative conclusions. This lack of reproducibility is due to irregularities in the physical, geometrical and chemical structures of films. Sometimes it has not even been possible

to relate variations of a given property with one or several types of clearly identified imperfections. Fabrication of films with characteristics that are uniform and predetermined with precision has thus not been easy so far. Important parameters in the preparation of films are either insufficiently controlled or improperly chosen, or probably even unrecognized and therefore ignored.

Little theoretical work has been done to successfully explain the accumulated data. A clearer understanding of events would certainly be useful in determining possible modifications to be brought in the fabrication techniques. Small-scale investigations and calculations are promising, since variations of structure and changes in magnetization direction occur over small distances of the order of a few hundred Angstroms or so.

The fundamental property of polycrystalline Permalloy films is the uniaxial magnetic anisotropy induced during deposition. The component parallel to the substrate of a uniform field present during evaporation determines the axis of preferred magnetization when the incident beam of atoms is perpendicular to the plane of the layer. The role of this external field is simply one of orientation: it aligns the "easy axis" parallel to the same direction everywhere. The origin

of the anisotropy is not understood yet and several theories have been proposed (7). Magnetic anisotropies (crystalline, magneto-elastic, etc.), although their origins are not known with certainty, depend upon the configuration and the deformation of the lattice and are the result of an interaction between this lattice and the atomic magnetic moment. Such an interaction is thought to be due to the spin-orbit coupling inside one atom and the quenching of its electron cloud by crystalline electric fields and overlapping with neighboring clouds (8).

Supposing that the actual explanation of the uniaxial anisotropy is indeed a spin-lattice interaction, which is likely to be the case, it seems relevant to remark the following. In the case of thin films deposited by evaporation or by electrolytic process (9), at all times during the formation of the sample, the magnetization oriented by the external field points in the same direction; thus, when an incident atom attaches itself to the surface of the film, its magnetic moment aligns with the neighboring spins along that direction; at that time, the spin-lattice interaction, presumably responsible for the anisotropy, becomes effective and the new atom will position itself in the surface layer of the crystal in such a way as to minimize the spin-lattice energy, whatever the latter is. Indeed, the incident atom, being for a fraction of a second with neighbors on one side only, is free to adjust distances between it and the underlying atoms. The technique

of fabricating films is unique in the sense that atoms, being deposited one at a time, have a chance to reach a higher order of arrangement under the influence of the magnetization $\vec{M}$. That the direction towards which the magnetic moments point during deposition represents a minimum of energy and becomes an axis of preferred magnetization is not entirely surprising.

As mentioned earlier, investigation of phenomena at a small scale is necessary in further studies of film properties and Chapters 3, 4 and 5 are examples of the importance of studying internal field configurations as rigorously as feasible. The detailed analysis of such fields has always been neglected, thus leaving some problems misunderstood or erroneously described quantitatively. Such is the case of Néel walls studied in Chapter 3, whose actual shape, largely determined by the internal field, is quite different from that deduced from approximate calculations, which up to now was considered valid by most workers. Internal fields also account for the configuration and dimensions of the so-called cross-tie walls reviewed in Chapter 4. Finally, in Chapter 5, investigation of the field at the very edge of the film suggests that its value, normally of the order of a few hundred oersteds in a 2000 Å film, can be significantly decreased to the point of altering the overall behavior of the magnetization of the film in the presence of an external field.

Chapter 6 describes an instrument, whose principle has been thought of in the course of the work at this Institute, and which might be helpful in the study of the anisotropy of films or, more generally, of their behavior in dc fields. In some instances, it could be used instead of a torquemeter for determining the magnetic anisotropy of a sample. Its most advantageous features are simplicity and low cost of fabrication.

The literature relative to Permalloy films is extensive and also quite dispersed. Goodenough and Smith (10) have published in 1959 a review on the matter and Middelhoek (11), in his thesis on "Ferromagnetic Domains in Thin Ni-Fe Films" (1960), has also described in great detail various aspects of the statics of films. These two publications provide a convenient introduction to the subject, as well as descriptions of various experimental techniques.

The method of preparation of the films reported in the experimental sections of this work is essentially similar to that described by Blois. The deposition is performed in a vacuum of 10^{-6} mm Hg, measured before the actual evaporation starts. The Permalloy slug, heated by induction, is briefly degassed in a preliminary step. Glass, cleaned chemically and ultrasonically, is used as a substrate and is heated to 300°C during deposition. This simple fabrication procedure is satisfactory for the qualitative

examples presented in Chapters 4, 5 and 6. However, it should be emphasized that, for a study of film structure or reproducibility of results, more elaborate techniques should be used, such as thorough degassing of the substrate as well as of the walls and materials inside the vacuum chamber, annealing of the film after deposition. These additional steps tend to eliminate structural abnormalities and foreign chemicals that might contaminate the film and appreciably alter its characteristics. On the other hand, it does not seem that a higher vacuum is necessary.

2. BASIC CONCEPTS AND FORMULAS

Unless otherwise indicated, the rationalized MKSA system is used throughout.

2.1 Magnetization and Magnetic Poles

The magnetization $\vec{M}$, a vector of constant amplitude characteristic of a ferromagnetic material, represents the total magnetic moment per unit volume. It is treated as a continuous function although, in fact, neighboring atoms are separated by finite distances. Whenever the $\vec{M}$ field is not a uniform one, by analogy with electrostatics, a volume density of magnetic poles may be defined as:

$$\rho(x,y,z) = -\operatorname{div} \vec{M} = -\frac{\partial M_x}{\partial x} - \frac{\partial M_y}{\partial y} - \frac{\partial M_z}{\partial z} \qquad (2.1\text{-}1)$$

This quantity ρ has no physical reality or meaning but is a convenient mathematical device.

2.2 Exchange Energy and Torque

The alignment of neighboring magnetic moments in the ferromagnetic crystal, giving rise to a non-zero macroscopic magnetization, is forced by the so-called exchange interaction of the electron

clouds. With this interaction is associated a potential energy which is minimum when the moments are parallel to each other. This "exchange energy" density will then be a function of the spatial variations of the vector $\vec{M}$. The three-dimensional expression adopted by Landau and Lifshitz (12) to describe this energy is:

$$\varepsilon_{ex} = A[\,(\text{grad}\,\alpha_1)^2 + (\text{grad}\,\alpha_2)^2 + (\text{grad}\,\alpha_3)^2\,]\,.$$

α_1, α_2 and α_3 being the direction cosines of $\vec{M}$. The exchange coefficient A is a constant for a given material. In the case of the unidimensional problem shown in figure 2-1, it reduces to :

$$\varepsilon_{ex} = A\left(\frac{d\theta}{dy}\right)^2 \qquad (2.2\text{-}1)$$

where θ is the angle between $\vec{M}$ and the x axis (Fig. 2-1).

Whenever $d\theta/dy$ itself varies with y, an "exchange torque" per unit volume is applied to the magnetization $\vec{M}$. It is obtained by differentiating (2.2-1) with respect to θ :

$$T_{ex} = 2A\,\frac{d^2\theta}{dy^2} \qquad (2.2\text{-}2)$$

2.3 Internal Field and Magnetostatic Energy

The internal field $\vec{H}_i$ originating in a ferromagnetic body is easily deduced from the Maxwell equation governing the magnetic induction. Indeed, with no external field applied, one has:

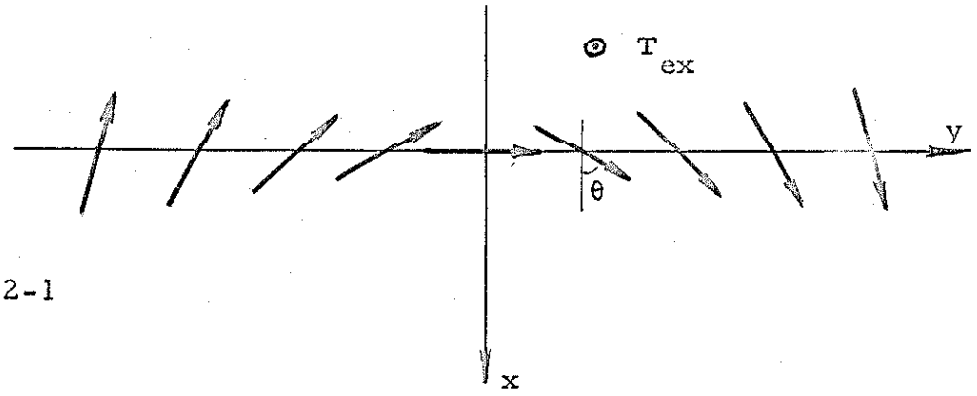

Fig. 2-1

Unidimensional variation of $\vec{M}$ in the plane (x,y)

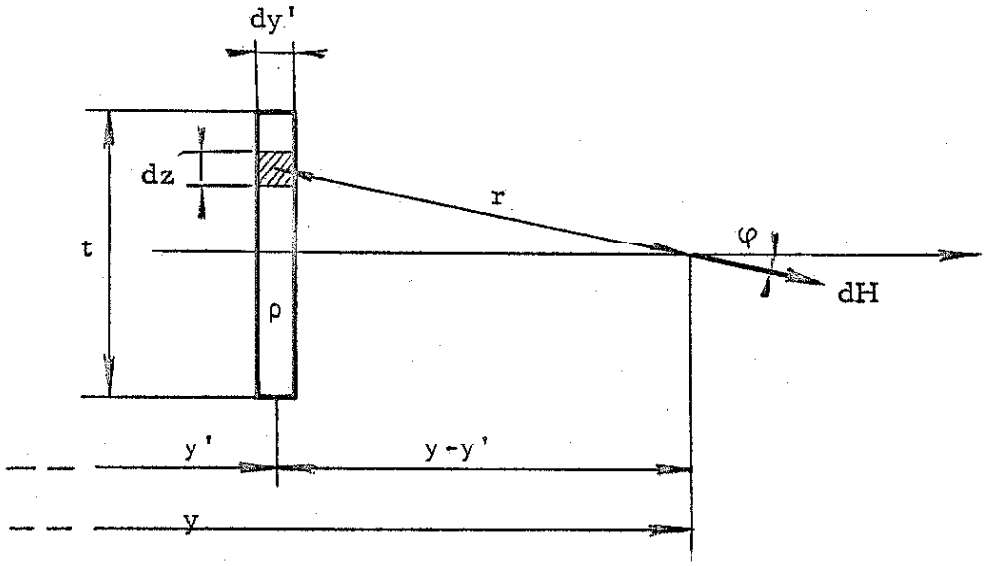

Fig. 2-2

Field due to a slice of poles of cross-section t dy' and infinite in the x direction

$$\vec{B} = \mu_o (\vec{H}_i + \vec{M})$$

$$\text{div } \vec{B} = \mu_o (\text{div } \vec{H}_i + \text{div } \vec{M}) = 0$$

$$\text{div } \vec{H}_i = - \text{div } \vec{M} = \rho (x, y, z)$$

Thus the formal analogy between magnetostatics and electrostatics is complete if the electric displacement and charge density are replaced respectively by the magnetic field and pole density. The following formulas will be needed in the remainder of this work; ρ, σ and λ designate volume, surface and line densities of poles.

Field, at location y, due to an infinite line of pole density, λ, parallel to the x axis, and located at y':

$$H_y = \frac{\lambda}{2\pi (y - y')} \quad \text{with } \lambda = \sigma \, dy = \rho \, dy dz \tag{2.3-1}$$

Field, at y, due to an infinite slice of poles of cross section t dy' parallel to the x axis and located at y'(as indicated in Fig. 2-2):

$$H_y = \int_{-t/2}^{t/2} \frac{\rho \cos \varphi \, dy' \, dz}{2\pi r}$$

$$= \frac{\rho dy'}{\pi} \arctan \left[\frac{t}{2(y - y')} \right] \tag{2.3-2}$$

Field, at y, due to an infinite line of dipoles along the x axis, of strength $\mathfrak{M}$ per unit length and parallel to the y axis:

$$H_y = \frac{\mathfrak{M}}{2\pi y^2} \tag{2.3-3}$$

Field, at a distance r, due to a pole density ρ at the origin:

$$H_r = \frac{\rho \, dx \, dy \, dz}{4\pi r^2} \tag{2.3-4}$$

A magnetic potential V can be used to describe this field. Thus:

$$V = \frac{\rho \, dx \, dy \, dz}{4\pi r} \tag{2.3-5}$$

with $H_r = -\text{grad } V = -\frac{dV}{dr}$.

The self-energy per unit volume of material is

$$\epsilon_m = -\frac{\mu_o}{2} \vec{M} \cdot \vec{H}_i \tag{2.3-6}$$

Because the field against which the work is done is of internal origin, the usual factor of one-half is included.

The corresponding torque per unit volume is:

$$T_m = \mu_o \vec{M} \times \vec{H}_i \tag{2.3-7}$$

Whenever the total field at one point is the sum of a non-zero external component $\vec{H}_{ex}$ and an internal one, $\vec{H}_i$, the energy and torque per unit volume are:

$$\epsilon_m = -\mu_o \vec{M} \cdot (\vec{H}_{ex} + \vec{H}_i/2) \tag{2.3-8}$$

$$\vec{T}_m = \mu_o \vec{M} \times (\vec{H}_{ex} + \vec{H}_i) \tag{2.3-9}$$

2.4 Anisotropy Energy and Torque

Permalloy films deposited in vacuo under conditions such as those reported by Blois (4) are anisotropic. There exists an "easy direction" in the plane (x,y) of the layer to which the magnetization will be parallel if no torque is applied to the $\vec{M}$ vector. This phenomenon is described by an anisotropy function or potential energy density $\epsilon_a = f(\theta)$, where θ is the angle between $\vec{M}$ and the easy axis (x axis). In the case of single domain films, various experiments can be used (13)(Chapter 6) to determine the anisotropy function. Most often it is approximated quite well by the function which describes the Stoner-Wohlfarth model (14):

$$\epsilon_a(\theta) = K \sin^2\theta \qquad (2.4\text{-}1)$$

This function presents two identical minima at $\theta = 0$ and π as expected. An "anisotropy torque" per unit volume appears when $\sin\theta$ differs from zero and one:

$$T_a = - K \sin 2\theta \qquad (2.4\text{-}2)$$

A high geometrical anisotropy exists perpendicular to the plane (x,y) of the film. Indeed, the z component of the internal field is equal to $-M_z$ in a single domain. When a single domain in such a film is under the influence of an external field $\vec{H}$, the equilibrium between the magnetostatic and anisotropy torques will determine the steady-state orientation of the magnetization $\vec{M}$.

If such a field were applied along the z direction, the angle θ between $\vec{M}$ and the easy axis would be determined by setting $\vec{T}_m$ equal to zero in equation (2.3-9), neglecting the anisotropy torque:

$$\mu_o M (H_z - M \sin \theta) \cos \theta - 0$$

or $$\sin \theta = \frac{H_z}{M} \quad .$$

Thus, H_z being in all practical cases negligible compared to M, the $\vec{M}$ vector will stay in the plane (x,y).

If the field is applied along the "hard direction" (y axis) in the plane of the layer as in Figure 2-3, formulas (2.3-7) and (2.4-2) give:

$$T_m + T_a = \mu_o M H_y \cos \theta - K \sin 2\theta = 0$$

that is: $$\sin \theta = H_y / H_k \qquad \text{for } H_y \leq H_k \qquad (2.4\text{-}3)$$

$$\sin \theta = 1 \qquad \text{for } H_y > H_k$$

where

$$H_k = \frac{2K}{\mu_o M} \qquad (2.4\text{-}4)$$

The quantity H_k, characteristic of a particular film, is referred to as the anisotropy field.

In the more general case where $\vec{H}$ makes an angle α with the easy axis, the equilibrium is expressed by the following relationship:

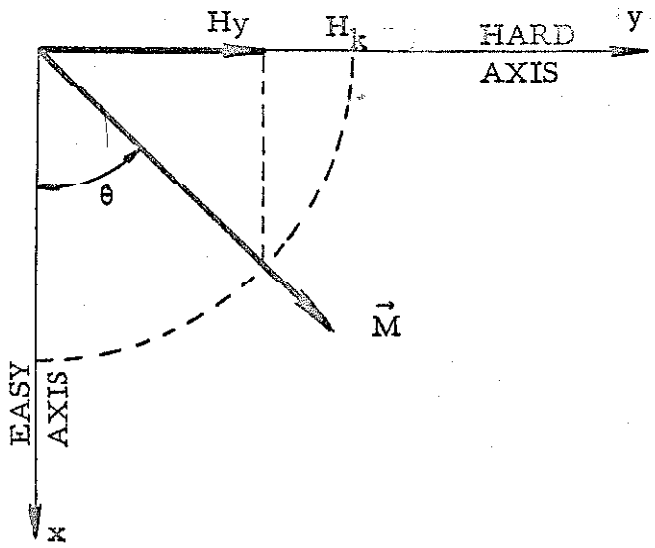

Fig. 2-3

Variation of $\vec{M}$ with the field applied along the hard axis

$$\mu_o M H \sin(\alpha-\theta) = K \sin 2\theta \qquad (2.4\text{-}5)$$

Figure 2.4 is a graphical interpretation of this equation which can be rewritten:

$$h_y - h_x \tan\theta = \sin\theta \quad \text{where } h = H/H_k$$

The curve θ = constant in the plane (h_x, h_y) is a straight line whose slope is $\tan\theta$, cutting the h_y axis at $\sin\theta$ and which is limited by a critical curve, the boundary between the regions of stability and instability. The mathematical expression of this curve (astroid) is a well-known result (15), and it can be written as follows:

$$(h_x)^{2/3} + (h_y)^{2/3} = 1 \qquad (2.4\text{-}6)$$

Inside the astroid, at point A for instance, two states of equilibrium are possible: θ_1 and θ_2. Outside that region, one stable state only exists.

The exact origin of the anisotropy in Permalloy films has not been determined yet with any certainty. However, it is presumably a short-range interaction depending on the direction of the magnetic moment at the site considered as well as its immediate neighbors. Therefore, it may be assumed that expression (2.4-1), true for single domains, is still a very good approximation when $\theta(y)$ varies, provided the increment $\Delta\theta$ from one lattice site to the next is very small.

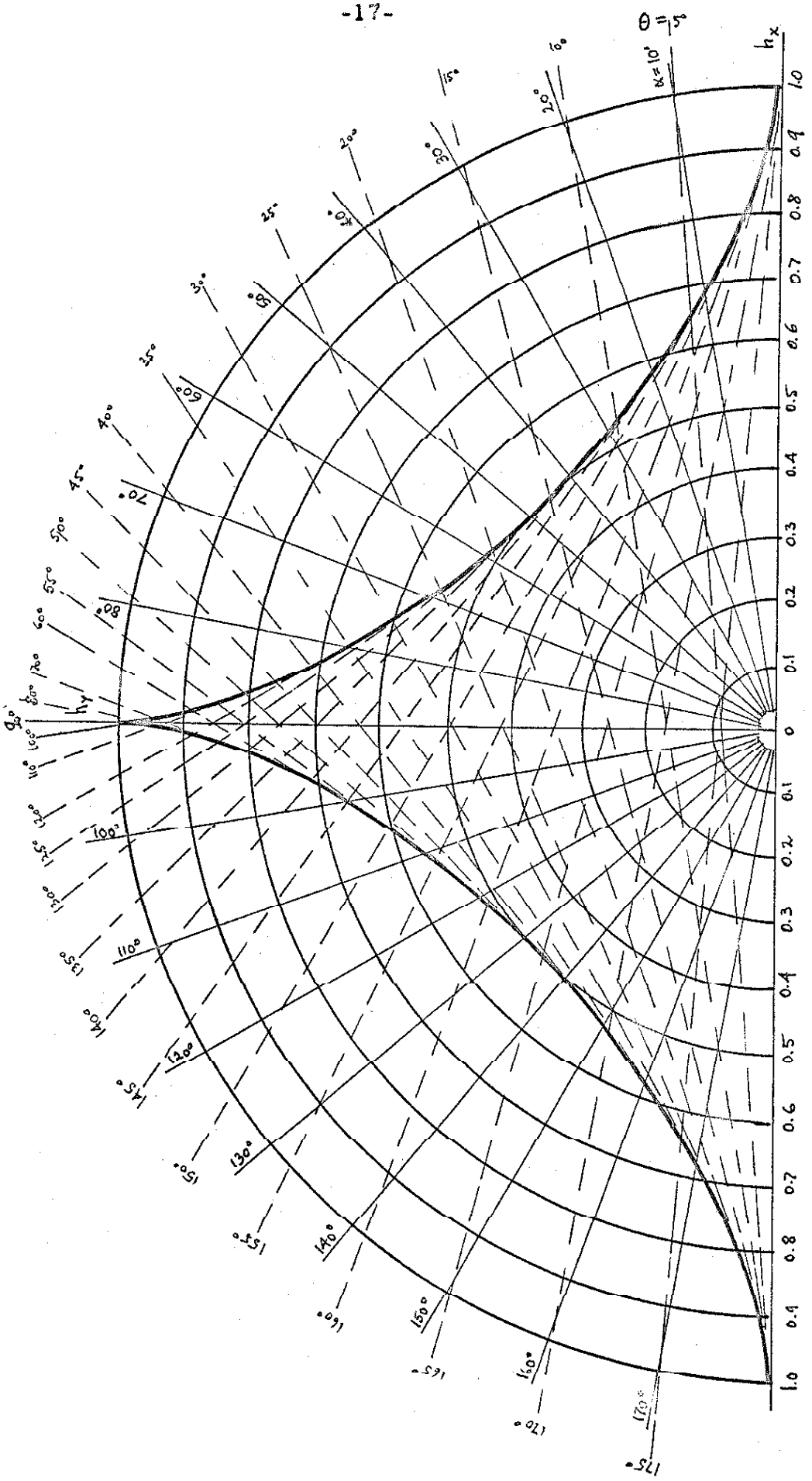

Fig. 2-4 Polar diagram of the reduced field h showing the value of the angle θ at equilibrium

2.5 Units of Physical Quantities and Constants

Quantity	Symbol	MKSA Unit
Magnetization	M	Amp. turn/meter
Magnetic Field	H	At/m (1/79.5 oersted)
Magnetic Induction	B	Weber/m^2 (10,000 gauss)
Pole density	ρ	At/m^2
Exchange Coefficient	A	Joules/m
Anistropy Coefficient	K	J/m^3
Permeability in vacuo	μ_o	$4\pi \cdot 10^{-7}$ Henry/m

3. SHAPE AND ENERGY OF NÉEL WALLS

3.1 Néel, Bloch and Cross-tie Walls

The shape of a wall separating two domains in a ferromagnetic body, with no external field applied, is very much dependent on the internal magnetostatic field configuration. Indeed, high concentrations of magnetic poles inside or at the surface of the volume where the rotation of magnetization occurs, can produce large fields that may reach values approaching M itself. In many cases, a sizable, if not a major, part of the total energy stored in the wall is magnetostatic. Consequently, a great deal of information can often be obtained by analyzing that single term first. For instance, a simple inspection of the internal magnetostatic energy permits the determination of the general form of the wall in two trivial cases:

(1) bulk material where two domains, with their axes of magnetization parallel and antiparallel to some direction, say the x axis, are separated by a wall situated in the plane (x, z);

(2) an infinitely thin layer (in the x, y plane) with two domains with magnetization lying in the plane of the film and separated by a wall parallel to the x axis.

In the first example, Figures 3-1a and b represent two possible extreme situations. Configuration (a) has no magnetic poles ($\text{div } \vec{M} = 0$), thus the internal field is zero throughout the material, whereas configuration (b) produces a field $H_y = - M_y$.

In the case of an infinitely thin film and the arrangement of Figure 3-2a, although the volume pole density, $\rho = - \text{div } \vec{M}$, is not zero, the total amount of poles, and therefore the field, are proportional to the thickness t, and thus tend towards zero with it. However, in Figure 3-2b, the poles appear at the surfaces only, and are now independent of t; there the amplitude of the internal field is $H_z = -M_z$.

It can then be concluded immediately that the stable walls are those of Figures 3-1a and 3-2a, having a magnetostatic energy density which is zero everywhere. These are called in the literature, respectively, Bloch and Néel walls, and have been studied by Landau and Lifshitz (12, 16), and by Néel (17).

By extension, a Néel-type wall in a film is one where the $\vec{M}$ vector rotates in the plane (x, y) of the layer. In a Bloch-type wall, $\vec{M}$ goes out of that plane. Néel (17), who pointed out the existence of both types of walls in thin films, established some very approximate formulas for their respective energy content in the case of a 180° rotation. He predicted a transition thickness t_c, below which the Néel walls would replace the Bloch walls. Due to his extreme

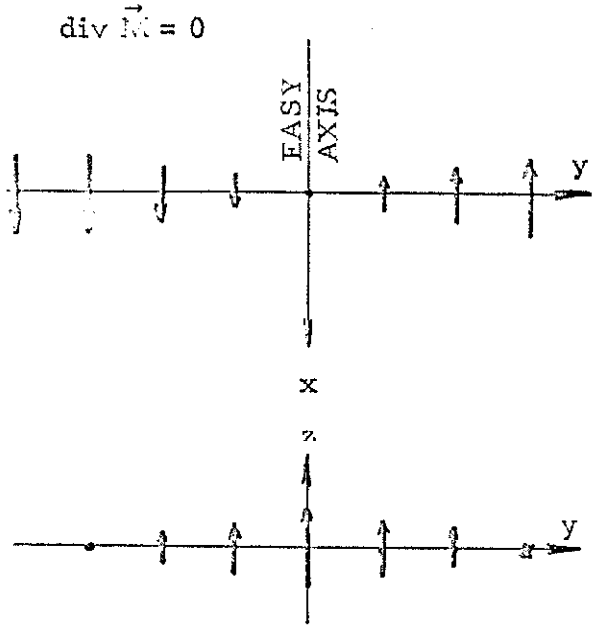

Fig. 3-1a

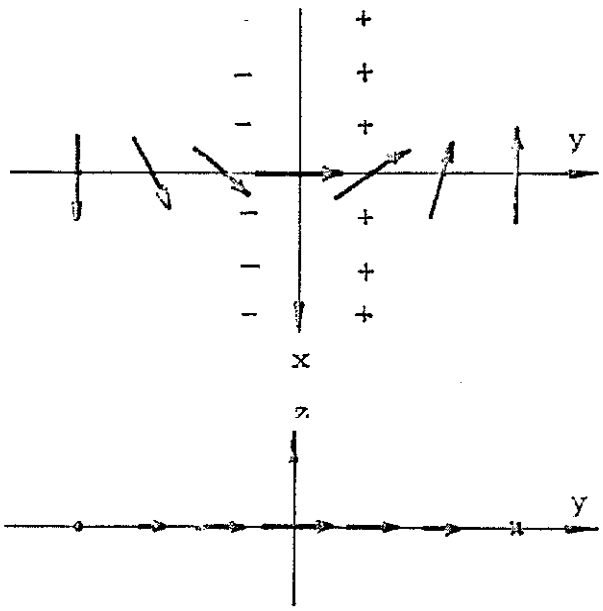

Fig. 3-1b

Two possible configurations of a wall in bulk material

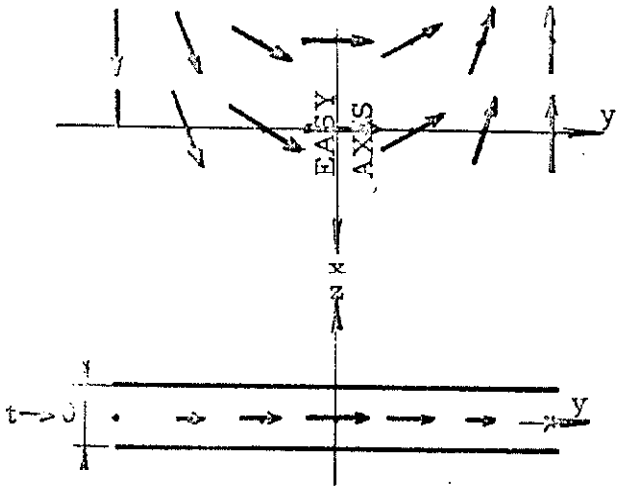

Fig. 3-2a

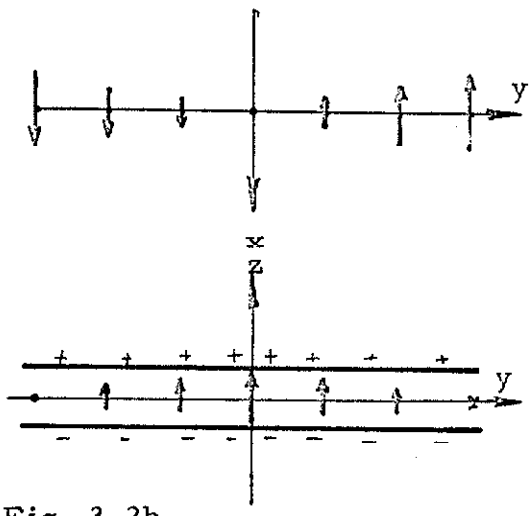

Fig. 3-2b

Two possible configurations of a wall in an infinitely thin film.

simplification of the calculations, no accuracy can be claimed in the determination of t_c. Its order of magnitude is several hundred Angstrüms. Figure 3-3 reproduces Néel's original results.

A third unpredicted type of wall, called "cross-tie," was observed by Huber, Smith and Goodenough (18) in films of intermediate thickness, approximately in the range where t_c was expected to fall. They proposed and Moon (19) demonstrated that these cross-ties were in fact closely related to Néel walls because, in their case also, the magnetization rotates in the plane of the layer. Thus, the critical thickness t_c, introduced theoretically, is fictitious and has no experimental counterpart, since actually two critical points exist rather than one: t_{c1}, transition between the Néel and cross-tie configurations, and t_{c2} between the cross-tie and Bloch configurations. Figure 3-4 explains the situation schematically and shows that t_c may be quite different from t_{c2}, although some authors have tried to reconcile a calculated t_c with an observed t_{c2}.

3.2 The Ritz Method for Determining the Energy and Size of Walls

A general expression for the rotation of $\vec{M}$ is chosen where one parameter is left undetermined and, on that basis, the total energy is evaluated and minimized with respect to that parameter. Evidently the function describing the rotation through the wall must be reasonably simple in order to make the analysis possible.

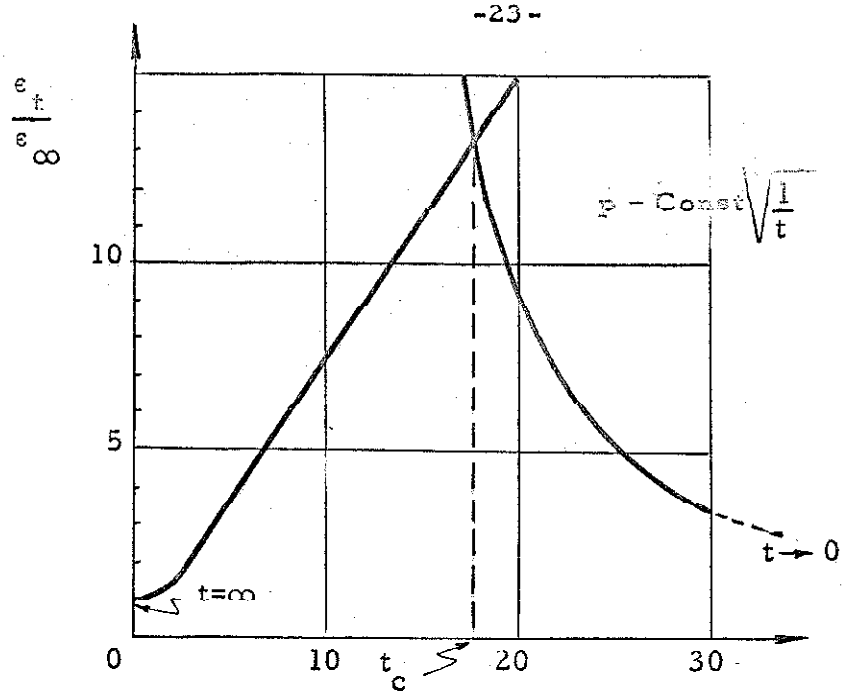

Fig. 3-3

Néel's calculation of the energy of Bloch and Néel walls in thin films

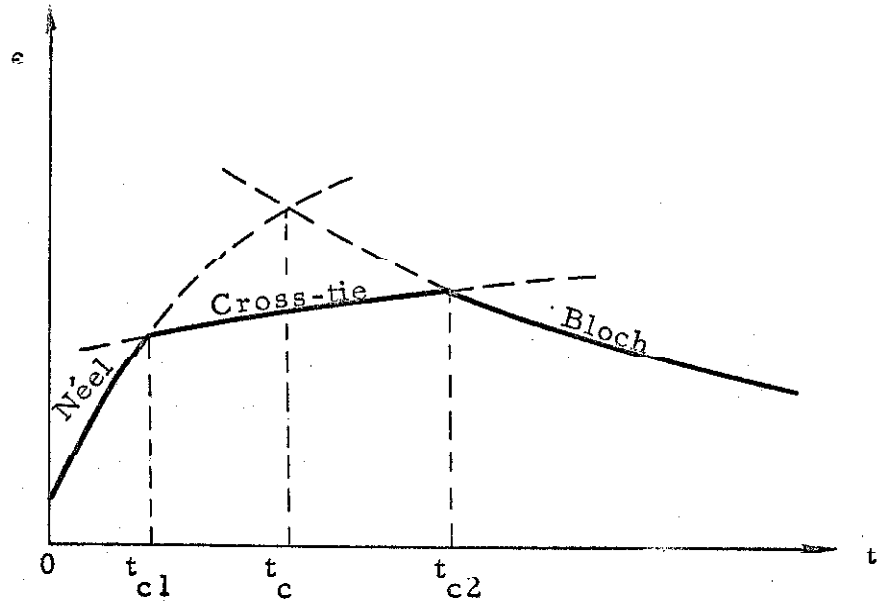

Fig. 3-4

Comparative energy densities of Néel, Cross-tie and Bloch walls

Several authors (20, 21), after Néel, have worked out the problem along this line, introducing some modification but without obtaining results significantly new. A detailed presentation of Néel and Bloch walls has been given by Middelhoek (11). His assumptions and findings are the following in the case of the Néel configuration. Figure 3-5 indicates the assumed rotation of $\vec{M}$ between two anti-parallel domains: the angle θ is presumed to vary linearly from 180° at y = -a to 0° at y = a. The variable parameter is $\underline{a}$, the width of the wall being 2a for a 180° rotation. The exchange and anisotropy energies E_{ex} and E_a are then easily determined. The magnetostatic energy E_m is approximated by introducing an additional assumption: E_m is equivalent to the energy contained in a ferromagnetic elliptical cylinder of half axes t/2 and $\underline{a}$, magnetized along the y direction, the amplitude of the uniform magnetization being $M/\sqrt{2}$. Thus:

$$E_m = \frac{\mu_o}{2} \cdot \frac{t}{t + 2a} \cdot \frac{M^2}{2} .$$

By minimizing the sum $E = E_a + E_m + E_{ex}$, the value of $\underline{a}$ is obtained which determines the energy E per unit length of wall as well as the width for a given thickness. Figure 3-6 shows the variations of the wall width 2a and surface energy density $\gamma = E/t$, as functions of t in a film where $\mu_o M = 1\ Wb/m^2$, $A = 10^{-11}\ J/m$, and $K = 100\ J/m^3$. (These values are typical of an 80 Permalloy film deposited by vacuum evaporation on a 300°C glass substrate.)

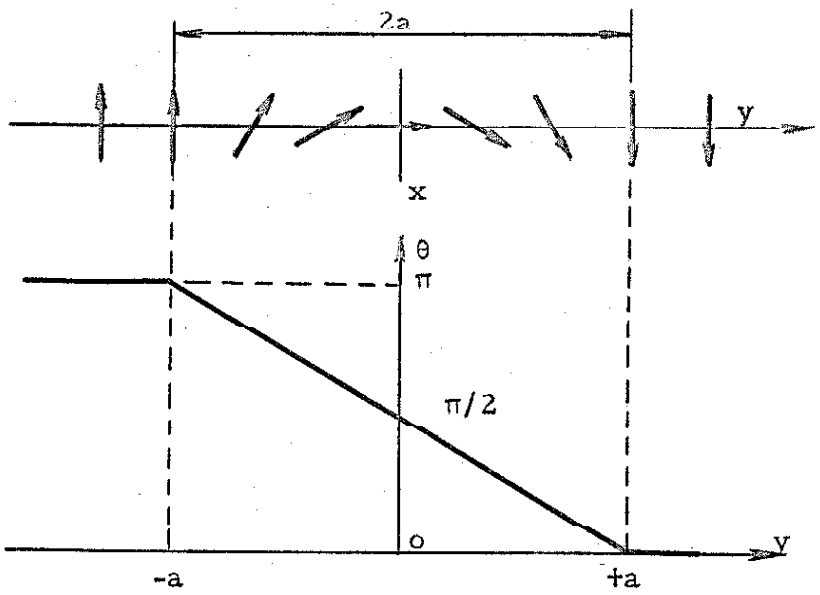

Fig. 3-5

Néel's model for the rotation of $\vec{M}$ in the plane of the film

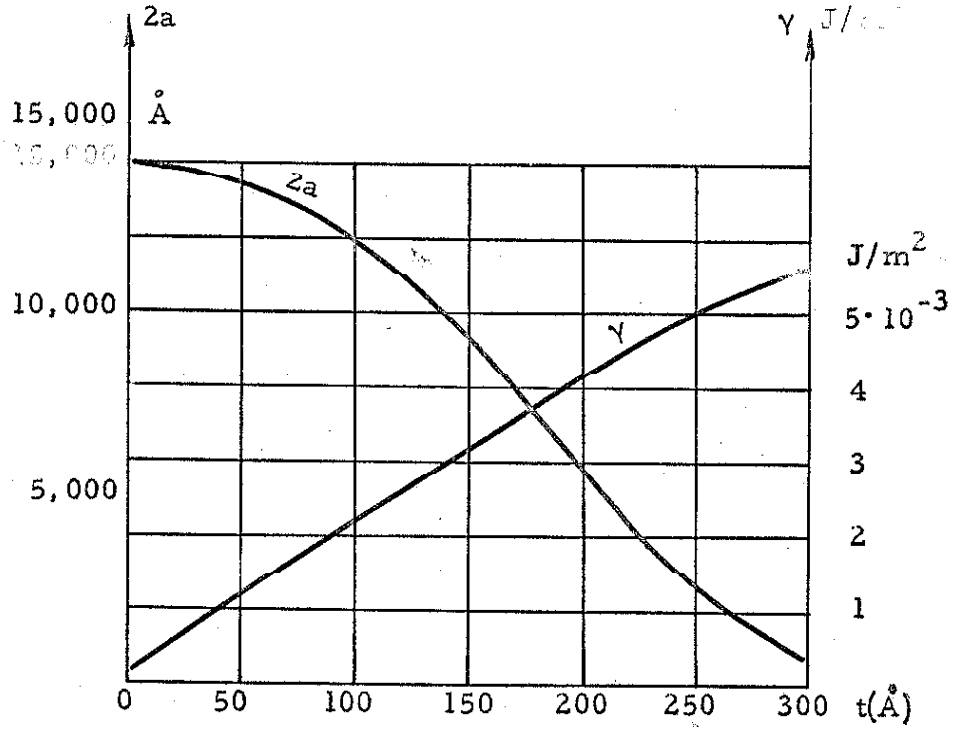

Fig. 3-6

Width and energy density of Néel's walls according to the Néel model of linear rotation (as calculated by Middelhoek)

At $t = 0$, the width $2a_o$ is, of course, equal to the value found for bulk material (Bloch wall of Fig. 3-1a), since the internal magnetostatic energy is zero in both cases. Thereafter, for increasing thickness, it is found that the width of the wall decreases. The energy density increases, of course, up to the critical thickness t_{c1}, where cross-tie walls become more favorable.

The Ritz method is useful in determining the order of magnitude of the total energy stored in a Néel wall, but as far as its dimensions are concerned, it certainly proves to be unsatisfactory, as will be shown in the remainder of this chapter. The function describing the rotation of $\vec{M}$ is actually the solution of a differential equation, whereas the energy is the result of an integration. A differentiation process is indeed more sensitive to errors made in approximating the problem.

The case of 180° Néel walls, appearing in very thin films between the thicknesses 0 and t_{c1} (of the order of 200 Å), will be analyzed in the present study. In this configuration (Fig. 3-7a), the internal field in the plane $z = 0$ is directed along the y axis and exerts an appreciable torque on $\vec{M}$ compared to the anisotropy torque. The cross-tie walls, because of their complex structure, do not permit a simple yet accurate quantitative treatment leading to the prediction of t_{c1} and t_{c2}. They will be discussed in Chapter 4 in the light of the findings concerning the strictly unidimensional Néel

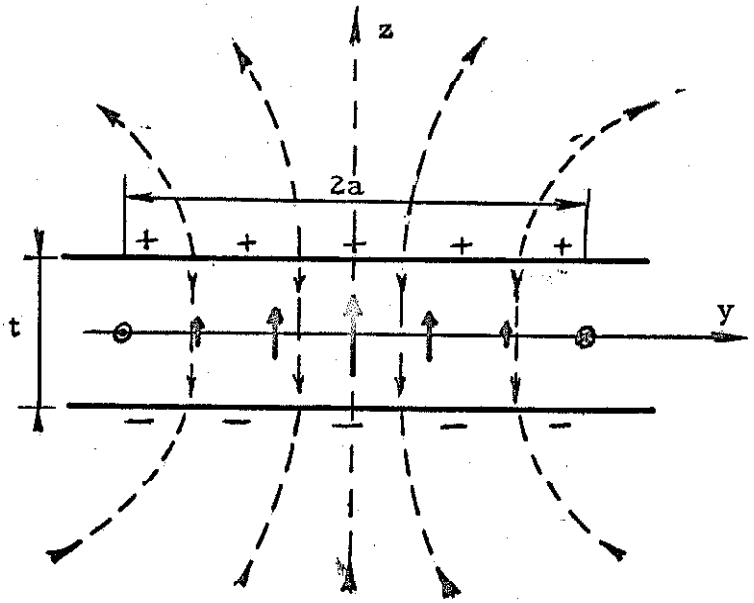

Fig. 3-7b

Internal field of a Bloch wall

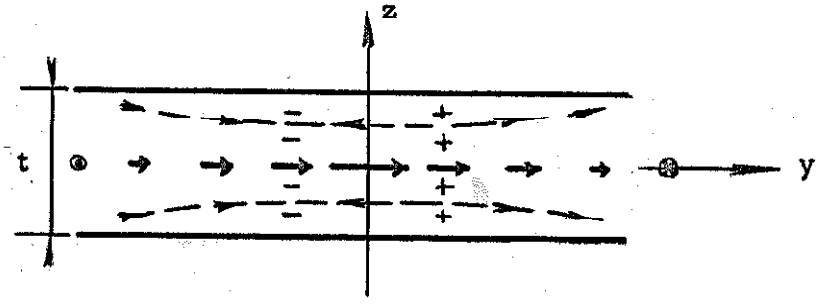

Fig. 3-7a

Internal field of a Néel wall

walls. As for the Bloch walls in thicker films, the demagnetizing field outside the wall itself is perpendicular to the plane (x,y) and has very little influence on the direction of magnetization because of the geometrical anisotropy in the z direction (Fig. 3-7b). Their characteristics were determined rather satisfactorily by the Ritz method.

3.3 Internal Field in a Néel Wall

Based on the model used by Néel, on the one hand, and the anisotropy property of the material on the other, a simple analysis shows a grave inconsistency between the function $\theta(y)$, chosen to represent the variation of the direction of $\vec{M}$, and the internal field $\vec{H}(y)$ due to the poles of density $\rho = -\text{div}\,\vec{M}$, appearing within the interval -a to +a. Figures 3-8a, b and c show the functions $\theta(y)$, $\rho(y)$ and $H(y)$ in the plane of the film. The wall is infinite along the x axis. Away from the center of the wall, at a distance 2a and farther, the field distribution is almost equivalent to that of an infinite line of dipoles of approximate strength Mta per unit length. Thus, according to the linear rotation hypothesis, $H(y)$, in that region, would be (from eq. 2.3-3):

$$H(y) \simeq \frac{Mta}{2\pi y^2} \qquad (3.3\text{-}1)$$

The wall being parallel to the easy direction of the material, the y axis represents the hard direction along which this field is applied. In a film where the anisotropy energy function is $K \sin^2\theta$ (eq. 2.4-1), neglecting the exchange torque as a first approximation, the

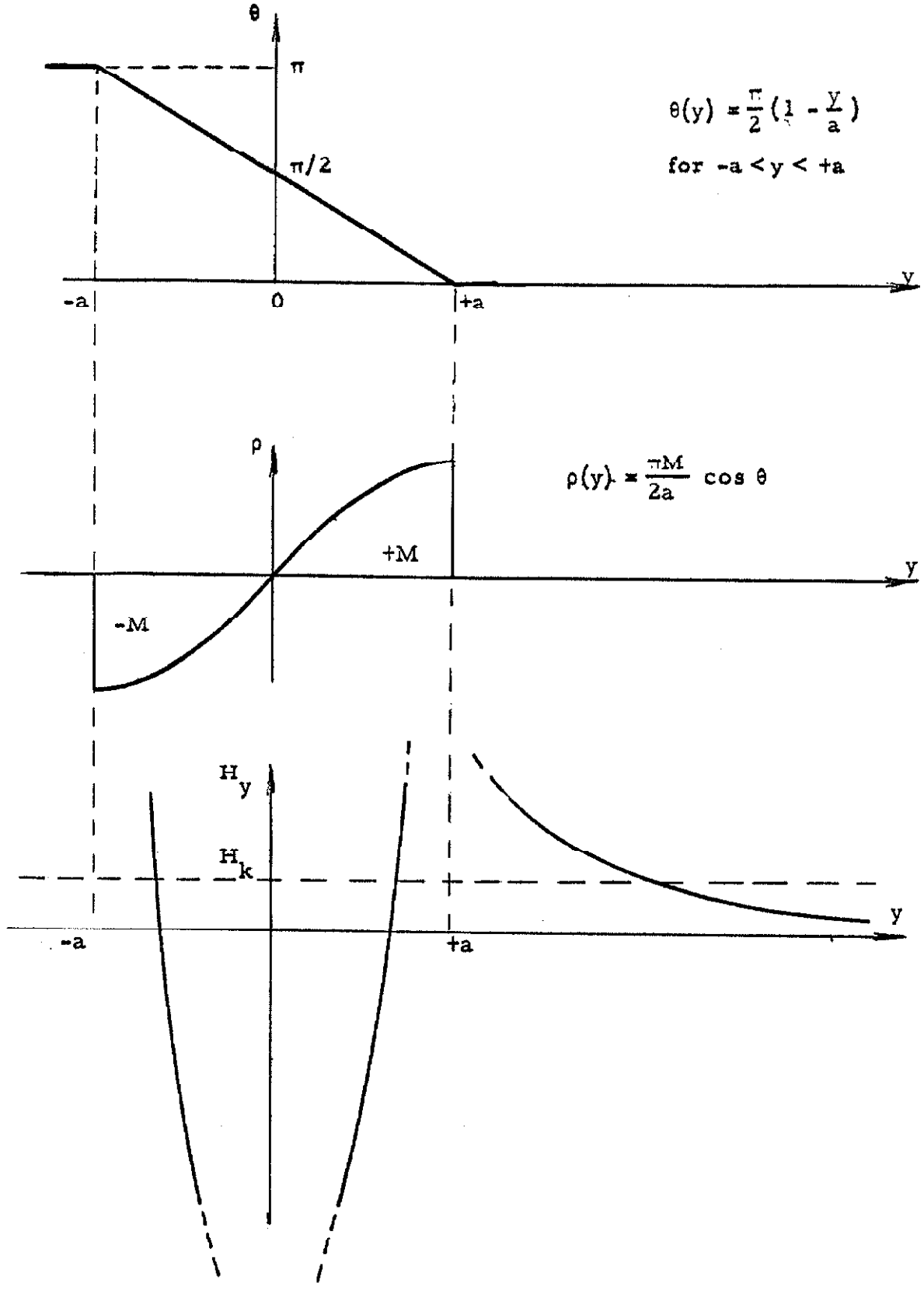

Fig. 3-8 Behavior of the internal field along the hard direction as deduced from Néel's model

equilibrium direction θ of the vector $\vec{M}$ under such a field is given by the relationship 2.4-3, which becomes $\theta = \pi/2$ when $H(y) > H_k$. But, in the present model, sin θ equals zero wherever $|y| \geq a$; this sine value is only compatible with a zero field in the y direction. Quite to the contrary, the calculated field reaches high values. For instance, at t = 100 Å , the value of a is 6000 Å (from Fig. 3-6), and at a distance 2a from the x axis, H(y) would be equal to (from eq. 3.3-1):

$$H(2a) \simeq \frac{Mt}{8\pi a} = 530 \text{ At/m} ;$$

whereas (from eq. 2.4-4):

$$H_k = \frac{2K}{\mu_o M} = 200 \text{ At/m} .$$

Clearly, the function $\theta(y)$ and $H(y)$, in the case of the Néel model, are in contradiction; the linear rotation assumption is therefore quite invalid.

This brief analysis of the internal field suggests, however, a more realistic shape for the wall. Except in a limited central portion, H_y and M_y are of identical signs; that is, the field pulls the vector $\vec{M}$ away from the easy direction over large distances on both sides of the x axis (Fig. 3-9). In that range of abscissae, the exchange torque, proportional to $d^2\theta/dy^2$, has a small, if not negligible, value in view of the slow θ variation. In these regions I and III, the actual field is

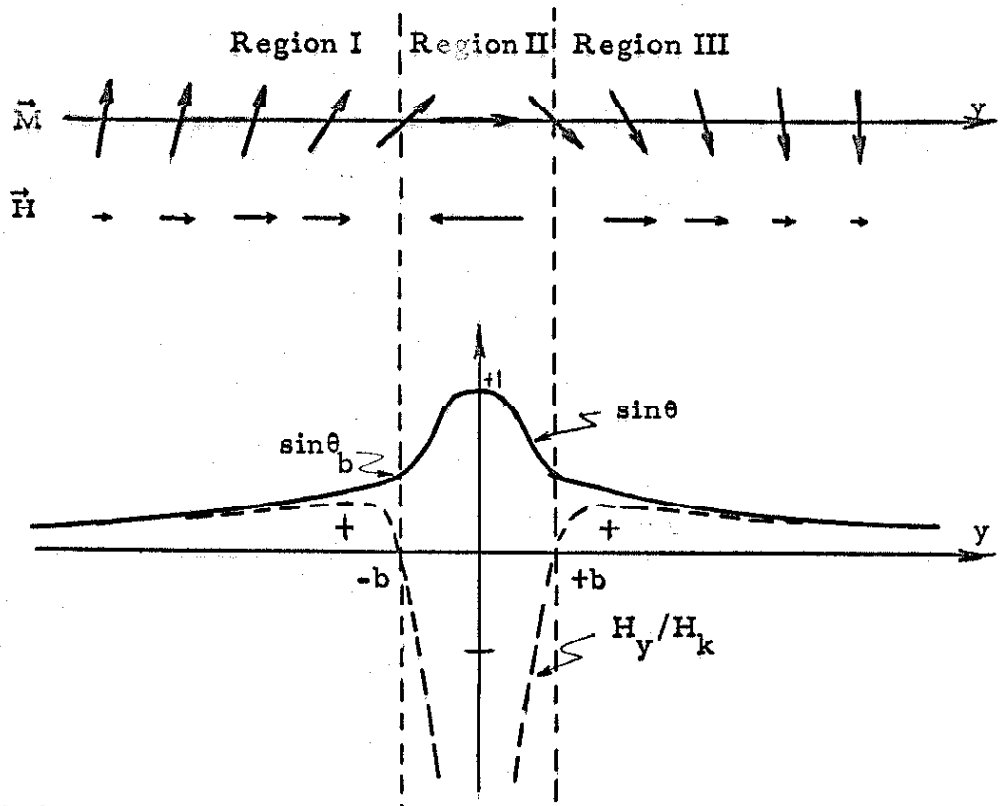

Fig. 3-9a

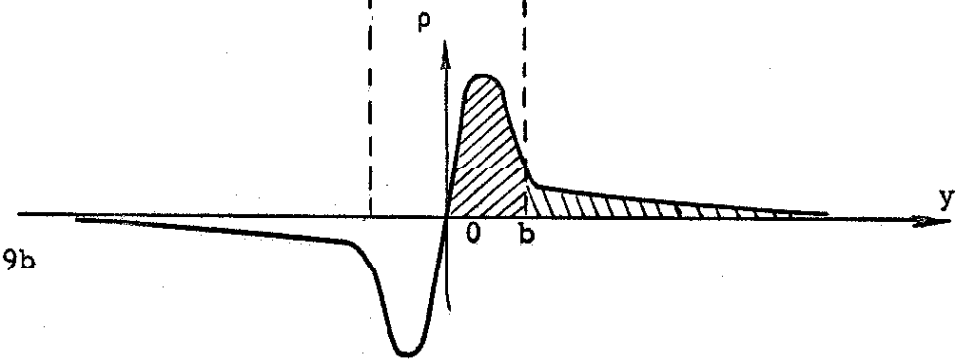

Fig. 3-9b

Actual variations of sin θ, H_y and ρ inside a Néel wall

almost equal to $H_k \sin\theta$ (from eq. 2.4-3), and consequently less than H_k at every point. Region II is characterized by a positive magnetostatic energy: H_y and M_y are of opposite signs and the rotation is fast in order to limit the volume with which this positive energy prevails.

If $\sin\theta_b$ is the sine value limiting regions II and III, the total amount of magnetic poles per unit length of wall between y=0 and y = b is $Mt(1 - \sin\theta_b)$ concentrated in the small interval 0 to b (Fig. 3-9b), whereas an amount equal to $Mt \sin\theta_b$ is spread out from b up to large distances, such as y = c, where $\theta \simeq 0$. This pole distribution produces a field which does not exceed $H_k \sin\theta$ at any point of region I or III, thus eliminating the inconsistently high values of H_y calculated from the Néel model where all poles are concentrated in the interval 0 to a (Fig. 3-8).

3.4 Remark on the Energy Content of the Wall

The total energy as computed by Néel does not include any magnetostatic term originating outside the limits y = ± a, and so might appear quite erroneous. However, in the new model of Figure 3-9, portions I and III of the curve do not contribute much energy. Indeed, the exchange energy density $A(d\theta/dy)^2$ (eq. 2.2-1), when integrated over the range b to c, gives, presuming a linear rotation:

$$E'_{ex} = A \int_{b}^{c} \left(\frac{d\theta}{dy}\right)^2 dy = A \int_{\theta_b}^{0} \frac{d\theta}{dy}\, d\theta = A \frac{\theta^2_b}{c}$$

This quantity tends to zero for large c. Most of the exchange energy, therefore, is contained in the interval -b to b, and is approximately equal to $2At \frac{(\pi/2-\theta_b)^2}{b}$. Similarly, although sin θ is different from zero for $|y| > b$, the sum of the anisotropy and magnetostatic energies is close to zero. The positive anisotropy term $K \sin^2\theta$ is balanced by the negative magnetostatic one $-\frac{\mu_o}{2} M_y H_y$ (from eq. 2.3-6). Neglecting the exchange torque as mentioned previously, the state of equilibrium between M and H is given by equation(2.4-3):

$$\sin\theta \simeq H_y/H_k$$

Thus, the sum of the two energy densities is:

$$\epsilon_a + \epsilon_m \simeq K \sin^2\theta - \frac{\mu_o}{2} MH_y \sin\theta$$

$$= K \sin\theta (\sin\theta - H_y/H_k) = 0$$

It is therefore to be expected that Néel's evaluation of the energy of the wall is somewhat too high, since, in fact, only the center part of the rotation contributes to the energy content.

3.5 Film of Thickness Tending Towards Zero

As a basis for the study of films of finite thickness, it is necessary to first treat the theoretical case t = 0. Furthermore, an approximate analytical determination of the internal field is

possible when t tends towards zero and the results are most useful in understanding the concept of regions I, II and III introduced in Section 3.3.

When t = 0, the internal field vanishes and only two terms have to be considered: the exchange and anisotropy torques. Their sum must be identical to zero everywhere. Thus, from equations (2.2-2) and (2.4-2),

$$2A \frac{d^2\theta}{dy^2} = K \sin 2\theta \qquad (3.5\text{-}1)$$

After multiplying both sides by $d\theta/dy$ and integrating between y and infinity ($\theta = d\theta/dy = 0$ at $y = \infty$), equation (3.5-1) becomes:

$$A \left(\frac{d\theta}{dy}\right)^2 = K \sin^2 \theta$$

or

$$dy = -\sqrt{\frac{A}{K}} \frac{d\theta}{\sin\theta} \qquad (3.5\text{-}2)$$

The exchange and anisotropy energies are equal at every point. The rotation of $\vec{M}$ is described by the following expression and is reproduced on Figure 3-10:

$$y = -\sqrt{\frac{A}{K}} \ln \left|\tan \frac{\theta}{2}\right| \qquad (3.5\text{-}3)$$

This function reduces to an exponential decay at large y. If the width 2a of the wall is defined as the distance separating the ordinates

$\theta = 5°$ and $\theta = 175°$, then $2a_o \sim 6.24\sqrt{A/K}$. If finite thicknesses are considered, magnetic poles will be present and a field will exist. However, if Δt is sufficiently small, in other words tending to zero, the magnetostatic energy will be negligible,

$$\frac{\mu_o}{2} \Delta H_y M_y << \epsilon_a = \epsilon_{ex} ,$$

and the field ΔH_y will not disturb the configuration of Figure 3-10a. Expression (2.3-1) will be used for the determination of ΔH_y. The volume density of poles (Fig. 3-10b) is easily deduced from equations (2.1-1) and (3.5-2):

$$\rho(y) = - M \frac{d \sin\theta}{dy} = - \frac{M}{2} \sqrt{K/A} \sin 2\theta ,$$

and, for a thickness Δt, the field is

$$\Delta H_y = \frac{\Delta t}{\pi} \int_o^\infty \frac{\rho(\eta)\eta \, d\eta}{y^2 - \eta^2}$$

Unless one uses numerical methods, there is no easy way to integrate the function $\rho\eta/(y^2 - \eta^2)$ unless $\rho(y)$ is reduced to a simpler form. The analysis needs be but qualitative, so $\rho(y)$ will be approximated as shown on Figure 3-10b (dashed line):

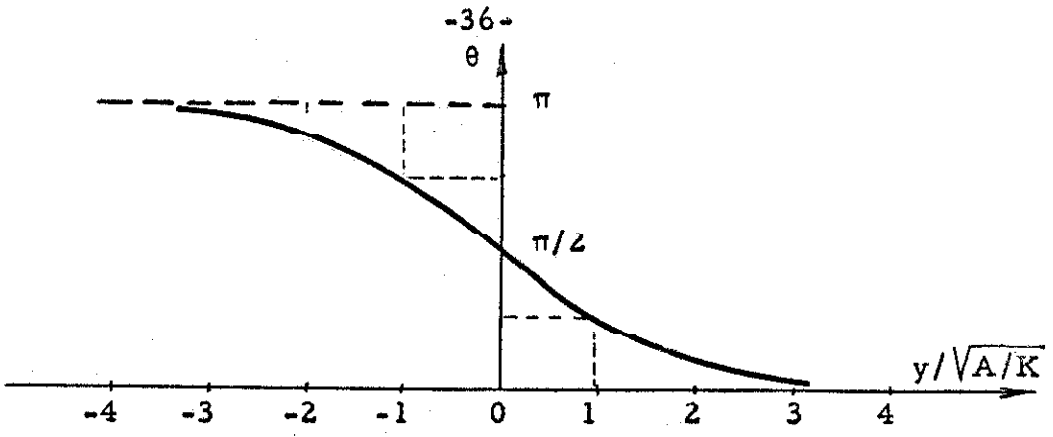

Fig. 3-10a

Rotation of magnetization in the case t = 0

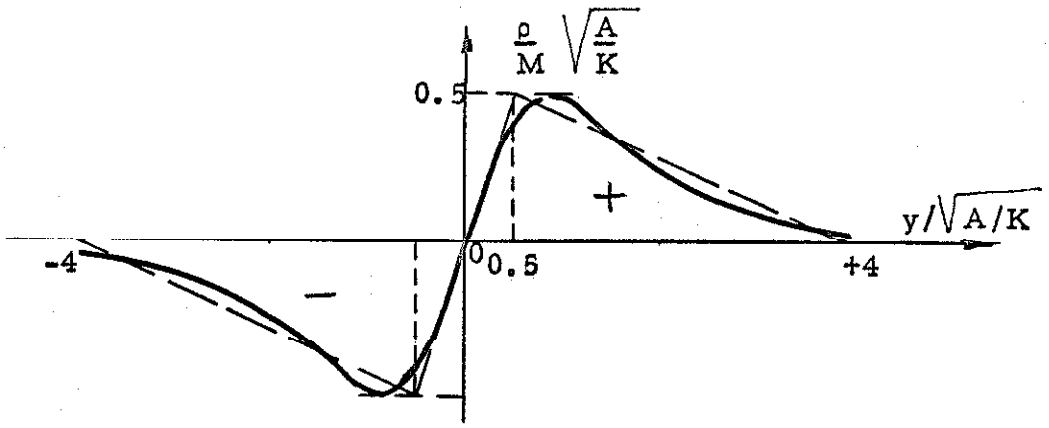

Fig. 3-10b

Volume density of poles

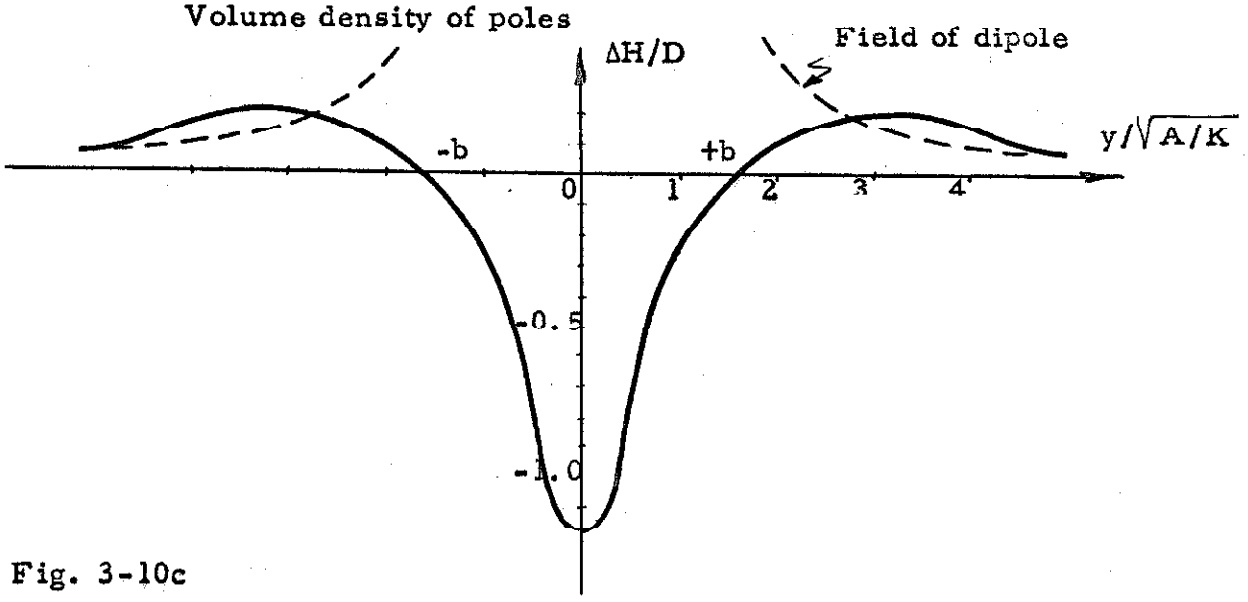

Fig. 3-10c

Field configuration when t ≃ 0

$$\rho = \frac{MK}{A}\, y \quad \text{for } 0 \le y \le 0.5B$$

$$\rho = \frac{MK}{A} \cdot \frac{4B-y}{7} \quad \text{for } 0.5B \le y \le 4B$$

$$\rho = 0 \quad \text{for } 4B < y$$

with $B = (A/K)^{\frac{1}{2}}$.

The condition $\int_o^\infty \rho\,(\eta)\, d\eta = M$ is still valid for this approximating function. A straightforward integration is now possible.

$$\Delta H_y = \frac{\Delta t}{\pi} \cdot \frac{MK}{A} \left[\int_o^{0.5B} \frac{\eta^2 d\eta}{y^2-\eta^2} + \frac{1}{7} \int_{0.5B}^{4B} \frac{(4B-\eta)\,\eta\, d\eta}{y^2-\eta^2} \right]$$

$$= D \left[\left(-\eta + \frac{y}{2} \ell n \left| \frac{y+\eta}{y-\eta} \right| \right)_o^{0.5B} - \frac{1}{7} \left(-\eta + \frac{y}{2} \ell n \left| \frac{y+\eta}{y-\eta} \right| \right)_{0.5B}^{4B} \right.$$

$$\left. - \tfrac{1}{2} \frac{4}{7} \ell n \left| y^2 - \eta^2 \right|_{0.5B}^{4B} \right]$$

$$= D \left[\frac{8}{14} (y + 0.5B) \ell n |y + 0.5B| - \frac{8}{14} (y - 0.5B) \ell n |y - 0.5B| \right.$$

$$\left. - \frac{1}{14} (y + 4B) \ell n |y + 4B| + \frac{1}{14} (y - 4B) \ell n |y - 4B| \right]$$

where $D = \frac{\Delta t}{\pi} \cdot \frac{MK}{A}$.

The field ΔH_y is drawn on Figure 3-10c. Far from the origin, it becomes equivalent to the field of an infinite line of dipoles, thus

decreasing with the square of the distance. Clearly, three regions can be distinguished: a central one "I" where ΔH_y and M_y are of opposite signs creating a positive magnetostatic energy and two adjacent regions "II" and "III" where field and magnetization form an angle less than $\pi/2$ with a negative energy associated with it. Energy-wise, it is advantageous to enlarge these portions of the wall I and III and to reduce region II. Indeed, when Δt increases, under the influence of $\Delta \vec{H}_y$, $\vec{M}$ will rotate at a faster rate from $y = 0$ to $y = b$, whereas for $y > b$, it will be pulled further away from the easy direction over large distances. In particular, the point $\theta = 5°$ will be reached at a larger abscissa and the wall width will increase accordingly. The preceding brief analysis supports the remarks of Section 3.3 concerning the actual behavior of the magnetization inside a Néel wall.

3.6 Magnetization Rotation in Films of Finite Thickness

When t is appreciably greater than zero, the magnetostatic energy is not negligible at all. On the one hand, a rigorous analytical treatment of the problem is not feasible and, on the other hand, the Ritz method, even using a more sophisticated model than Néel, is not reliable if conclusive results are to be obtained. Evidently, the only satisfactory solution is a numerical one based on the correct equations and performed on a computer.

Some assumptions must be made. As already indicated, only three types of energy are taken into account: exchange, anisotropy and magnetostatic. The functions expressing them are (2.2-1), (2.3-6) and (2.4-1). The wall is parallel to the easy direction (x axis) and is infinitely long, The magnetization rotates in the plane (x,y) through an angle of 180°. No external field is applied to the sample. Furthermore, variations of $\vec{M}$ and $\vec{H}_i$ (in particular $H_y(z)$ at a given y) along the z direction, perpendicular to the plane of the film, are neglected. Thus, the equations will be strictly unidimensional and independent of x and z.

The wall is represented in Figure 3-11 with the proper boundary conditions. At any point the volume energy density is equal to:

$$\varepsilon(y) = A(d\theta/dy)^2 + K \sin^2\theta - \frac{\mu_o}{2} M H_i \sin\theta \qquad (3.6\text{-}1)$$

The total energy per unit length of wall is obtained by integration

$$E = t \int_{-\infty}^{+\infty} \varepsilon(y)\, dy$$

The function $\theta(y)$ is unknown, but is such that E is a minimum. The condition $\delta E = 0$ for any $\delta\theta(y)$ determines $\theta(y)$. The calculus of variations applied to this case will lead to a differential equation, called the Euler equation, of the problem which, in fact, is the torque equation. The sum of the three torques is zero at every point, and this can be written down by inspection from equations (2.2-2), (2.3-7) and (2.4-2):

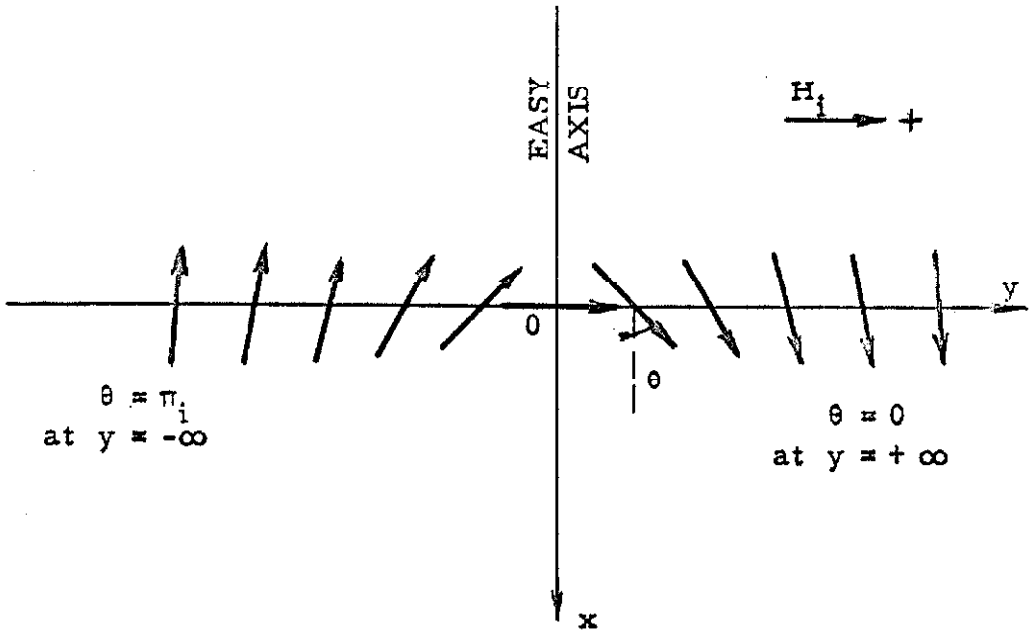

Fig. 3-11

Néel wall with boundary conditions as chosen in this work

$$2A(d^2\theta/dy^2) - K \sin 2\theta + \mu_o M H_i(y) \cos\theta = 0$$

or
$$\frac{A}{K} \cdot \frac{d^2\theta}{dy^2} = \cos\theta \left[\sin\theta - \frac{\mu_o M}{2K} H_i(y)\right] \qquad (3.6\text{-}2)$$

Recalling the definition of the anisotropy field $H_k = 2K/\mu_o M$, and introducing the dimensionless quantities:

$$h = H_i/H_k \quad \text{and} \quad y^* = y(K/A)^{\frac{1}{2}} \quad , \qquad (3.6\text{-}3)$$

equation (3.6-2) becomes:

$$d^2\theta/dy^{*2} = \cos\theta(\sin\theta - h[\theta(y^*)]) \qquad (3.6\text{-}4)$$

This second order, transcendental equation containing a functional $h[\theta(y^*)]$, with conditions $\theta = \pi/2$ at $y^* = 0$, and $\theta = 0$ at $y^* = -\infty$, will lead to a particularly complex two-point boundary problem.

The internal field is not known <u>a priori</u>, since it depends upon the configuration of the wall. For this reason, h cannot be expressed directly in terms of y^*, but rather will contain the function $\theta(y^*)$ itself. The determination of this functional is straightforward, however. The magnetization is presumed to remain in the plane (x,y) and not to vary with z; this assumption is valid because of the high demagnetizing factor associated with a component M_z (Sec. 2.4). The pole density is found by the usual formula:

$$\rho = -\text{div}\,\vec{M} = -M \frac{d(\sin\theta)}{dy}$$

At y, the field is obtained by integration of equation (2.3-2), that is:

$$H(y) = \frac{1}{\pi} \int_{-\infty}^{+\infty} \rho(\eta) \arctan \left(\frac{t}{2(y-\eta)} \right) d\eta$$

and, taking advantage of the antisymmetry of the ρ distribution with respect to the origin:

$$H(y) = \frac{M}{\pi} \int_{o}^{\infty} \frac{d(-\sin \theta)}{d\eta} \left[\tan^{-1} \left(\frac{t}{2(y-\eta)} \right) - \tan^{-1} \left(\frac{t}{2(y+\eta)} \right) \right] d\eta$$

or, introducing the reduced units:

$$h[\theta(y^*)] = C \int_{o}^{\infty} \frac{d(-\sin \theta)}{d\eta^*} \left[\tan^{-1} \left(\frac{t^*}{2(y^*-\eta^*)} \right) - \tan^{-1} \left(\frac{t^*}{2(y^* + \eta^*)} \right) \right] d\eta^* \qquad (3.6\text{-}5)$$

where $C = M/\pi H_k$ and $t^* = t/(A/K)^{\frac{1}{2}}$.

If $\mu_o M = 1$ Wb/m^2 and $H_k = 300$ At/m, $C = 845$.

The method used to solve the system of equations (3.6-4) and (3.6-5) on a 7090 IBM computer is now described. The solution $\theta_t(y^*)$ being known for thickness t^*, the solution $\theta_{t+\Delta t}(y^*)$, corresponding to a higher thickness $(t^* + \Delta t^*)$ is sought. The increment Δt^* being small, θ_t may be chosen as a first approximation to $\theta_{t+\Delta t}$. Indeed, the integrodifferential equation obtained by replacing $h[\theta(y^*)]$ by its value (3.6-5) in equation (3.6-4) is impossible to solve as such. The functional $h[\theta(y^*)]$ must be treated as a function of y^* simply, which is then introduced in equation (3.6-4), thus enabling it to be

solved as a usual two-point boundary problem. A first approximation $h_o(y^*)$ is obtained by using $\theta_o = \theta_t(y^*)$ for the computation of the field at thickness $(t^* + \Delta t^*)$. A second approximation $\theta_1(y^*)$ is determined by solving equation (3.6-4) where $h = h_o$, which in turn generates a new field $h_1(y^*)$. Successive cycles of this type should finally lead to practically identical solutions θ_N and θ_{N+1} if the process converges at all. This scheme is summarized as follows:

$$\left.\begin{aligned} & h_n(y^*) = h\,[\theta_n(y^*),\ (t^* + \Delta t^*)] \\ & \frac{d^2\theta_{n+1}}{dy^{*2}} = \cos\theta_{n+1}\,(\sin\theta_{n+1} - h_n(y^*)) \end{aligned}\right\} \qquad (3.6\text{-}6)$$

with $\theta_o(y^*) = \theta_t(y^*)$

and finally $\theta_N(y^*) = \theta_{t+\Delta t}(y^*)$

The starting thickness is obviously $t^* = 0$, since a rigorous analytical solution is available for that case. Equation (3.5-3) can be rewritten:

$$\theta(y^*) = 2 \arctan\,(e^{-y^*}) \quad \text{for} \quad t^* = 0$$

From this point on, higher and higher thicknesses are considered.

Several very delicate problems arise in this step by step operation, such as a proper selection of boundary conditions, convergence or stability of successive iterations, choice of suitable division of the abscissa axis in discrete intervals at which θ and h are to be calculated. These questions are discussed in detail hereafter in order to clarify several peculiarities of the computer

program in Appendix B, which would otherwise be incomprehensible.

3.6.1 Abscissa Axis

The range of abscissae is limited between $y^* = 0$ and $y^* = Y_\infty$, at which point θ should be sufficiently small as to be almost equal to h. It has been shown in Section 3.3 that the rotation is extremely slow at large y^* and that $\sin\theta$ is just slightly larger than $h(y^*)$ in that region. Hence, the semi-infinite axis is replaced by a finite section 0 to Y_∞. In order to limit the use of the computer to a practical length of time, it is imperative to maintain the number of divisions of the y axis under a certain value. On the other hand, the functions $\sin\theta(y^*)$ and $h(y^*)$ must be satisfactorily described up to Y_∞. Since the variation of $\sin\theta$ with y^* is rapid in the positive magnetostatic energy region (negative h) and slower thereafter, a double mesh has been chosen which satisfies the above requirements: one hundred intervals are provided between 0 and Y_1, and another hundred between Y_1 and Y_∞, with $Y_1 << Y_\infty$, as indicated in Figure 3-12. The intervals (Δy_1^*) are small where $\sin\theta$ varies rapidly, and larger (Δy_2^*) for the remainder of the range. Thus, the functions θ, $\sin\theta$, h, etc., appear as tables of 201 values.

3.6.2 Boundary Conditions

At $y^* = 0$, $\sin\theta$ equals one and then decreases towards zero, with $h(y^*)$, when y^* tends to infinity. However, having substituted

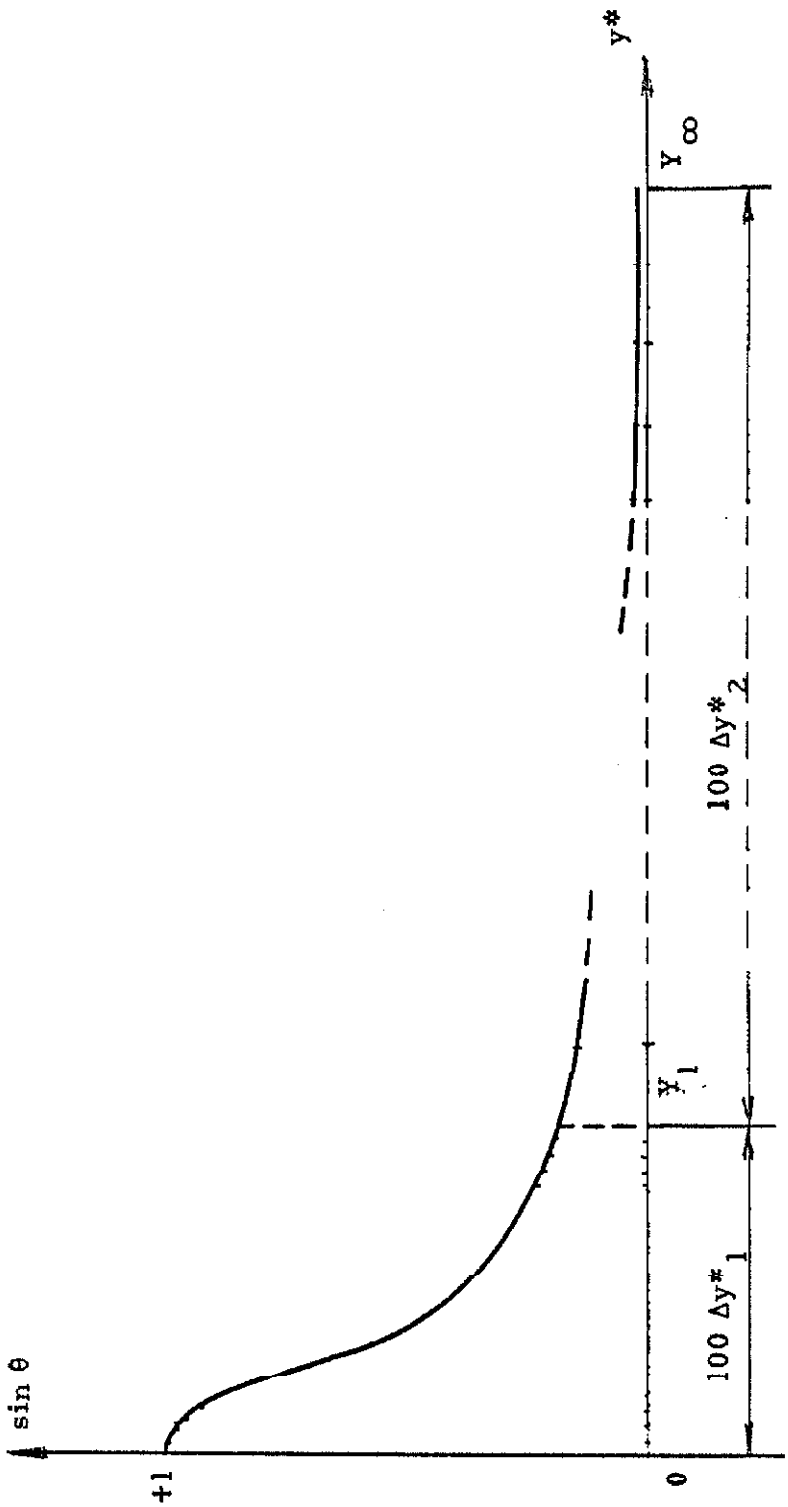

Fig. 3-12

Division of the abscissa axis

Y_∞ in place of infinity, the requirement $\sin\theta = 0$ is no longer correct at that limit. Instead, the condition

$$\sin^{-1}[h(Y_\infty)] \leq \theta(Y_\infty) \leq 1.005 \cdot \sin^{-1}[h(Y_\infty)] \qquad (3.6\text{-}7)$$

will be imposed. This boundary condition is not rigorously exact since, in fact, $\sin\theta$ is somewhat larger than h everywhere, but this does not affect the accuracy of the function $\sin\theta(y^*)$ at lower abscissae because, as numerical calculations show, an error of even 10 % at $y^* = Y_\infty$ would reflect an error of a fraction of a per cent only at $y^* = Y_\infty/2$, for instance. The very tail of the wall where θ is of the order of 5° is of no practical interest anyhow, due to variations of the easy direction at a microscope scale, as observed by Fuller and Hale (22), who first detected the so-called "ripple" of magnetization.

The function $h_n(y^*)$ being known, a solution of the differential equation (3.6-4) exists for every slope $\dot{\theta}(o) = d\theta/dy^*\big|_o$ chosen at the origin. The correct value of $\dot{\theta}(o)$ will be determined by trial and error in order to satisfy the condition (3.6-7). Figure 3-13 illustrates three cases where the slope at $y^* = 0$ is larger, equal to and smaller than the correct value. For too small a negative slope, the function oscillates around the ordinate $\theta = \pi/2$, and never crosses the curve $h(y^*)$ (curve "1"), whereas for too high a positive slope, $\theta(y^*)$ tends towards minus infinity after its intersection with $h(y^*)$

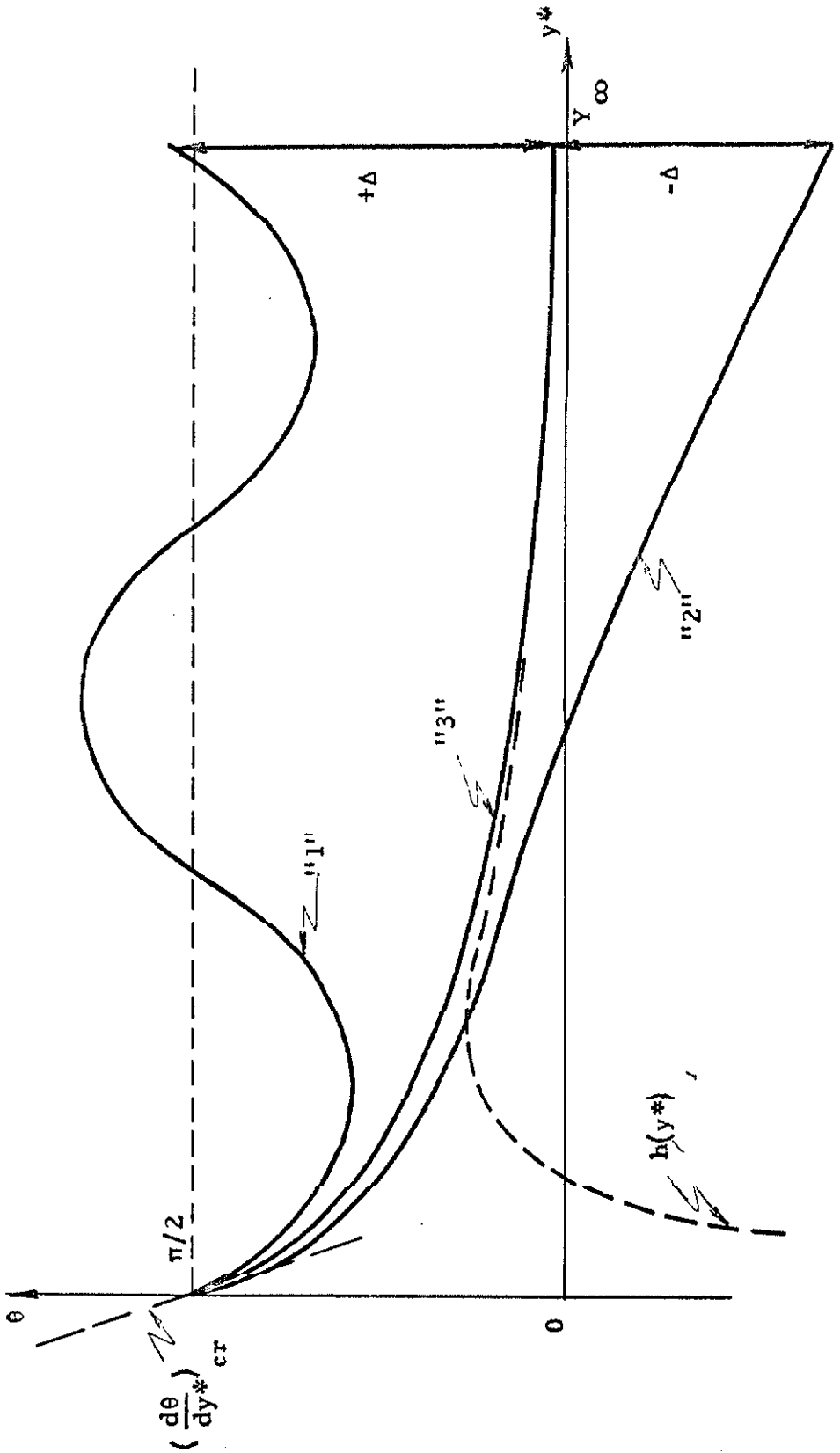

Fig. 3-12 Effect of the initial slope $\left(\frac{d\theta}{dy^*}\right|_o$

(curve "2"). Curve "3," which is the only acceptable solution having any physical meaning, corresponds to the critical slope $\dot{\theta}(o)_{cr}$.

In the first case, the error $\Delta = \theta - \sin^{-1} h$ at Y_∞ will always be positive; in the second case, it will always be negative. Because of the oscillatory nature of curve "1," a smaller Δ does not necessarily indicate a better choice of $\dot{\theta}(o)$. For this reason, a proportional interpolation formula cannot be used for the determination of better and better approximations of $\dot{\theta}(o)_{cr}$. Instead, the following rule shall be used: "If $|\dot{\theta}(o)|_{max}$ is the maximum absolute value of the slope still leading to a positive error Δ at Y_∞ and $|\dot{\theta}(o)|_{min}$, the minimum value still leading to a negative Δ, then the next trial will be:

$$\frac{|\dot{\theta}(o)|_{max} + |\dot{\theta}(o)|_{min}}{2} \quad " \tag{3.6-8}$$

This process will always work if two initial trials are performed, the first one with too small a slope and the second with too high a slope.

The value Y_∞ being too large, the number of significant figures (eight) available on the computer for the choice of $\dot{\theta}(o)$ will not suffice to satisfy condition (3.6-7). Even the double precision method will not be adequate. But, as found numerically and shown on Figure 3-14, the curve obtained by determining $\dot{\theta}(o)_{cr}$ correctly up to the

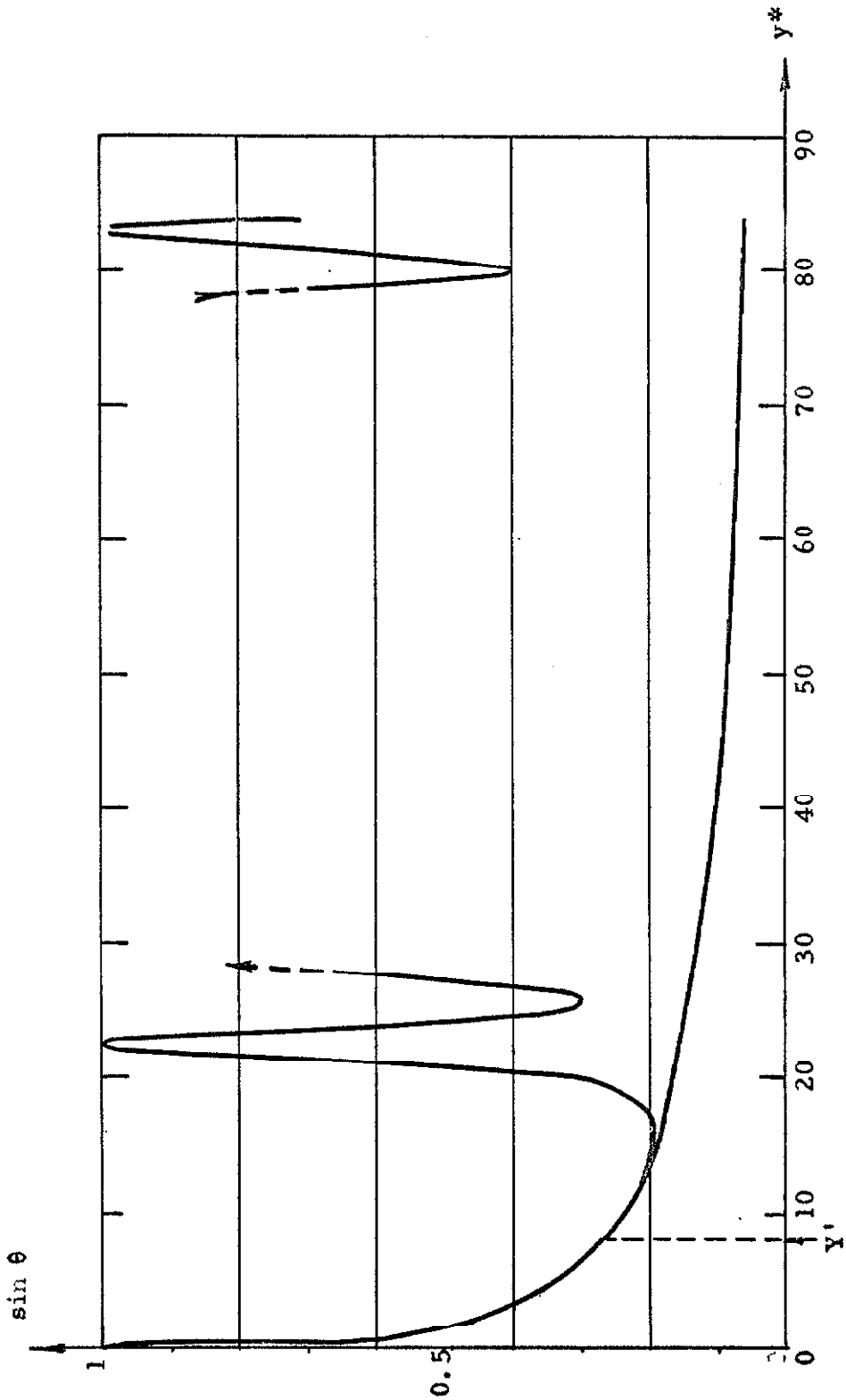

Fig. 3-14 Effect of the limited number of significant figures to express the initial slope $d\theta/dy^*|_o$

last decimal available, according to rule (3.6-8), on the one hand, and the exact solution, on the other hand, do not differ appreciably along a sizable section of the abscissa axis 0 to Y'. The value of Y' depends evidently upon the discrepancy tolerated at that point (0.01 per cent in this work). At Y', the slope $\dot{\theta}(Y')_{cr}$ is now correct up to a few decimals only. The method used to determine $\dot{\theta}(o)$ and the function $\theta(y^*)$ with accuracy from 0 to Y' will be repeated between Y' and Y'', then Y'' and Y''', etc., up to Y_∞. Thus, the differential equation will be solved again starting this time at Y' with $\theta(Y')$ known and two trial values for the slope:

$$\dot{\theta}(Y') = \dot{\theta}(Y')_{cr} \pm 10\%$$

3.6.3 Convergence of Successive Approximations $\theta_n(y^*)$

It is assumed that $\theta_t(y^*)$ has been found for thickness t*. Starting with this function, the solution $\theta_{t+\Delta t}(y^*)$ should be reached by successive steps, as indicated in the system of equations (3.6.6). Although a physical solution exists, it is not certain that this process will be a convergent one, even if Δt^* is taken small. A detailed study of stability in such a complex problem is not feasible a priori. An actual trial is faster and conclusive. It was found that, above a certain thickness $t^* \simeq 0.002$, the successive approximations diverge. In other words, if the exact functions $\theta(y^*)$ and $h(y^*)$ were known, and a perturbation $\delta\theta$ were introduced at a certain point intentionally,

the new perturbed function $\theta' = \theta + \delta\theta_1$ would lead to a perturbed field $h' = h + \delta h$, which itself, being introduced in equation (3.6-4), would produce a new curve $\theta'' = \theta + \delta\theta_2$ with $|\delta\theta_2| > |\delta\theta_1|$.

Some portions of the curve are more unstable than others, notably regions I and III, where sin θ and h are nearly equal.

The following analysis, although schematic, explains this observed unstable behavior and suggests a remedy for it. The correct sin θ function is represented in Figure 3-15a, together with the correct field $h(y^*)$. The corresponding distribution of magnetic poles $\rho(y^*)$ appears in Figure 3-15b. The perturbation introduced at c^* is indicated on Figure 3-15b, and for the sake of the calculation has been given a simple form:

$$\delta\rho = M\sqrt{K/A}\ \epsilon_1^*(y^* - c^*)$$

between c^*-d^* and c^*+d^*.

The function sin θ itself is barely affected by this change in its first derivative. The additional field δh due to $d\rho$ is evaluated using equation (2.3-1):

$$\delta h = \frac{1}{H_k}\ \frac{Mt^*}{2\pi}\ \int_{c^*-d^*}^{c^*+d^*}\ \frac{\epsilon_1^*(\eta^*-c^*)}{y^*-\eta^*}\ d\eta^*$$

or, at $y^* = c^*$:

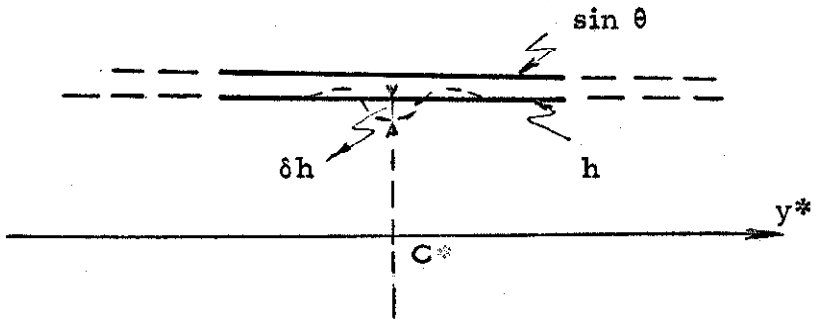

Fig. 3-15a

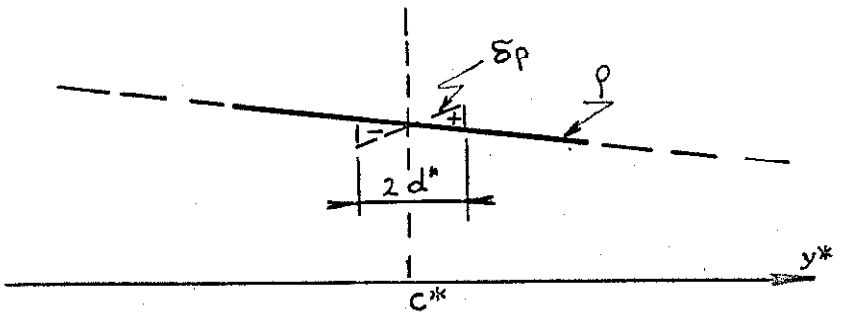

Fig. 3-15b

Perturbation δρ introduced in the pole distribution and resulting variation δh of the field

$$\delta h_c = - C\ t^*\ \epsilon_1^*\ d^*$$

with $C = M/\pi\ H_k$

In this example, the point c* has been chosen in region III where the following approximations are permissible:

$$\cos\theta \simeq 1,\ \sin\theta = \theta,\ \rho = - M\sqrt{K/A}\ \frac{d\theta}{dy^*}\ ,\ \epsilon^* = - \frac{d^2(\delta\theta)}{dy^{*2}}$$

and

$$d^2\theta/dy^{*2} \simeq \sin\theta - h$$

Therefore, assuming that $\sin\theta$ has not changed at c*, the next iteration will give:

$$\epsilon_2^* = - \frac{d^2(\delta\theta_2)}{dy^{*2}} \Bigg|_{c^*} = \delta h_c$$

and finally: $\epsilon_2^* = - C\ t^*\ d^*\ \epsilon_1^*$ (3.6-9)

Thus, the initial perturbation ϵ_1^* of the second derivative $d^2\theta/dy^{*2}$ results in a perturbation ϵ_2^* and the successive approximations will be divergent if $C\ t^*\ d^* > 1$. This analysis, although qualitative, shows clearly that, as such, the iteration scheme (3.6-6) fails above a certain thickness. Since in this study $C = 845$ and $d^*_{min} = \Delta y^*_2 = 0.4$, this critical thickness should be of the order of 0,003. In fact, instability was observed around $t^* = 0.002$.

Because of this instability, the proposed method must be modified. The modification to be introduced is simple and was found to eliminate all instability. Its disadvantage is a slow convergence in certain portions of the y-axis, which makes it necessary to go through quite a number of approximation cycles. Nevertheless, the process can be accelerated as explained below. The important fact is to note that ε^*_2 and ε^*_1 are of opposite signs. Therefore, starting with the erroneous function θ_n and obtaining the function θ_{n+1}, as in equation (3.6-6), the next approximation, rather than θ_{n+1} itself, will now be a combination of both θ_n and θ_{n+1}:

$$(1 - m) \sin \theta_{n+1} + m \sin \theta_n \qquad (3.6\text{-}10)$$

The errors ε^*_2 and ε^*_1 will tend to compensate each other. Indeed, if $\varepsilon^*_2 = - k \varepsilon^*_1$, the convergence will be insured if:

$$| (1 - m) \varepsilon^*_2 + m \varepsilon^*_1 | < | \varepsilon^*_1 |$$

or, $$| - k + m (1 + k) | < | 1 | ;$$

that is:

$$\frac{k - 1}{k + 1} < m < 1 \qquad (3.6\text{-}11)$$

For a given k, the convergence will be fastest when:

$$(1 - m) \varepsilon^*_2 + m \varepsilon^*_1 = 0$$

or $$m = \frac{k}{k + 1} \qquad (3.6\text{-}12)$$

As t* increases, so does k , and it will be necessary to increase m correspondingly.

This study of the stability of the curve in regions I and III is not valid in the central portion II. There, actual calculations show a greater stability. Furthermore, the value of m (3.6-12), selected in order to optimize the convergence of the tail of the sin θ function, is found to cause the central part to converge comparatively slowly. In order to limit the total number of cycles and still reach the proper function sin θ for small abscissae, after every few iterations a lower value of m will be used which will accelerate the stabilization of region II.

In Appendix A, a possible alternate method is proposed for the solution of the system of equation (3.6-6). It has, however, not been tested for convergence.

3.6.4 Example of the Determination of θ(y*) for a Given Thickness

The computer program is reprinted and explained in Appendix B. In the present section, the transition from thickness t* = 0.04 to t* + Δt* = 0.05 is reproduced in detail.

The y* axis extends from 0 to $Y_\infty = 84$. The change of mesh occurs at $Y_1 = 4$, so that $\Delta y^*_1 = 0.04$ and $\Delta y^*_2 = 0.8$. In the case t* = 0.04, at y* = 4, sin θ equals 0.35 and thereafter, together with h(y*), decreases slowly to 0.045 at y* = 84; one hundred intervals

are adequate to describe these functions between 4 and 84. As indicated in Section 3.6.2, the axis is divided into several intervals, according to the tolerance criterion established in that section: 0 to Y', Y' to Y'', etc., with Y' = 8, Y'' = Y' + 12 = 20, Y''' = Y'' + 12 = 32, etc. Figure 3-16a represents the correct solution $\sin \theta_t$ and the corresponding internal field for thickness t* = 0.04. The field $h_o(y^*)$ obtained from the function $\sin \theta_o = \sin \theta_t$, used as the first approximation for thickness 0.05, is reproduced on Figure 3-16b (dashed curve). The fields h_o and h_t are approximately proportional; strict proportionality is not to be expected because of the arctan functions in equation (3.6-5).

The next step is to determine the solution $(\sin \theta_1)'$ of the differential equation with $h = h_o(y^*)$. The initial slopes $\dot{\theta}(o)$, necessary to start the process expressed in the rule (3.6-8), are -12 and -4, respectively, below and above the critical value $\dot{\theta}(o)_{cr}$ still unknown. Twenty-nine trials are needed before exhausting all decimals, the result being

$$\dot{\theta}(o)_{cr} = -7.80204E \quad (*)$$

For this value of the slope, the discrepancy between θ and $\sin^{-1} h$ at Y_∞ is still $\Delta = 2.54$, and the boundary condition (3.6-7) is far

---

(*) The symbol E stands for existing but unprinted decimals.

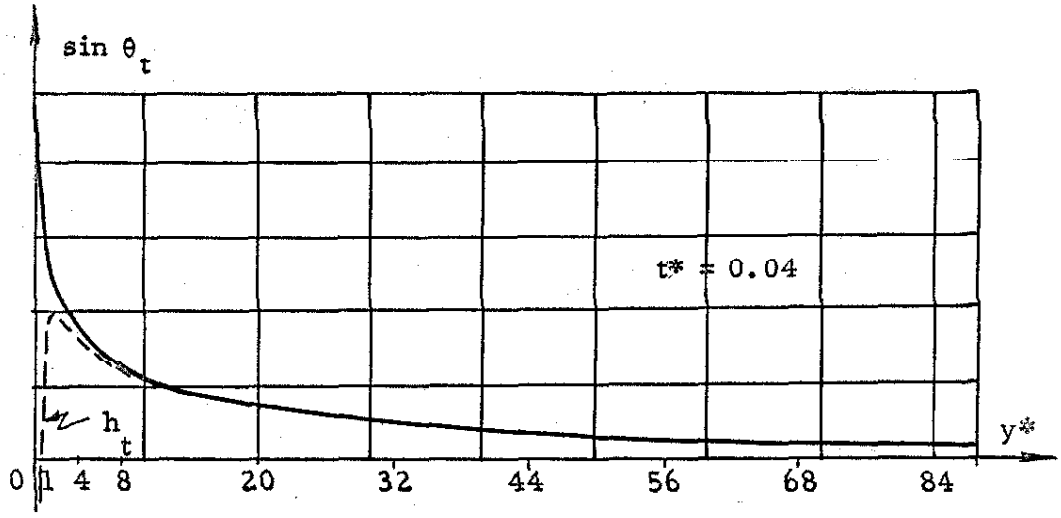

Fig. 3-16a

Sin θ_t and h_t for t* = 0.04

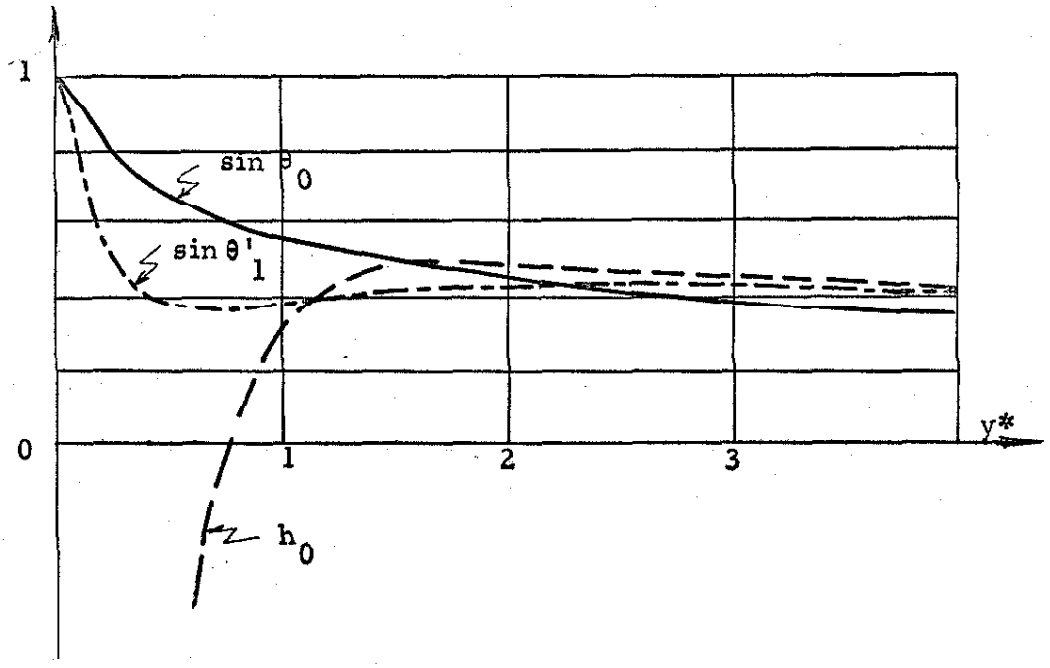

Fig. 3-16b

Starting cycle of the thickness transitions
t* = 0.04 to t* + Δt* = 0.05

from being satisfied. The curve is correct only in the lower range of the y* axis; this first section is limited to Y' = 8. At that point, two new initial slopes are chosen:

$$\dot{\theta}(8) = \dot{\theta}(8)_{cr} \pm 10\%$$

and the same process occurs. This time, after 27 trials, all the decimals of $\dot{\theta}(8)_{cr}$ are known, but the error at y* = 84 is 2.51. A new section of the curve, however, between Y' = 8 and Y'' = 20, has been determined. The function $(\sin \theta_1)'$ has actually been computed in seven steps: 0 to 8, 8 to 20, 20 to 32, 32 to 44, 44 to 56, 56 to 68, and 68 to 84; it is reproduced on Figure 3-16b also, and it shows a large oscillation around y* = 1.

This series of computations represents but the first cycle of scheme (3.6-6). The second approximation will then be (from 3.6-10):

$\sin \theta_1 = 0.05 \cdot (\sin \theta_1)' + 0.95 \cdot \sin \theta_o$. The coefficient m has been given the value 0.95, which insures the stability of the calculations in region III. In this instance, from equation(3.6-9), where $d^* \simeq \Delta y^*_2 = 0.8$,

$$k = C\ t^*\ d^* = 845 \cdot 0.05 \cdot 0.8 = 34 .$$

The convergence inequality (3.6-11) gives:

$$0.94 < m < 1 ,$$

and, according to equation (3.6-12), the optimum value of m is:

$$m = 34/35 = 0.97 .$$

The new function $\sin \theta_1$ can then be used to compute another approximation of the field $h_1(y^*)$, which is in turn introduced in the differential equation to obtain $(\sin \theta_2)'$. The successive approximations will be given by formula (3.6-10):

$$\sin \theta_{n+1} = (1 - m) (\sin \theta_{n+1})' + m \sin \theta_n .$$

The number of such cycles in this example is 24. The value of m is 0.95, except for n = 10 and n = 19, where it is 0.5, this last value in order to accelerate the convergence in region II, as explained in Section 3.6.3. Table 3-I, as well as Figures 3-17 and 3-18, represent the values of $h_n(0)$, $h_n(84)$, $\sin \theta_n(4)$ and $\sin \theta'_{n+1}(4)$ for the successive cycles of approximation, n varying from 0 to 24. The abscissa $y^* = 4$, at which $h(y^*)$ and $\sin \theta(y^*)$ start converging towards each other (Fig. 3-16a), has been chosen to characterize $\sin \theta$ at an intermediate point. The quantity $h(84) \simeq \sin \theta\ (84)$ converges rapidly, as can be seen on the preceding table (h(84) is practically stabilized at n = 9). The field h(0) tends much slower towards its final value: -132.4. Figure 3-18 shows how a reduction of m somewhat accelerates the process. The first change in the m value could have been introduced earlier, such as at n = 5, for instance, where it would have been more efficient. At $y^* = 4$, $\sin \theta$

Table 3-I

Successive Cycles Represented by the System of Equations (3.6-6)

n	m	$\sin \theta_n(4)$	$\sin \theta'_{n+1}(4)$	$h_n(0)$	$h_n(84)$
0	0.95	0.3493	0.4197	-119.99	0.0591
1	0.95	0.3528	0.3259	-127.02	0.0599
2	0.95	0.3515	0.3815	-127.90	0.0604
3	0.95	0.3530	0.3587	-128.99	0.0607
4	0.95	0.3532	0.3695	-129.58	0.0609
5	0.95	0.3541	0.3639	-130.10	0.0611
6	0.95	0.3546	0.3660	-130.47	0.0615
7	0.95	0.3551	0.3645	-130.78	0.0617
8	0.95	0.3556	0.3648	-131.03	0.0619
9	0.95	0.3561	0.3643	-131.24	0.0620
10	0.50	0.3602	0.3634	-133.00	0.0620
11	0.95	0.3603	0.3617	-132.92	0.0621
12	0.95	0.3604	0.3628	-132.85	0.0621
13	0.95	0.3605	0.3624	-132.79	0.0622
14	0.95	0.3606	0.3628	-132.74	0.0622
15	0.95	0.3607	0.3627	-132.70	0.0621
16	0.95	0.3608	0.3628	-132.67	0.0620
17	0.95	0.3609	0.3628	-132.64	0.0620
18	0.95	0.3610	0.3629	-132.61	0.0620
19	0.50	0.3619	0.3631	-132.39	0.0616
20	0.95	0.3620	0.3631	-132.39	0.0617
21	0.95	0.3621	0.3631	-132.39	0.0618
22	0.95	0.3621	0.3631	-132.38	0.0617
23	0.95	0.3622	0.3631	-132.38	0.0617
24	0.95	0.3622	---	-132.38	0.0617

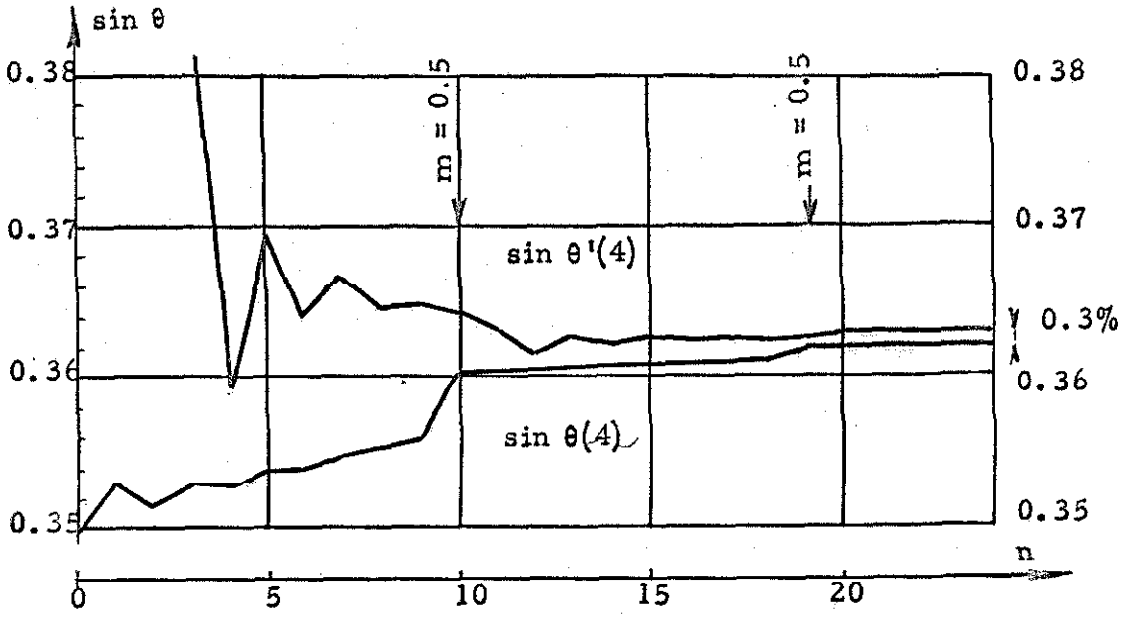

Fig. 3-17

Convergence of sin θ'(4) and sin θ(4) (t* = 0.05)

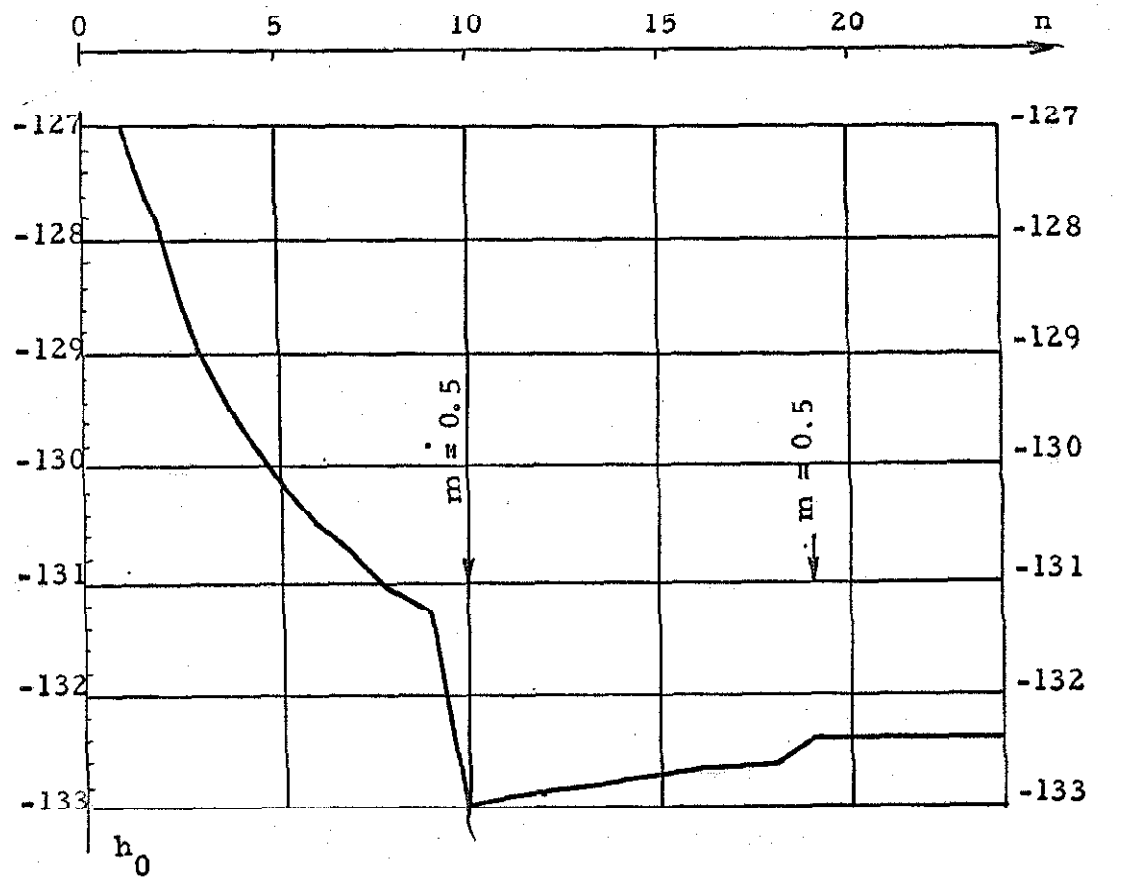

Fig. 3-18

Convergence of $h_{(0)}$ (t* = 0.05)

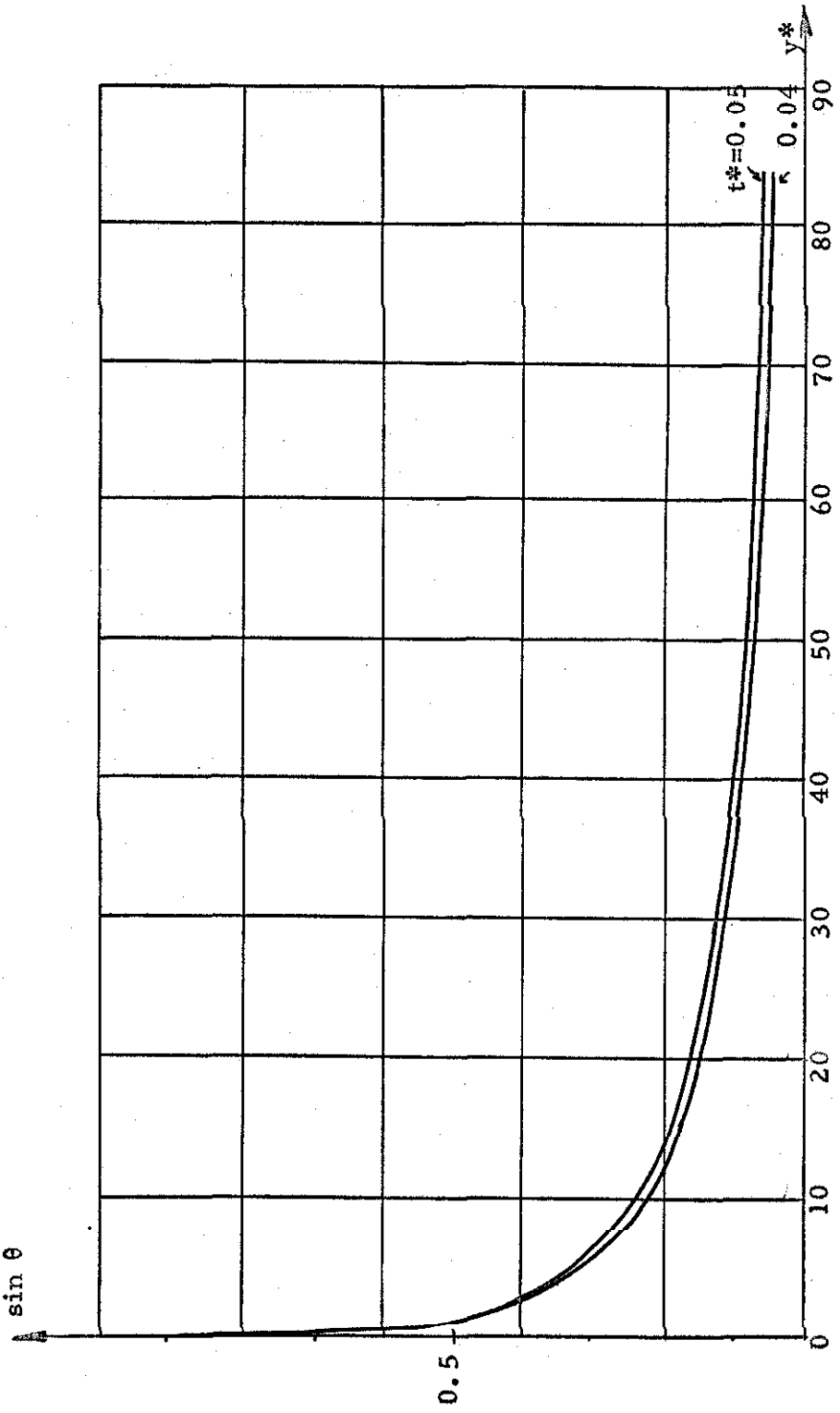

Fig. 3-19a

Shape of the wall for $t^* = 0.04$ and $t^* = 0.05$

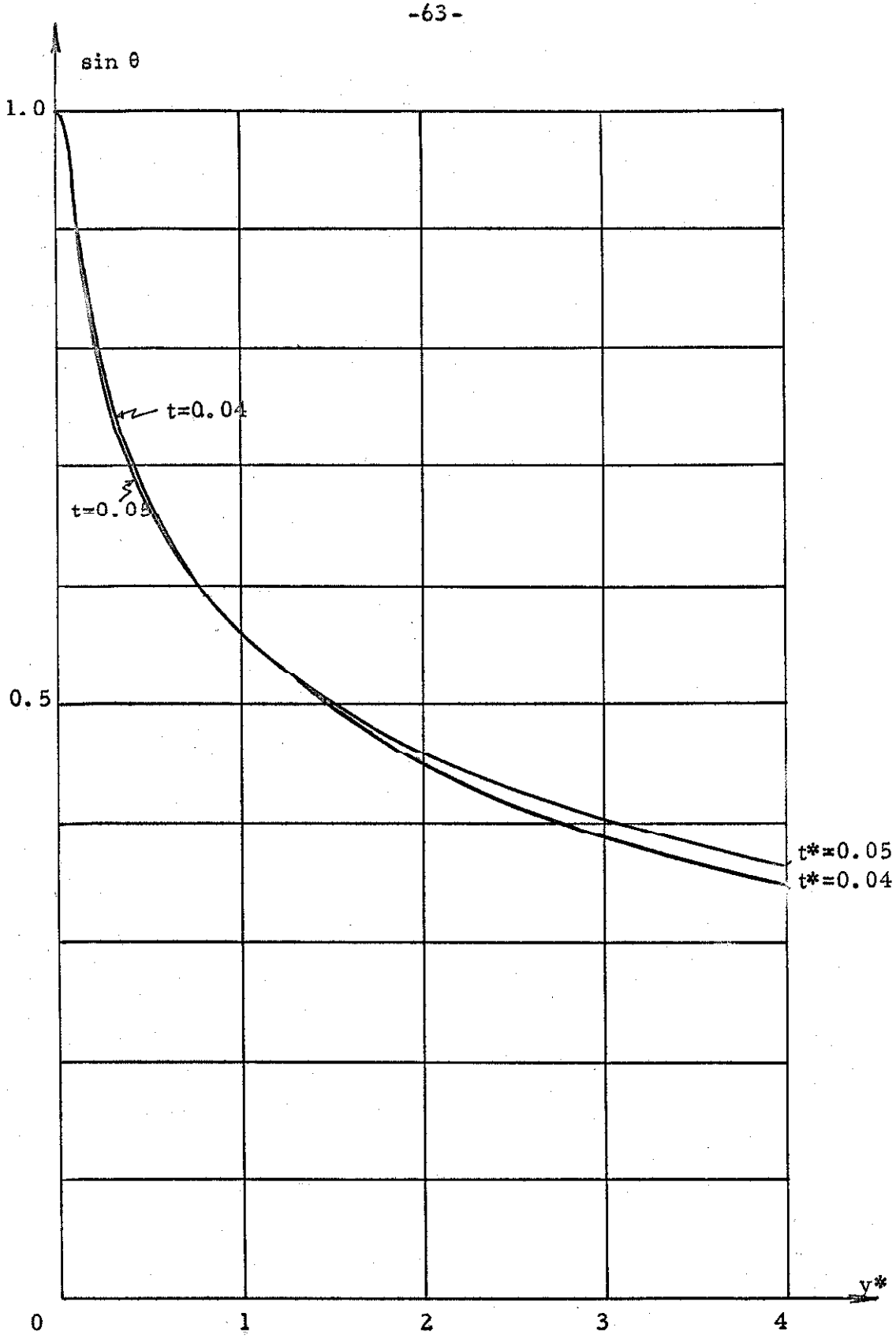

Fig. 3-19b

Shape of the wall for t* = 0.04 and t* = 0.05 (enlarged)

clearly tends towards $\sin \theta'$ (4), but it is not necessary to achieve $\sin \theta = \sin \theta'$. Indeed, the function $\sin \theta'_{24}$, rather than $\sin \theta_{24}$, will be taken as the final solution for thickness 0.05. Figures 3-19a and b show the shape of the wall for $t^* + \Delta t^* = 0.05$, compared to the shape at $t^* = 0.04$. In the lower range of abscissae, the curves are very similar. At $y^* = 84$, the ratio $\sin \theta_{t+\Delta t} / \sin \theta_t = 0.0619 / 0.0479 = 1.295$ is close to $0.05/0.04 = 1.25$.

3.6.5 Results for the Range of Reduced Thicknesses 0 to 0.08

Recalling the factor $C = M/\pi H_k$ used in the numerical computations (eq. 3.6-5), it is clear that the ratio M^2/K is predetermined. The quantity $(A/K)^{1/2}$, however, can be chosen freely. Typical constants for 80 Permalloy films are $\mu_o M = 1$ Wb/m^2 or $M = 8 \cdot 10^5$ At/m, $K = 150$ J/m^3 or $H_k = 300$ At/m, and $A = 10^{-11}$ J/m. The factor $(A/K)^{\frac{1}{2}}$ is then equal to $0.258 \cdot 10^{-6}$ m = 2580 Å, and the reduced units $t^* = t/(A/K)^{\frac{1}{2}}$, $y^* = y/(A/K)^{\frac{1}{2}}$ can be expressed in terms of Angstrŏms. Thickness $t^* = 0.08$ would in this case be approximately equal to 200 Å, which is close to the observed transition thickness t_{cl} between Néel walls and cross-tie walls in films of such composition (20).

The passage from $t^* = 0$ to 0.08 has been accomplished in steps of about 25%, except for the first few values. Time and cost of computation, as well as the appearance of cross-ties above 200 Å,

were the reasons to limit the range to this value.

Figures 3-20a and b represent the rotation of $\vec{M}$ in a Néel wall for the case t* = 0, 0.0084 (21 Å), 0.02 (50 Å), 0.04 (100 Å), 0.06 (150 Å), and 0.08 (200 Å). The corresponding pole densities $\rho(y^*)$ appear in Figure 3-21 for t* = 0.02, 0.04 and 0.08. Finally, the internal fields h(y*) are reproduced in Figure 3-22, where a reduced field of one is equal to H_k. It is seen how region II (positive magnetostatic energy) diminishes in length and h(0) reaches large negative values when t* increases (Fig. 3-23). The maximum positive field h^+_{max} varies little, since it is subject to the condition $h(y^*) < \sin\theta(y^*)$, but region III spreads farther and farther to the right.

In Figure 3-20a, the fast and slow rotation portions of the curves are clearly distinguishable, and it is interesting to notice that for all thicknesses considered, the angle θ goes through 30° at an abscissa varying very little around 1.35. The width of the wall, if it is determined by the limits θ = 5° and 175°, increases considerably with t* (Fig. 3-24). It was mentioned previously that an angle of 5° was of the order of the random variations in the direction of the local easy axis. Therefore, a width 2a, corresponding to a total variation of 170°, has little physical meaning, but may nevertheless serve for a comparison with Néel's results. Figure 3-25 shows, as a function of thickness, the distance y between the center

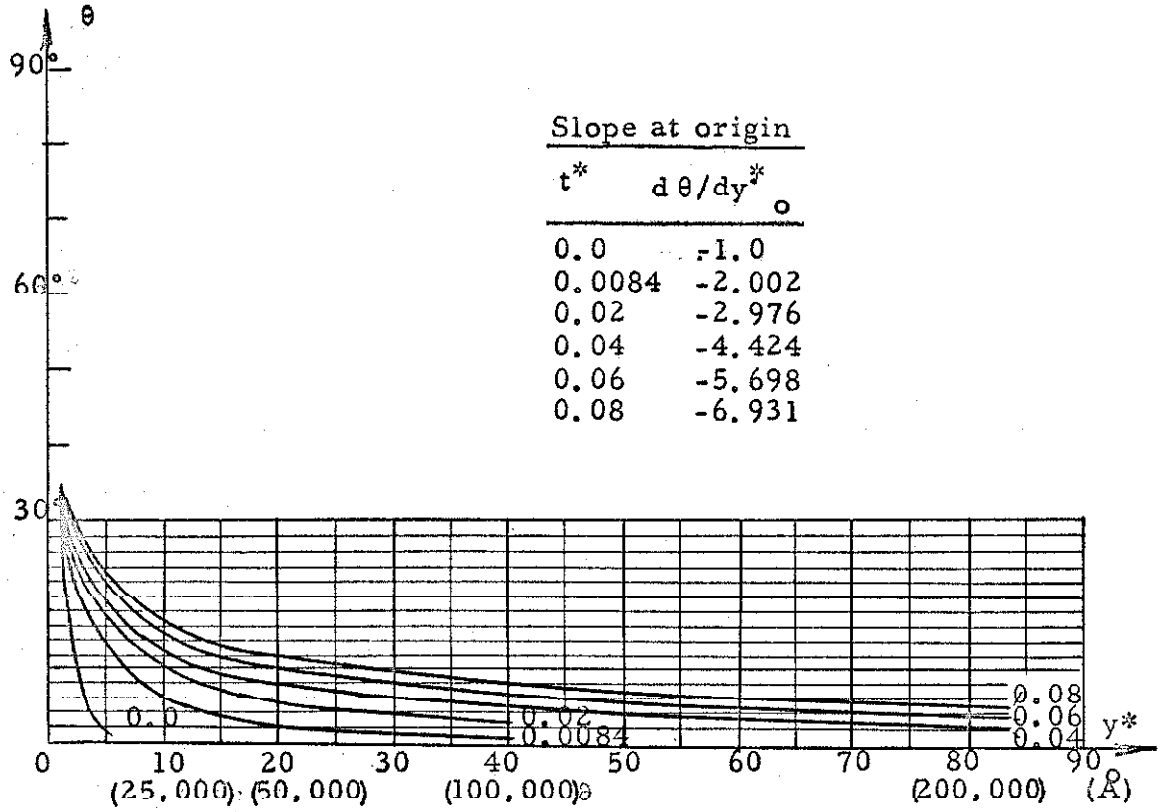

Slope at origin

t^*	$d\theta/dy^*_o$
0.0	-1.0
0.0084	-2.002
0.02	-2.976
0.04	-4.424
0.06	-5.698
0.08	-6.931

Fig. 3-20a

Shape of a Néel wall for t* = 0; 0.0084; 0.02; 0.04; 0.06; 0.08

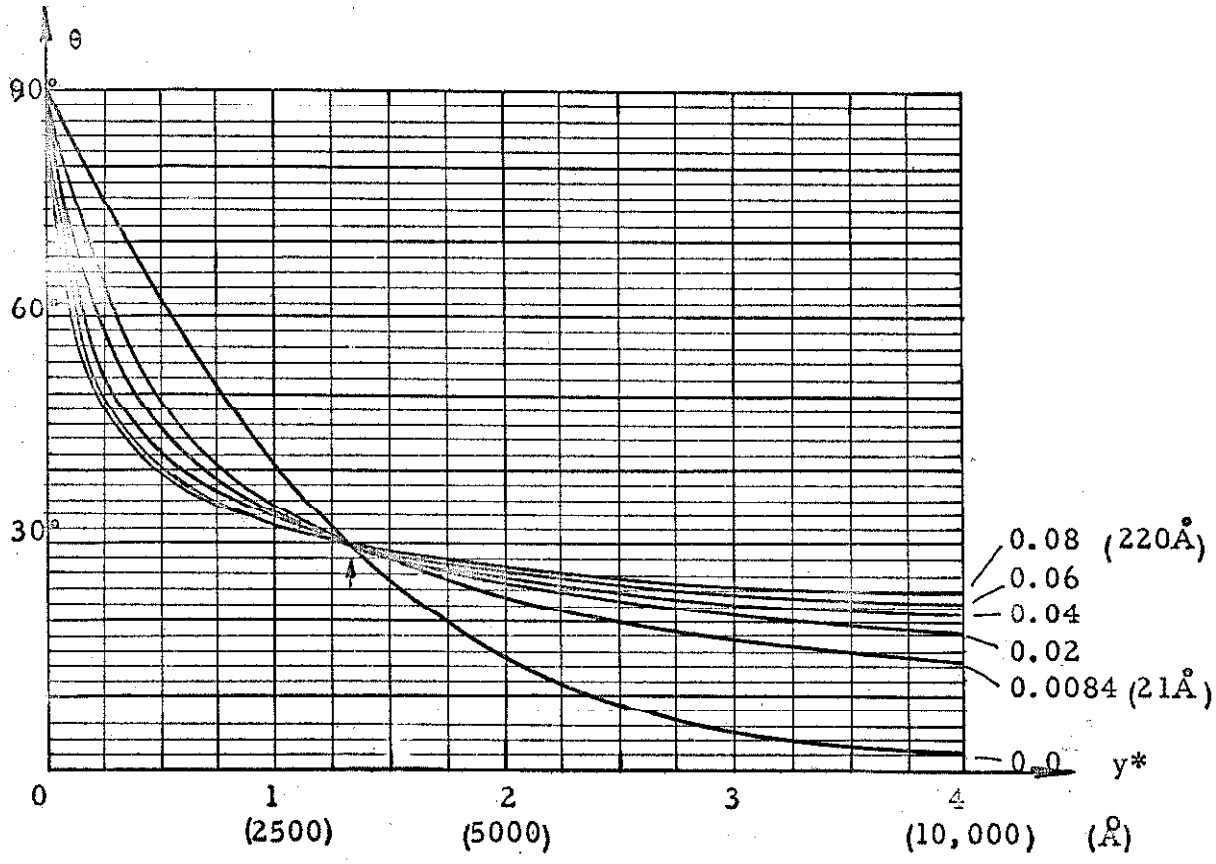

Fig. 3-20b

Shape of a Néel wall for same thicknesses (enlarged)

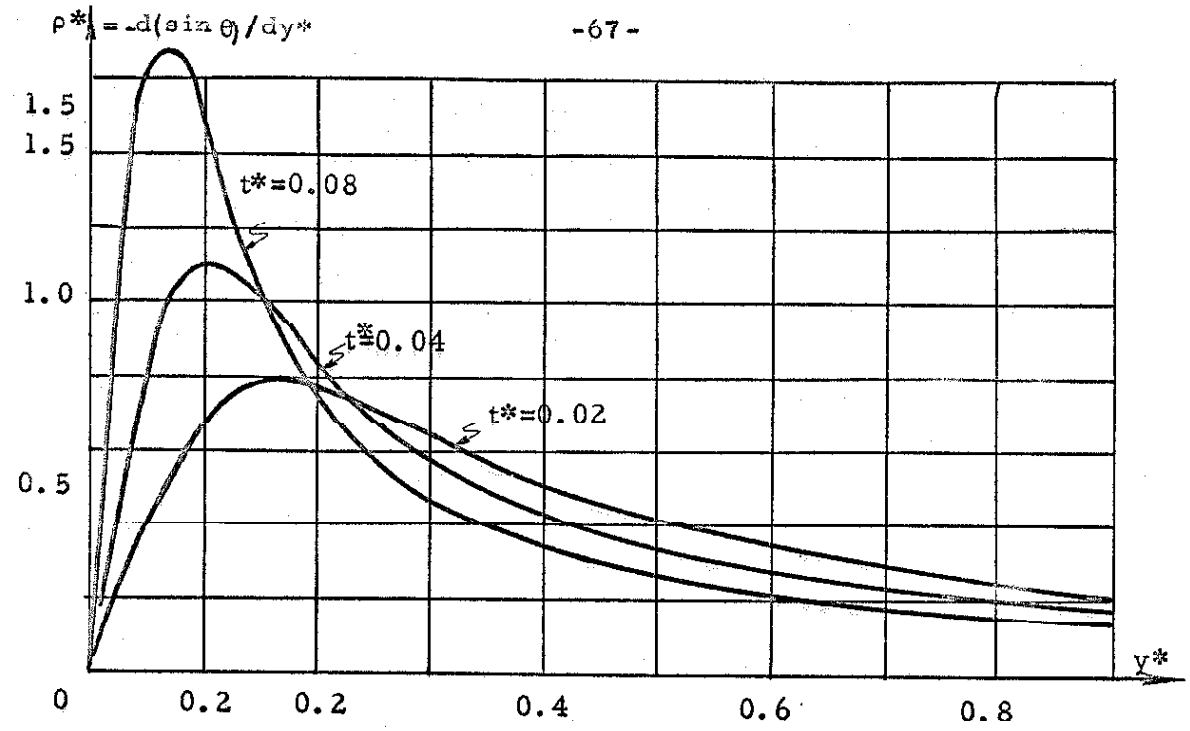

Fig. 3-21

Pole distribution close to the origin (t* = 0.02, 0.04, 0.08).

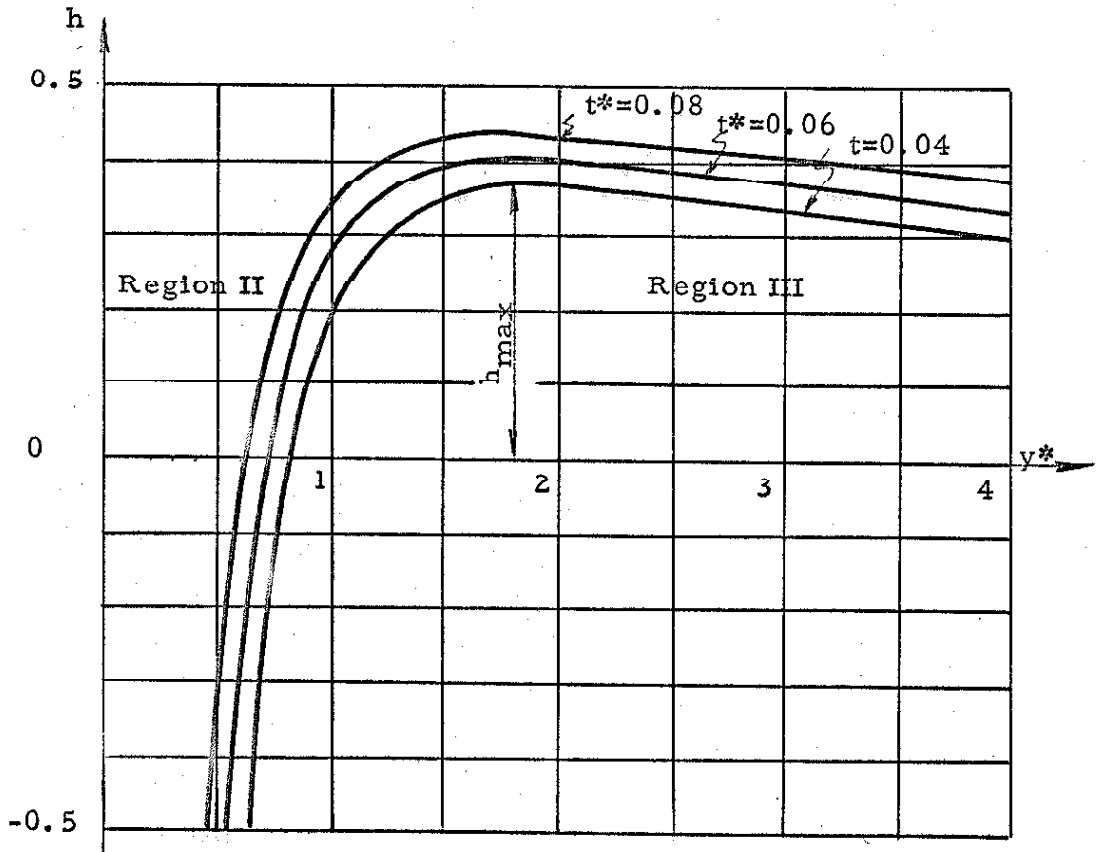

Fig. 3-22

Reduced field close to the origin (t* = 0.02; 0.04; 0.08)

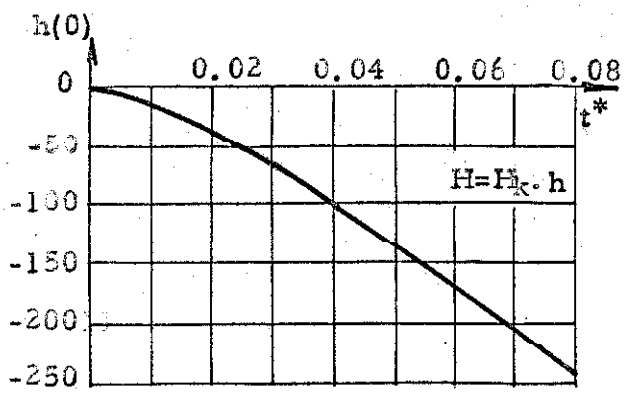

Fig. 3-23

Internal field at origin as a function of reduced thickness t^*.

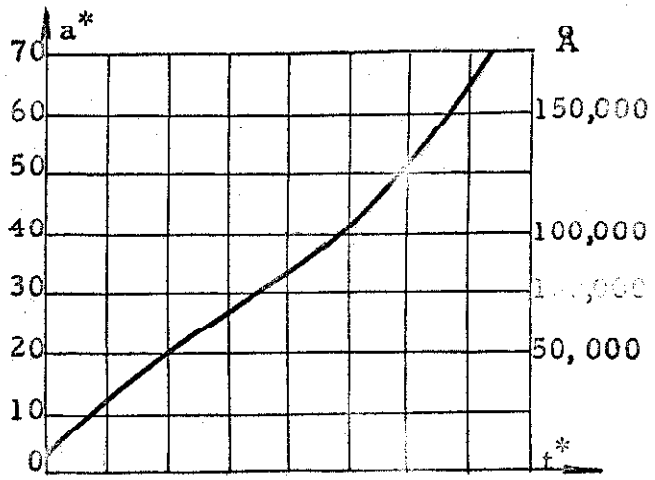

Fig. 3-24

Half-width of Néel walls (rotation of 85°) as a function of t^*.

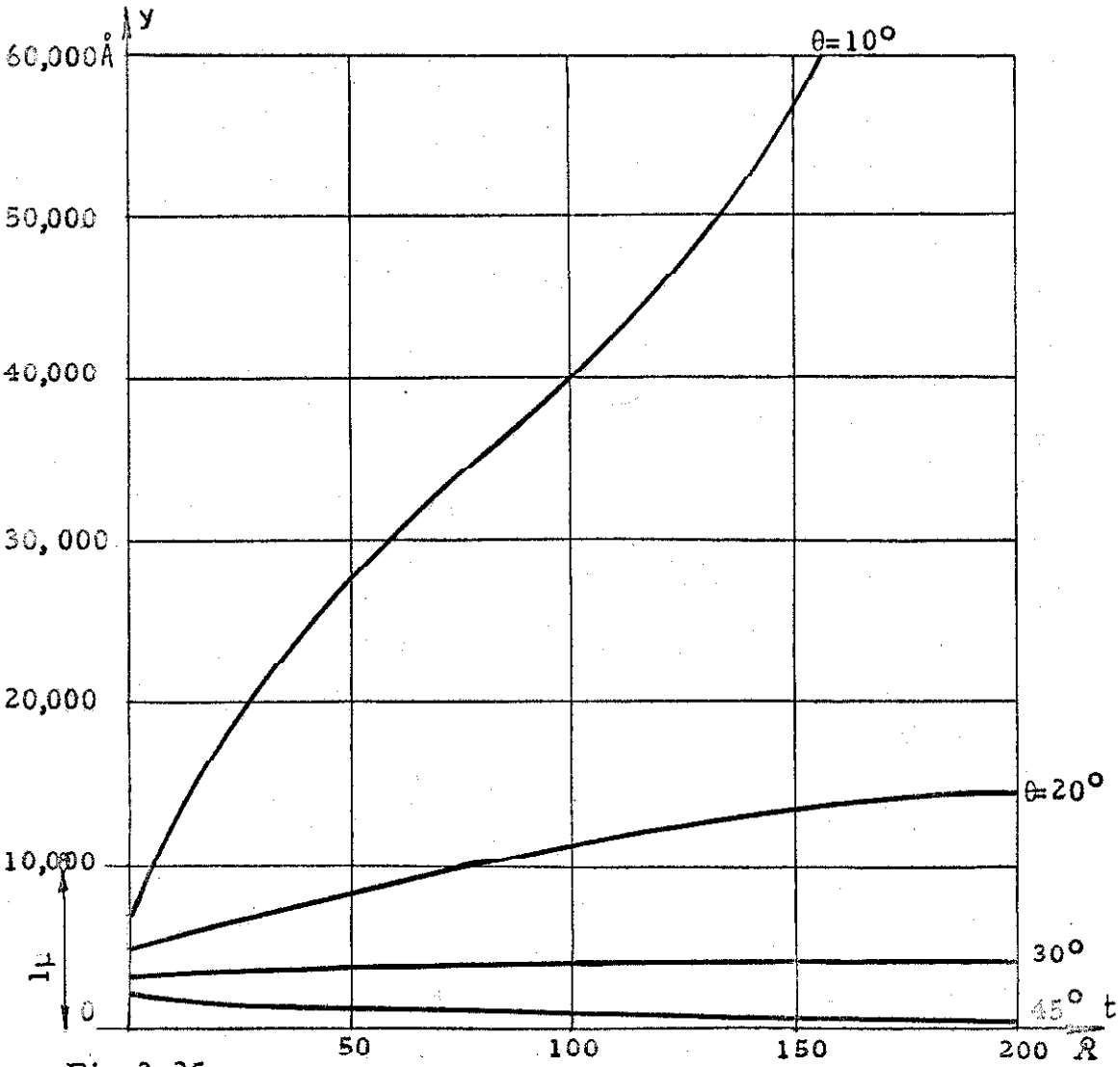

Fig. 3-25

Distance along the y axis corresponding to a rotation from 0=90° to, respectively, θ=45°, 30°, 20°, 10°.

of the wall and the point where θ = 10°, 20°, 30° and 45°; the values adopted for M, K and A are those mentioned at the beginning of this section. Ten degrees is certainly a meaningful angle, and it can be seen how a Néel wall widens with increasing thickness, although a first portion of the rotation, from 90° to 30°, occurs over a distance of the order of 4000 Å, this figure being approximately the same for all values of t. Figure 3-25 should be compared to Figure 3-6, where Middelhoek's results, based on the Néel model, shows a systematic decrease of the "total width" (60% from 0 Å to 200 Å). The important feature of these walls is their exceptionally long "tail." Wall widths are generally thought of in terms of thousands of Angstroms, whereas, in this case, 2a is evaluated in terms of microns. A direct experimental observation of the presence of a fast and a slow rotation region was apparently obtained by Fuchs (23) by studying films with the electron-microscope method developed by Hale, Fuller and Rubinstein (22). A quantitative measurement through such an experiment was only possible for the central portion of the wall and its total width could not be determined. One of the films studied by Fuchs was 270 Å thick and made of 81-Permalloy. Figure 3-26 reproduces the experimental curve $\theta(y)$ in the neighborhood of the origin, and it is seen that a total rotation of 90° occurs over a distance of 1450 Å, and that the knee of the curve appears at θ = 30° approximately. These results are compared with the curve $t^* = 0.08$

(210 Å) in Figure 3-20b. The agreement is rather satisfactory considering, for instance, that the exchange constant A is not known with accuracy (experimental values vary by more than 100%) and that the calibration of Fuchs's method might not be precise.

An indirect demonstration of the large width of the Neel configuration possibly exists since 1958, when Huber, Smith and Goodenough (18) discovered cross-tie patterns and identified them as juxtaposed segments of Néel walls with alternating clockwise and anti-clockwise rotations (Chapter 4).

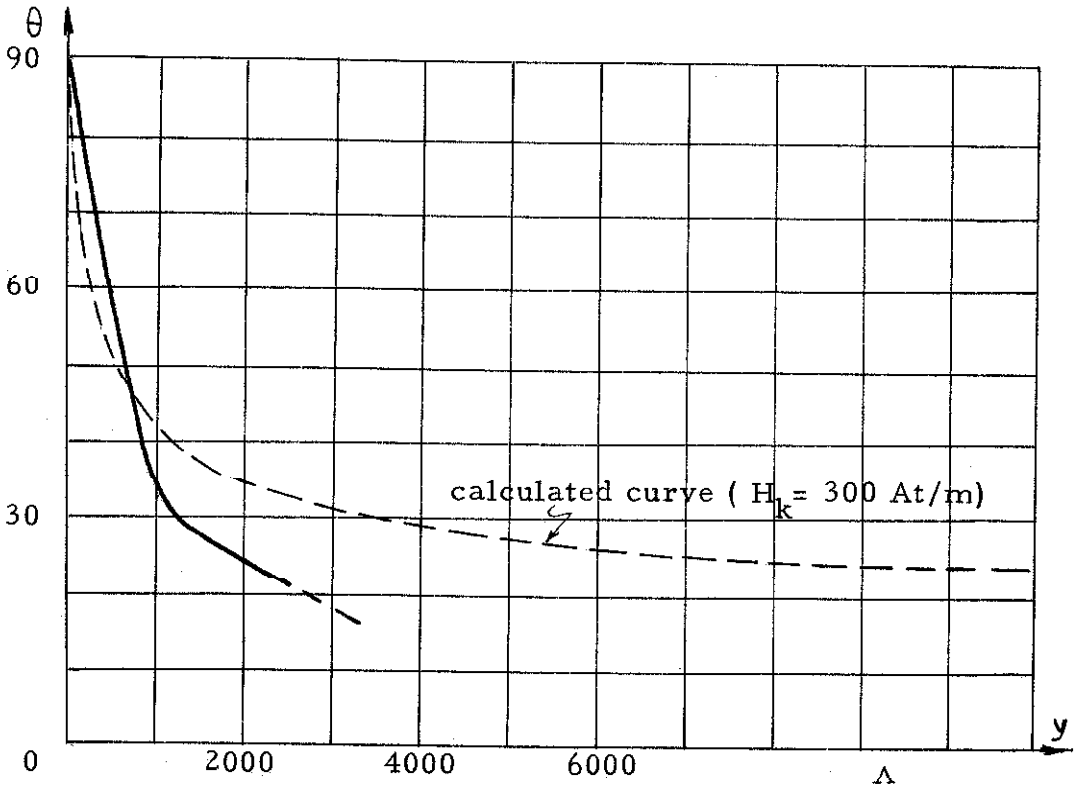

Fig. 3-26 Experimental curve θ(y) obtained by Fuchs compared to theoretical curve . (The exchange constant A, the anisotropy field H_k are unknown).

3.7 Energy Stored Inside a Néel Wall

The sum of the three energy terms corresponding to the three torques appearing in equation (3.6-4) constitutes the total energy density stored inside the wall if phenomena such as magnetoelasticity or microscopic crystalline anisotropy are neglected, as was done in the determination of the shape of the wall. Thus, at any point in the layer, the volume energy density will be, from equations(2.2-1), (2.3-6) and (2.4-1):

$$\epsilon(y) = A(d\theta/dy)^2 + K \sin^2\theta - \frac{\mu_o}{2} M H_y \sin\theta \qquad (3.7\text{-}1)$$

where the first, second and third terms represent, respectively, the exchange, anisotropy and internal magnetostatic energies. This energy density varies along the y axis perpendicular to the wall, since the direction of magnetization has been assumed constant throughout the thickness of the film (z axis). Recalling the reduced units $y^* = y/(A/K)^{\frac{1}{2}}$ and $h = H/H_K = \mu_o M H/2K$, $\epsilon(y)$ can be rewritten as follows:

$$\epsilon(y^*) = K\left[\left(\frac{d\theta}{dy^*}\right)^2 + \sin^2\theta - h(y^*) \sin\theta \right]$$

$$= K\left[(d\theta/dy^*)^2 + \tan\theta \cdot (d^2\theta/dy^{*2}) \right] \qquad (3.7\text{-}2)$$

since $\sin\theta - h(y^*) = \frac{1}{\cos\theta} \cdot \frac{d^2\theta}{dy^{*2}}$, as derived from equation (3.6-4).

The total energy per unit length of wall is therefore:

$$E = t \int_{-\infty}^{+\infty} \epsilon(y)dy = 2t(A/K)^{\frac{1}{2}} \int_{o}^{\infty} \epsilon(y^*)dy^*$$

$$= 2t(AK)^{\frac{1}{2}} \int_{o}^{\infty} [\ (d\theta/dy^*)^2 + \tan\theta(d^2\theta/dy^{*2})\ ]dy^* \qquad (3.7\text{-}3)$$

Usually the literature refers to the surface energy density of the wall $\gamma = E/t$. The reduced unit $\gamma^* = \gamma/(AK)^{\frac{1}{2}}$ will be used hereafter.

From $y^* = 0$ to infinity, θ varies from 90° to 0° and, for large y^*, $\tan\theta \simeq \theta$. The limits of integration can therefore be slightly modified. Indeed, noticing that:

$$\int_{Y^*}^{\infty} [\dot{\theta}^2(y^*) + \theta(y^*) \cdot \ddot{\theta}(y^*)]\ dy^*$$

$$= \theta(y^*)\ \dot{\theta}(y^*)\ \Big|_{Y^*}^{\infty} = -\ \theta(Y^*)\ \dot{\theta}(Y^*)$$

the integral (3.7-3) becomes:

$$\gamma^* = \frac{E}{t(AK)^{\frac{1}{2}}} = 2\left[\int_{0}^{Y^*} (\dot{\theta}^2 + \ddot{\theta} \cdot \tan\theta)dy^* - \theta(Y^*)\ \dot{\theta}(Y^*) \right] \qquad (3.7\text{-}4)$$

where Y^* is chosen sufficiently large so that the assumption $\tan\theta \simeq \theta$ is valid.

The preceding integral (3.7-4) is expressed solely in terms of $\theta(y^*)$, whereas the initial expression (3.7-1) contained the field $h(y^*)$ explicitly. The integrand is readily calculable, the function $\sin\theta(y^*)$ having been determined numerically for given thicknesses (Section 3.6) and stored on perforated cards (Appendix B). At $y^* = 0$, $\tan\theta$ and $d^2\theta/dy^{*2}$ become, respectively, infinite and zero; however, their product has a finite value:

$$\tan\theta \cdot (d^2\theta/dy^{*2})\,|_0 = 1 + |h(o)|$$

as found from the torque equation (3.6-4), where $\sin\theta(o) = 1$. The field $h(0)$ has been previously calculated when determining the shape of the wall (Fig. 3-23).

When t^* tends toward zero, the torque equation becomes $\ddot{\theta} = \sin\theta\cos\theta$, or, after multiplying both sides by $\dot{\theta}$, integrating between y^* and infinity ($\theta = \dot{\theta} = 0$ at $y^* = \infty$), and taking the minus sign for the square root of $\sin^2\theta$:

$$d\theta/dy^* = -\sin\theta$$

From equation (3.7-1), it is seen that γ^* itself tends to

$$\gamma^*_{t\to 0} = 2\int_0^\infty (\dot{\theta}^2 + \sin^2\theta)\,dy^*$$

$$= -4\int_{\pi/2}^{0} \sin\theta\, d\theta = 4$$

The shape of the wall, that is the function sin $\theta(y^*)$, is known for several reduced thicknesses between $t^* = 0$ and 0.08. These functions are stored as tables of values for discrete positive abscissae y^*, sin θ varying from one to zero. The energy constant of the wall was determined by numerical integration using the trapezoidal rule over finite intervals Δy^*. Thus:

$$\gamma^* = 2\left[\sum_{0}^{Y^*}\left[\left(\Delta\theta/\Delta y^*\right)^2 + \tan\theta\left(\Delta^2\theta/\Delta y^{*2}\right)\right]\Delta y^* - \theta(Y^*)\dot{\theta}(Y^*)\right] \tag{3.7-5}$$

Appendix C gives details concerning the numerical method, the change of interval at $y^* = Y_1$ from Δy^*_1 to Δy^*_2, as well as the Fortran program.

As an indication of the precision of the numerical formulas used, the energy density γ^*_0 at $t^* = 0$ has first been computed and found to be 3.86 as compared to 4, which is the value determined analytically above. The calculated value is 3.5% below the expected figure. For increasing thicknesses, the general shape of the wall (Fig. 3-19a) is preserved, but the rotation occurs over a much larger distance. Thus, for cases where $t^* > 0$, the function $d\theta/dy^*$ varies more smoothly over the major portion of the abscissa axis and the systematic error accumulated during the integration process will at most be of the order of that one found in the test case $t^* = 0$. The present study of the energy content of the wall does not call for more

elaborate numerical analysis in order to increase the absolute accuracy of γ^* . In fact, only relative values are meaningful. Indeed, the analytical expression (2.2-1) used for the exchange energy is approximate. Furthermore, no satisfactory method is available to determine the exchange constant A with certainty; measurements differ by up to 50%.

Figure 3-27 is a graph of the reduced energy density γ^* as a function of the reduced thickness t^* up to 0.08 for the case $C = M/\pi H_k = 845$. On Figure 3-28, three sets of results are compared: those obtained in this section for the usual values $A = 10^{-11}$ J/m, $\mu_o M = 1$ Wb/m^2, and $K = 150$ J/m^3, and those found by Néel (17) for the same values of the constants (see Fig. 3-3). Middelhoek's calculations are also reported, although they correspond to a slightly different value of K (100 J/m^3). It is seen that the figures of this thesis are systematically less than the previous ones; this is due to the fact that in regions I and III, that is for quite a sizable portion of the rotation, the energy density is very small (Section 3.4).

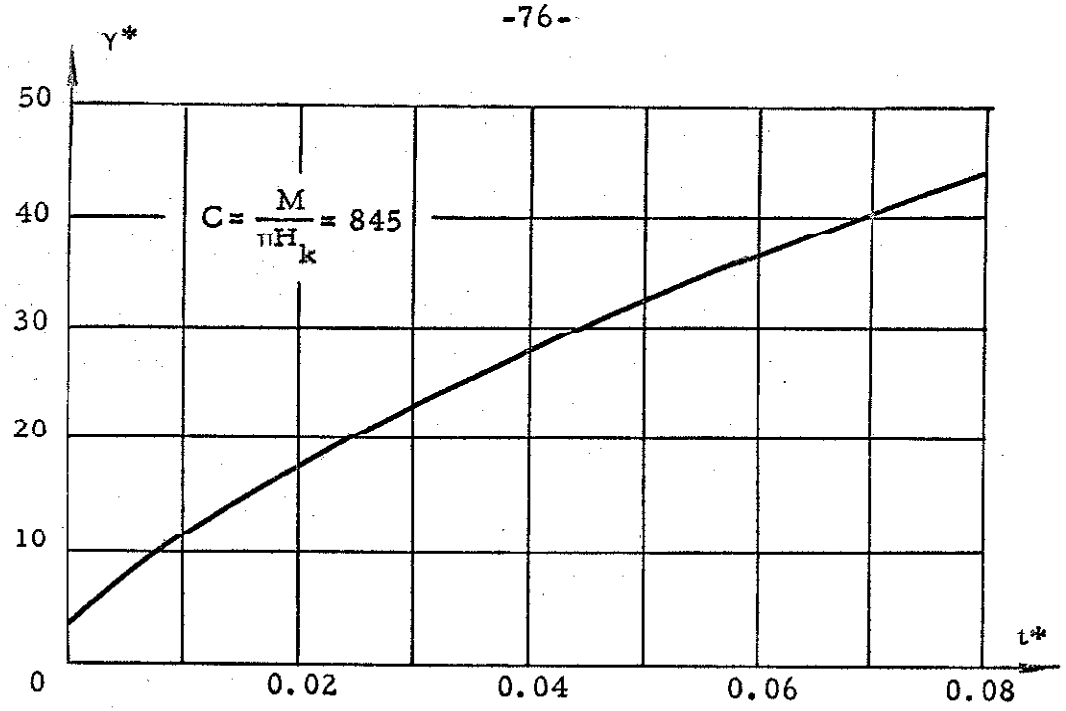

Fig. 3-27

Reduced energy density $\gamma^* = E/t(AK)^{\frac{1}{2}}$ of Néel walls as a function of thickness

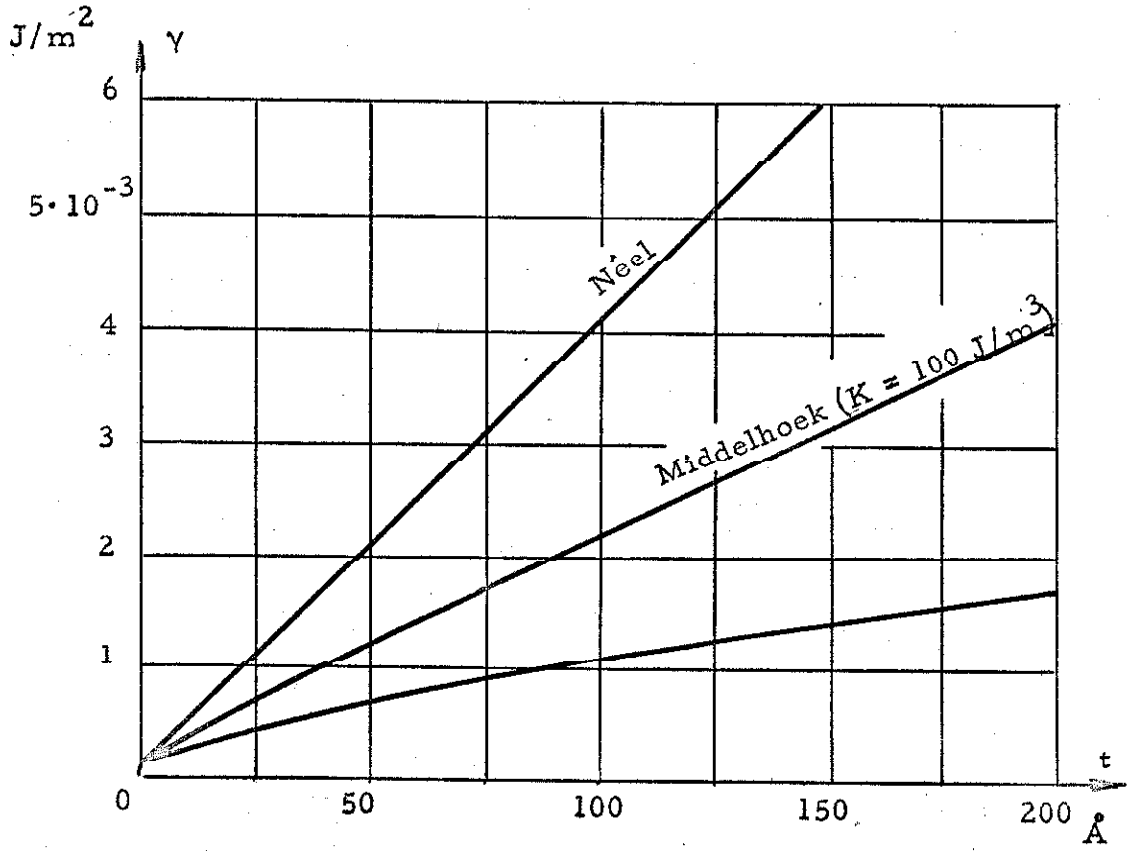

Fig. 3-28

Energy density of Néel walls as a function of thickness (Néel's and Middelhoek's results are also indicated)

4. DOUBLE WALLS AND CROSS-TIE WALLS

4.1 Double Walls

The so-called double wall configuration was first observed in very thin films by Williams and Sherwood (24). Thereafter, it was recognized that two Néel walls, parallel to each other and of opposite polarities, would lead to such a pattern (25). If this interpretation was correct, the total rotation of magnetization would be 360° occurring in two separate stages of 180° each. Therefore, one obvious method of studying this problem is to consider the interaction of two Néel walls, thus taking advantage of the results of Chapter 3. Using the Bitter technique (3) as a tool of experimental investigation, the parallel traces which locate the axes of the nearby walls (at $\theta = 90°$ and 270°) are found to be separated by a distance of the order of a few microns in the absence of an external field. The purpose of the present section is to reconcile the magnitude of this spacing with the width of a 180° wall as found from the previous study of Néel walls.

The thickness at which 360° walls are best observed is approximately 100 Å when there is still enough material left to create a continuous trace of colloid. Above that value of thickness, the pattern

apparently becomes unstable and is not observed. Several authors (11, 26) have observed double walls as well as their behavior in the presence of an external field. Feldtkeller and Liesk (27), using the Lorentz microscopy technique with the electron microscope (22), have directly confirmed the presence of 360° walls in films of such thickness. It will simply be assumed here that such a wall is formed by bringing together two Néel walls under the influence of a field along the easy direction and of appropriate sign. If three domains of alternating directions are separated by two parallel walls, as in Figure 4-1, and a field H_{ex}, of the order of the coercive force, is applied favoring domains "1" and "3," the central portion "2" will shrink, and the two walls will interact.

The study of Néel walls in Chapter 3 has shown how far the internal field H_i extends along the y axis. The shape, as well as the internal field, of a 180° wall in a 100 Å film ($t^* = 0.04$) was shown in Figure 3-16a. Evidently two cases may occur: either walls "1" and "2" have identical polarities (Figure 4-2a) or opposite ones (Figure 4-2b). In the first case, they will attract each other, whereas in the second, they will repel. In other words, it will be shown that the interaction energy will respectively decrease or increase if the distance 2d, separating "1" and "2," decreases.

The total energy of the system, made up of the domains and the walls under the influence of an external field, is difficult to determine. In fact, the shape of each wall will be altered not only by

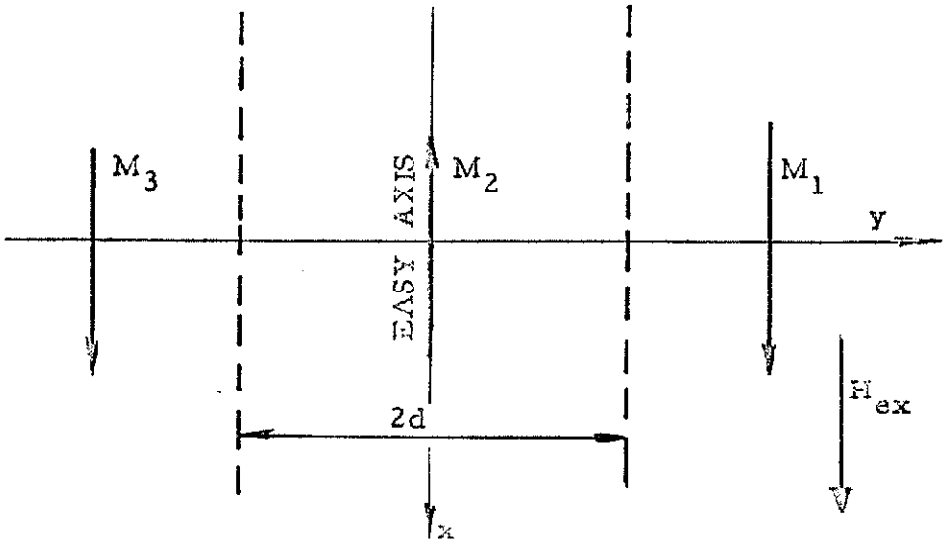

Fig. 4-1

Two Néel walls separating three domains and brought together under the influence of a field H_{ex}.

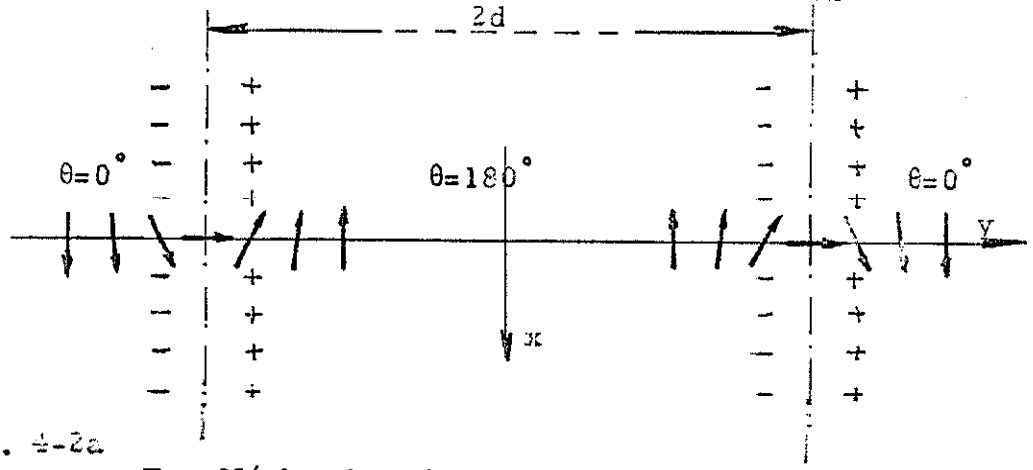

Fig. 4-2a

Two Néel walls of identical polarities
(total angle of rotation : 0°)

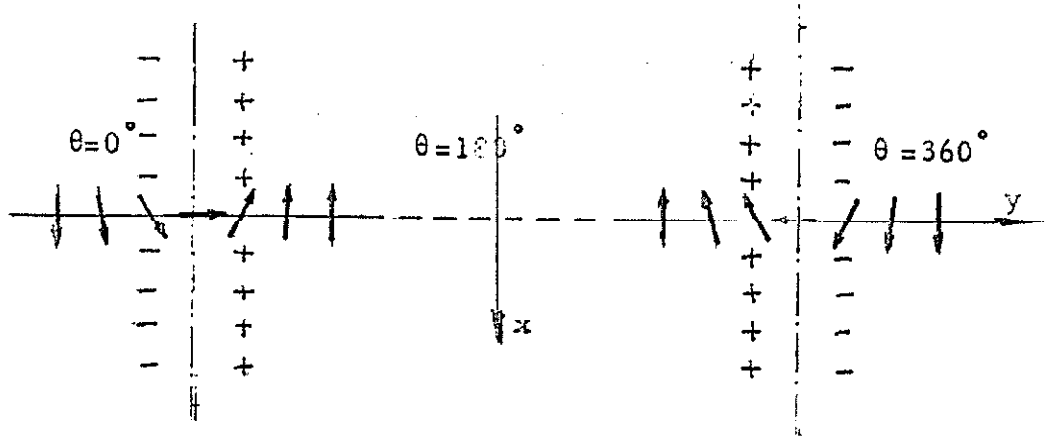

Fig. 4-2b

Two Néel walls of opposite polarities
(Total angle of rotation : 360 °)

their mutual interaction, but also by the field H_{ex}, whose amplitude is comparable to the anisotropy field H_k, and which therefore should play a role not at all negligible in determining the direction of $\vec{M}$ in the slow rotation regions (regions I and III of Section 3.3). No study, except a rigorous one, similar to that of Section 3.6, would produce accurate results. Furthermore, since in this case wall motion occurs, the propagation field H_w or coercive force (see Section 5.2.1) has to be taken into account as well.

Considering the case of Figure 4-2b, and basing the reasoning on the knowledge of the internal field in a single Néel wall, the situation can be represented approximately as in Figure 4-3. When the two walls are sufficiently far apart, they do not interact, which will be the case when 2d is larger than 2a, the width of one wall. The width 2a is equal to 17 μ for t = 100 Å (Figure 3-24). Supposing that the distance 2d decreases, the walls then start interacting. The energy density at every point can be obtained from equations (2.2-1), (2.3-8) and (2.4-1) (see Fig. 4-4).

$$\epsilon(y) = A(d\theta/dy)^2 + K \sin^2\theta - \frac{\mu_o}{2} M H_i \sin\theta - \mu_o M H_{ex} \cos\theta$$

The corresponding torque equation is:

$$2A \frac{d^2\theta}{dy^2} - K \sin 2\theta + \mu_o M H_i \cos\theta - \mu_o M H_{ex} \sin\theta = 0 \qquad (4.1\text{-}1)$$

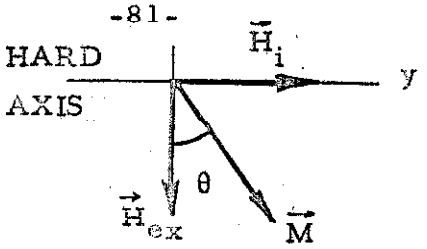

Fig. 4-4

Directions of internal and external fields

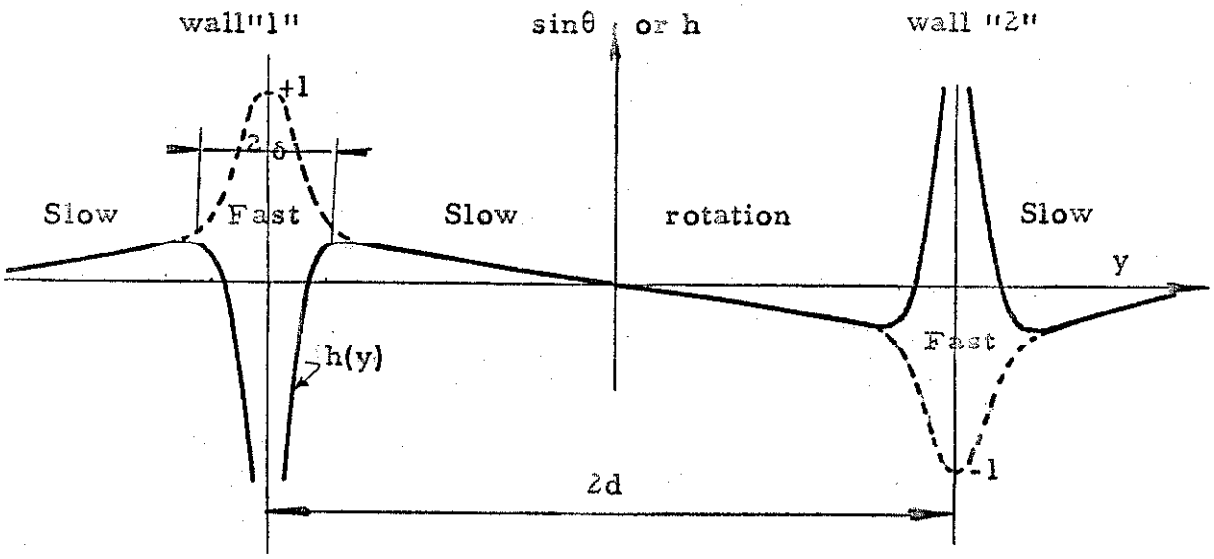

Fig. 4-3

Field distribution in a double wall showing the regions of fast and slow rotations

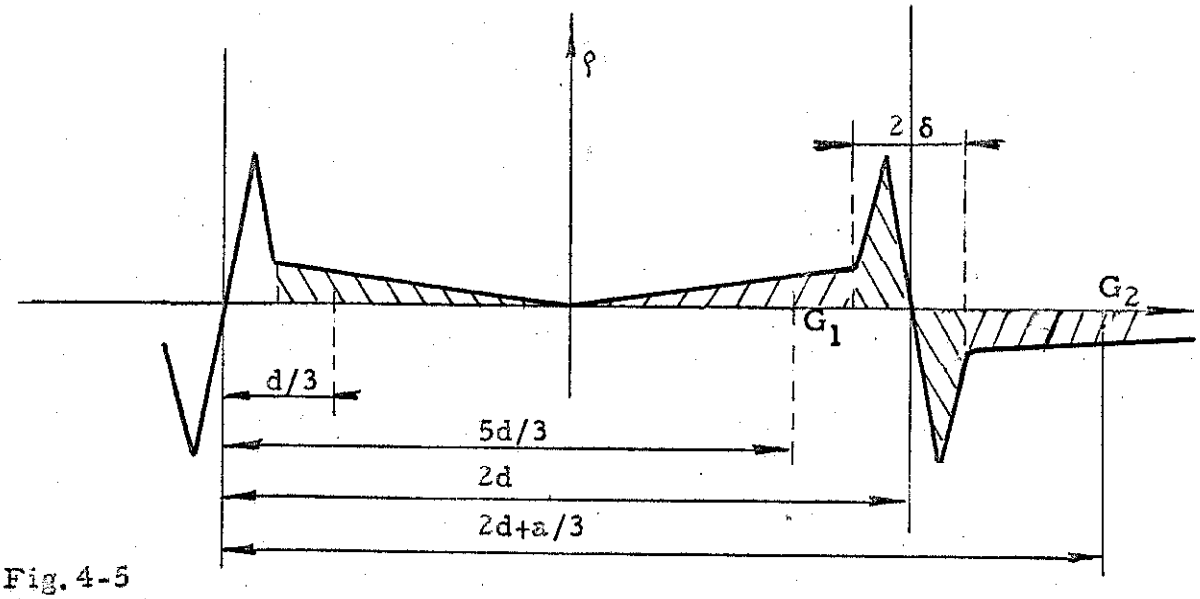

Fig. 4-5

Simplified pole distribution in a double wall

with the following boundary conditions for the direction of $\vec{M}$:

$$\text{at } y = 0,\ \theta = 180^\circ \text{ and at } y = \infty,\ \theta = 360^\circ$$

and

$$H_i = \frac{M}{\pi} \int_{-\infty}^{+\infty} \frac{d(-\sin\theta)}{d\eta} \arctan\left[\frac{t}{2(y-\eta)}\right] d\eta$$

The function $\sin\theta$ is antisymmetrical with respect to $y = 0$, the center point between the walls. A numerical solution, analogous to that of Section 3.6 in the case of a single Néel wall, could probably be obtained, but such a problem, although still unidimensional, would be more complicated yet.

When d decreases but is still large enough so that the shape of each wall is not excessively disturbed (Figure 4-3), an approximate treatment will yield the order of magnitude of the interaction energy. Excluding any term due to an external field, the energy of the 360° wall is:

$$E = E_a + E_b + 2\,E_{ab}(d)$$

where $E_a = E_b$ is the energy of one wall when d is infinite and $2\,E_{ab}(d)$ the additional term representing the interaction as a function of d. Recalling the remark of Section 3.4, it may be assumed that in the slow rotation regions, the energy density is approximately zero, provided the influence of the external field is neglected. The central regions around $y = \pm d$ are not appreciably disturbed by the presence of the neighboring wall. It can therefore be concluded that the

interaction is mainly magnetostatic and is described by:

$$E_{ab} = -\frac{\mu_o}{2} Mt \int_{-d-\delta}^{-d+\delta} \Delta H_i \sin\theta \, dy$$

where 2δ is the extent of the region in wall "1" where $\sin\theta$ and $h(y)$ depart from each other (fast rotation). The quantity ΔH_i in the central region $(-d-\delta)$ to $(-d+\delta)$ is the difference between the field of a single 180° wall and the field due to the pole distribution of a double wall as represented schematically in Figure 4-5. For calculating the field at one wall, the ρ diagram of the other wall can be thought of as made of a dipole of strength $Mt\delta\,(1 - \sin\theta_\delta)$ and two triangular distributions with centroids at G_1 and G_2.

Assuming a uniform value of ΔH_i over the interval 2δ, E_{ab} becomes:

$$E_{ab} = -\frac{\mu_o}{2} Mt \cdot \Delta H_i \cdot 2\delta \, (\sin\theta)_{av} \qquad (4.1\text{-}2)$$

An approximate value can be derived for ΔH_i:

$$\Delta H_i = -\frac{Mt}{2\pi}\left[\left(\frac{1}{d/3} - \frac{1}{a/3}\right)\sin\theta_\delta + \frac{\sin\theta_\delta}{5d/3} + \frac{\delta(1-\sin\theta_\delta)}{4d^2} - \frac{\sin\theta_\delta}{2d+a/3}\right] \qquad (4.1\text{-}3)$$

The first term accounts for the deformation of the slow rotation region of wall "1" and the other terms for the presence of wall "2."

In the presence of an external field parallel to the easy direction, assuming that the energies E_a and E_{ab} are unchanged, the

equilibrium distance between the two walls will be given by the following equation, expressing the static equilibrium condition:

$$\frac{\partial E}{\partial(2d)} = \frac{\partial(2\ E_{ab})}{\partial(2d)} + 2\mu_o\ Mt\ H_{ex} + \frac{\partial \Delta\ E_w}{\partial(2d)} = 0 \qquad (4.1\text{-}4)$$

In this equation, $2\ \mu_o\ Mt\ H_{ex}\ \partial(2d)$ represents the variation in external magnetostatic energy in the domain configuration of Figure 4-1 due to a wall displacement, and ΔE_w is the random variation of energy which is the origin of the propagation field H_w of a wall (Section 5.2.1). From equation (5.2.2)

$$H_w = \frac{1}{2\mu_o M t} \left| \frac{\partial \Delta E_w}{\partial x} \right|_{max}$$

Equation (4.1-4) becomes:

$$2\mu_o\ Mt\ (H_{ex} \pm H_w) = -\frac{\partial E_{ab}}{\partial d} \qquad (4.1\text{-}5)$$

The positive sign corresponds to a decreasing field and the negative sign to an increasing one. For the case t = 100 Å, the following numerical values may be introduced in equations (4.1-2), (4.1-3) and (4.1-5):

$M = 8 \cdot 10^5$ A t/m, $\delta = 0.4 \cdot 10^{-6}$ m, $\sin\theta = 0.5$, $(\sin\theta)_{av} = 0.75$,

$a = 8.5 \cdot 10^{-6}$ m (from Section 3.6).

Thus, expressing d in microns:

$$\Delta H_i = -640\left[\frac{3.6}{d} - 0.35 + \frac{0.1}{d^2} - \frac{1}{2d + 2.8}\right]$$

$$E_{ab} = -0.3.10^{-6}\,\mu_o M t \Delta H_i$$

$$H_{ex} \pm H_w = 96\left[\frac{3.6}{d^2} + \frac{0.2}{d^3} - \frac{2}{(2d + 2.8)^2}\right] = F(d) \quad (4.1\text{-}6)$$

Figure 4-6 represents the function F(d). If H_w is measured experimentally, equation (4.1-6) gives an approximate relationship between 2d and H_{ex}. This variation is represented in Figure 4-7, and is obtained by translating the curve of Figure 4-6 by an amount equal to $\pm H_w$, which is equal to 1 oe in the example of Photograph D-1 (Appendix D).

For decreasing H_{ex}, one point is particularly easy to observe experimentally. It is the distance $2d_o$ to which the walls will repel each other when H_{ex} is brought back to a zero value. The value $2d_o$, predicted on the basis of this graph, is about 4μ. When the field increases, 2d does not tend asymptotically towards zero, but rather the double wall vanishes as soon as H_{ex} reaches the critical value H_e, the erasure field. This quantity H_e is not determinable on the basis of the present study. Indeed, as can be seen from Figure 4-2b, untwisting of the wall can only occur if $\vec{M}$ goes out of the plane of the layer.

Experimental observations have been made with the Bitter technique. The transparent film was illuminated from below and the

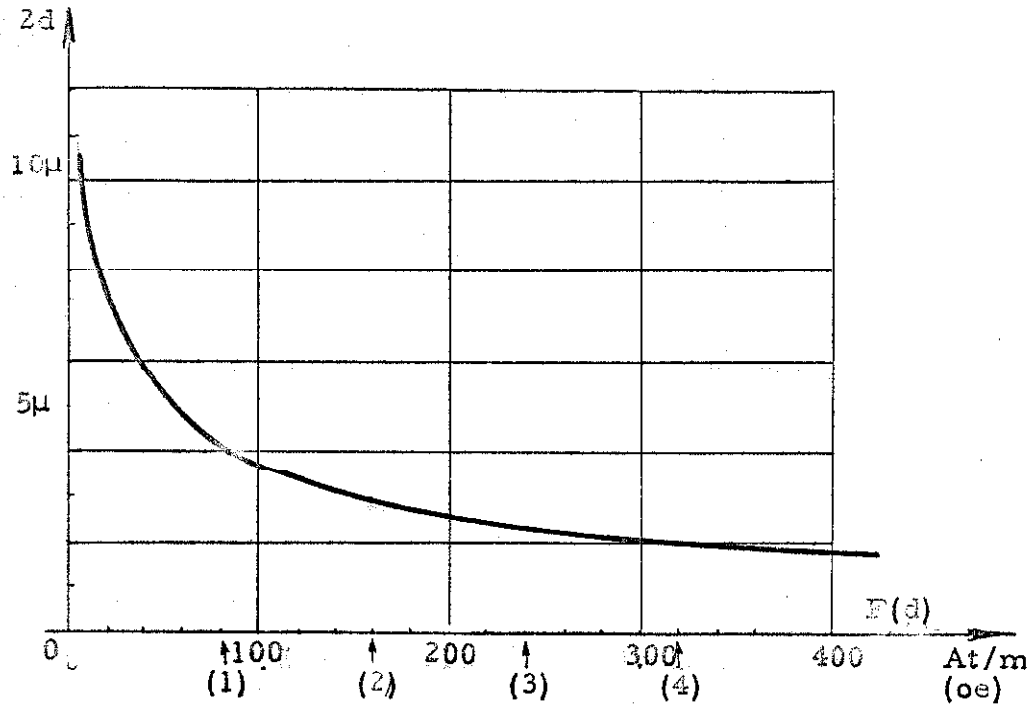

Fig. 4-6

F(d) as a function of 2d as given by equation(4.1-6)

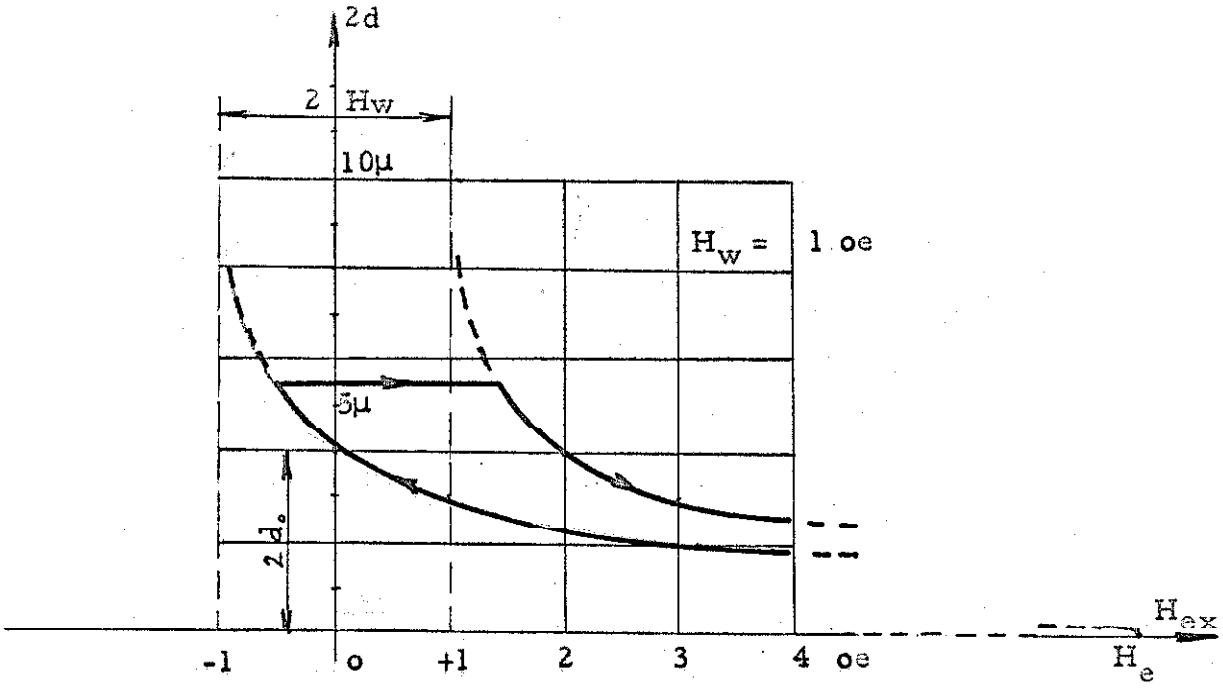

Fig. 4-7

Distance 2d between the axes of the walls as a function of H_{ex} (H_w= 1 oe)

colloid pattern observed with a phase contrast microscope. Photograph D-1a (Appendix D) shows a double wall in a zero field and Photograph D-1b represents the same configuration in a field of 13 oe almost equal to the erasure field H_e. In the latter case, the two traces are not separable with the colloid technique. When the external field is zero, the separation $2d_o$ is approximately equal to 3μ in this film. The thickness of the film could not be determined accurately, but is within 20% of 100 Å, this value being obtained from the saturation flux of the hysteresis curve.

Although double walls have not been studied in detail in this section, the relationship between them and single Néel walls has been clearly described. In particular, the experimental value $2d_o$ was compared with its theoretical equivalent, calculated approximately, and the agreement was satisfactory or even accidentally too good in view of the lack of accuracy of the analytical formulas. In any case, this section confirms the conclusions of Chapter 3, namely that Néel walls extend into the domains for distances of several microns.

4.2 Cross-tie Walls

4.2.1 General

Cross-tie walls were first observed by Huber, Smith and Goodenough (18) in films of intermediate thickness (200 Å to 1000 Å)

and, since then, by numerous other workers (20, 11, 28). The colloid patterns obtained with the Bitter technique appear as in Figure 4-8. No satisfactory explanation of the origin or even a proper description of cross-ties has been proposed yet. The scope of this section is to relate this two-dimensional pattern to the configuration of infinite Néel walls and to, therefore, account for the creation of transverse walls, their width 2ℓ, the distance 2 L separating them, and the variation of $\vec{M}$ in between.

The interpretation previously given to these colloid traces (18) is reproduced in Figure 4-9, where the local direction of magnetization is indicated. It has been correctly recognized that a succession of Néel wall segments alternately clockwise and anticlockwise is the "backbone" of the cross-tie configuration. Two different situations occur, depending on the polarities of the two adjacent Néel walls compared to the domain orientations. At a site such as "A," a sudden break in the magnetization direction appears accompanied by a transverse wall, whereas at "B," the lines of magnetization describe a flux closure pattern, and no cross-tie is observed there. Perhaps the most convincing demonstration of the presence of such alternating Néel segments has been furnished by Moon (19) using the Bitter technique. He applied a field of 50 oe perpendicular to the plane of the film and thereby modified the field distribution along the segments BA, AB', etc., that way creating a shift of the colloid traces, as in

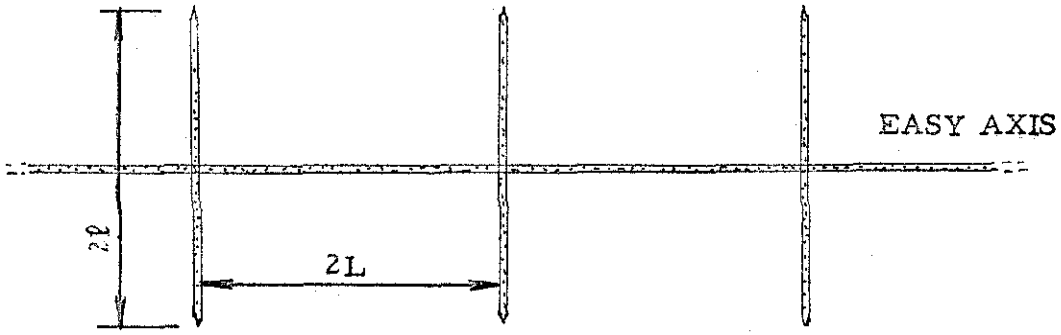

Fig. 4-8

Colloid trace of a cross-tie wall observed with the Bitter technique

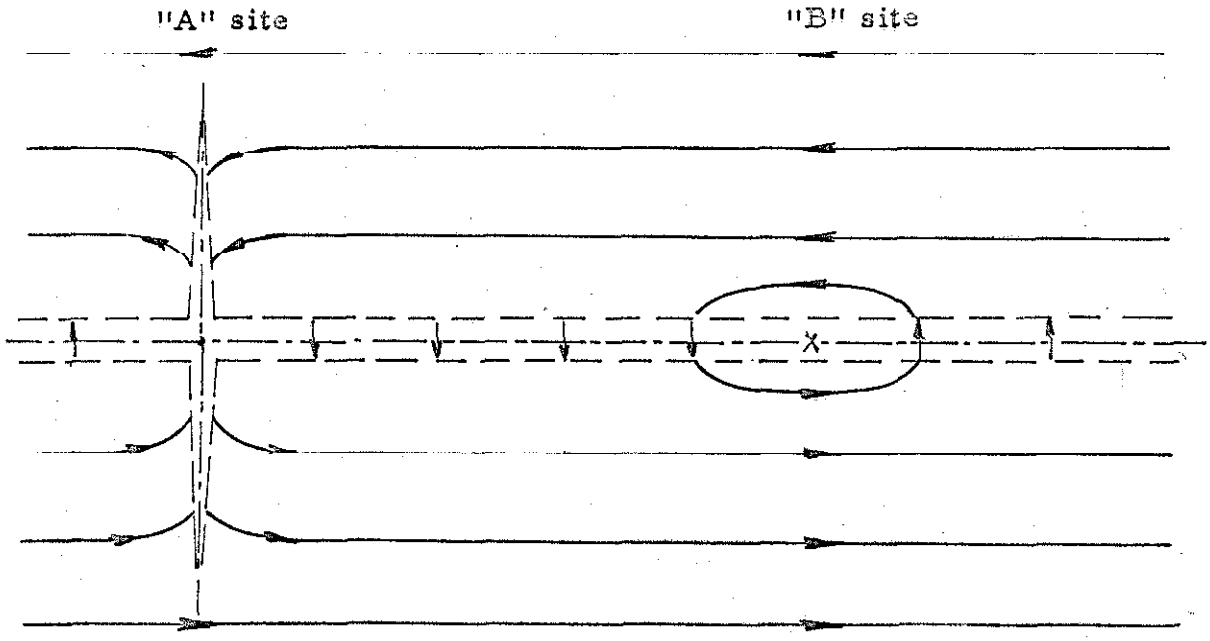

Fig. 4-9

Interpretation of the cross-tie configuration given by Huber, Smith and Goodenough

Figure 4-10. Methfessel, Middelhoek and Thomas (20) observed the changes of the wall character with decreasing film thickness showing that the length 2ℓ of a transverse wall reaches values over 10 microns. Middelhoek (11), using the model of Figure 4-9, attempted to compute the energy content of such walls in order to show that, above a certain thickness (Fig. 3-4), cross-ties become more favorable than pure Néel walls.

There always has been an apparent contradiction which probably was the reason why cross-ties have remained rather misunderstood: how could Néel walls, thought to have a width in the range of a thousand Angstrŏms, interact with each other and produce patterns as wide as ten microns (dimension 2ℓ of Fig. 4-8)? Chapter 3 has shown that the first part of this statement is not correct, since Néel walls were found to extend up to several microns in width.

A transverse wall can thus be thought of as resulting from the juxtaposition of two semi-infinite Néel walls of opposite polarities such that the field along the y axis is opposed to the magnetization vector inside the domains (Fig. 4-11a). On the other hand, if the signs of $\vec{M}$ and the field are the same, no cross-tie will be created (Fig. 4-11b). The considerable width of cross-tie walls, that is the length 2ℓ of the transverse walls, is thus accounted for by the dimensions of pure Néel walls themselves. Although, in the preceding chapter, calculations have not been pursued above the thickness of

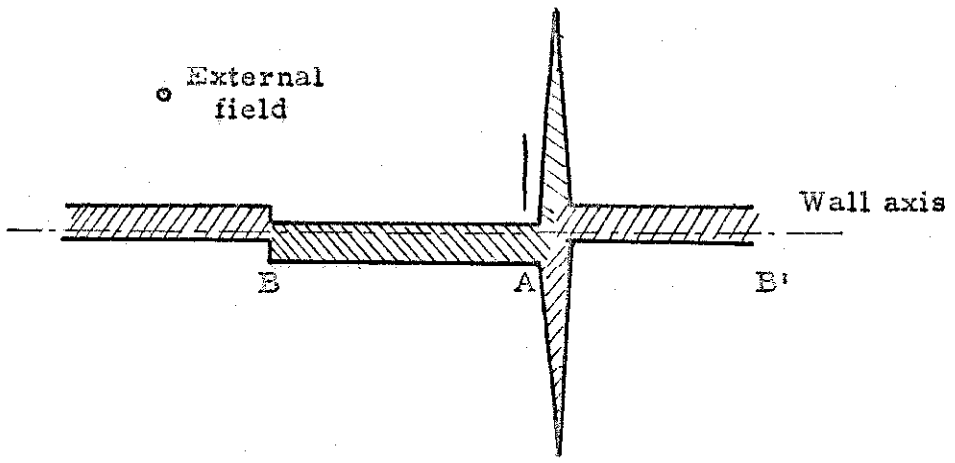

Fig. 4- 10

Moon's experiment showing the displacement of the colloid under the influence of a field perpendicular to the plane of the film

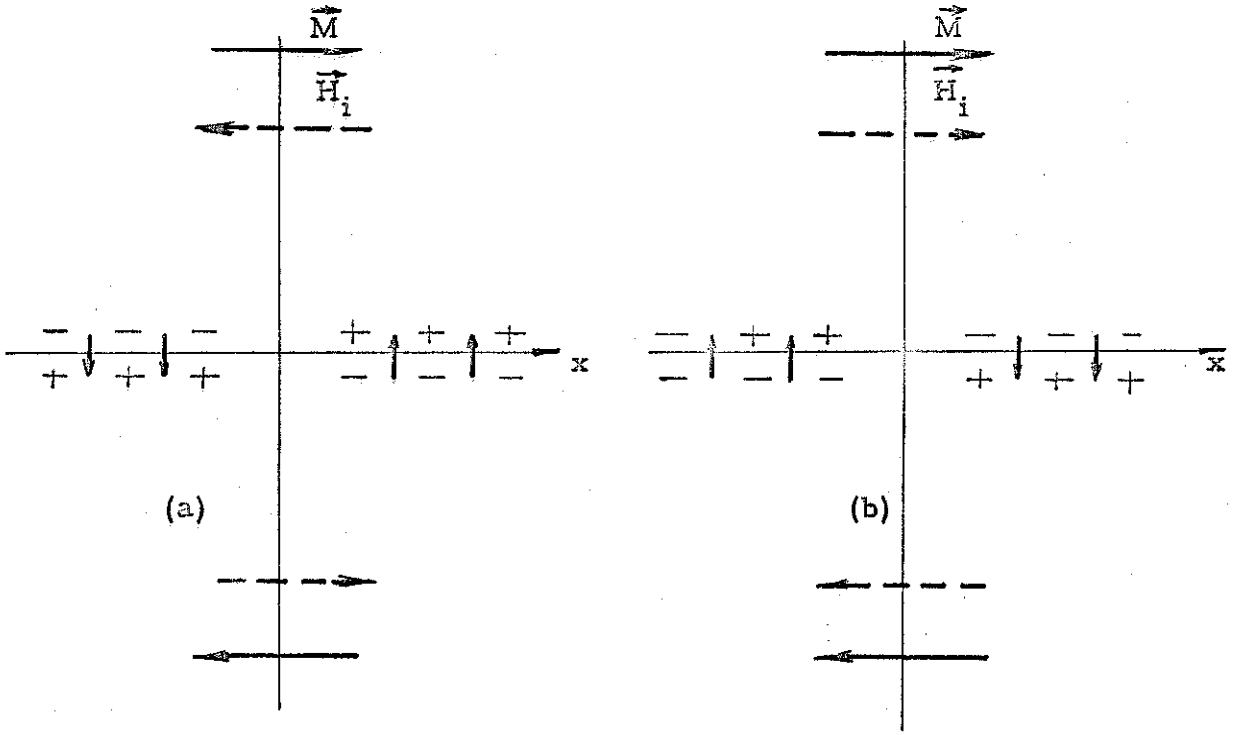

Fig. 4- 11a and b

Direction of the internal field H_i due to two semi-infinite Néel walls as compared to the direction of magnetization inside the domains

200 Å, infinite Néel walls, if they existed above that value of t, would extend farther yet into the neighboring domains. This is evident from Figures 3-24 and 3-25, as well as from the behavior of the reduced field h when t increases (eq. 3.6-5).

More realistic maps of the $\vec{M}$ field are those of Figures 4-12a, b and c, representing an "A" site, a "B" site, and a succession of these. They are based on the known behavior of the magnetization inside an infinite Néel wall from which they logically follow. They differ appreciably from Figure 4-9, where, the Néel walls being imagined much narrower, the appearance of a considerably wider cross-wall was in fact unexplainable and even illogical. Electron microscope observations by Liesk (29), showing clearly the ripple structure perpendicular to $\vec{M}$, are in full support of Figure 4-12.

4.2.2 Torque Equation of the Problem

If the problem were to be treated rigorously, a torque equation analogous to equations (3.6-4) and (4.1-1) should be solved. Two independent variables must now be introduced, x as well as y. The sum of the torques is zero everywhere. Thus:

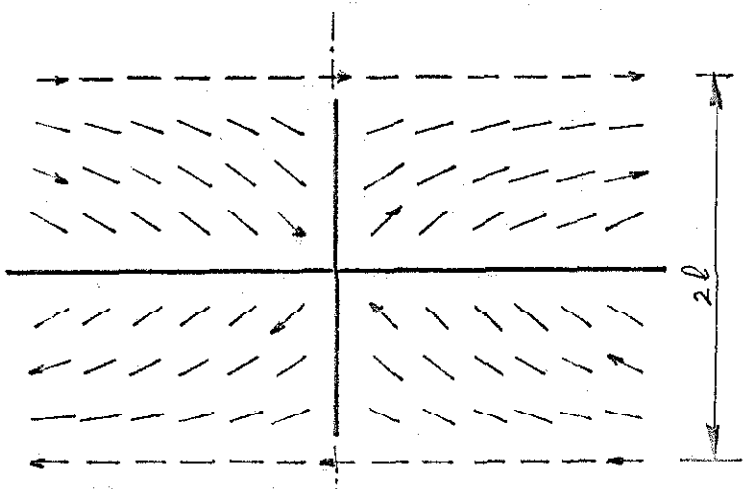

Fig. 4-12a "A" site separating two semi-infinite Néel walls

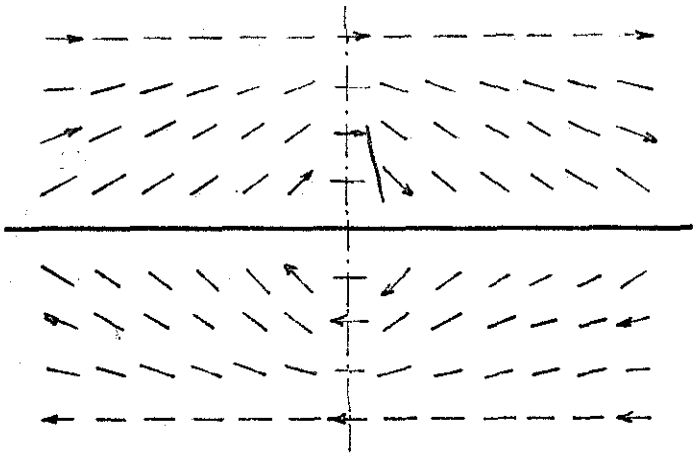

Fig. 4-12b "B" site separating two semiinfinite Néel walls

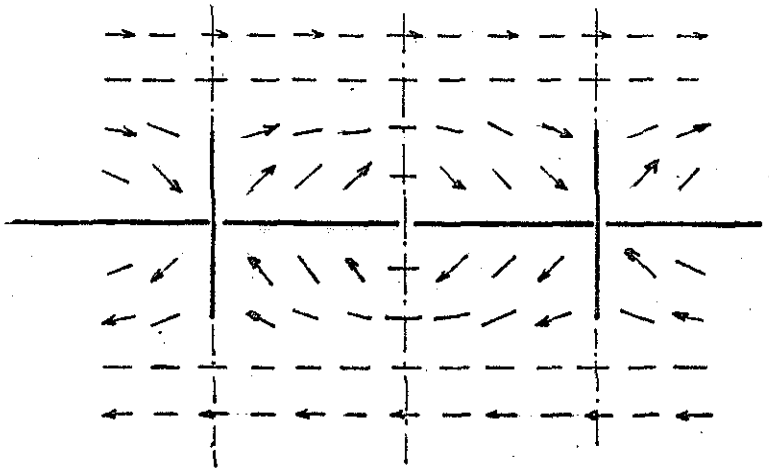

Fig. 4-12c Succession of interacting crosswalls

$$T_{ex} + T_a + T_m = 0$$

or $$2A\left[\frac{\partial^2\theta}{\partial x^2} + \frac{\partial^2\theta}{\partial y^2} + \frac{\partial^2\theta}{\partial x \partial y}\left(\frac{\partial\theta}{\partial y}\cdot\frac{\partial x}{\partial\theta} + \frac{\partial\theta}{\partial x}\cdot\frac{\partial y}{\partial\theta}\right)\right]$$

$$-K \sin 2\theta + \mu_o \vec{M} \times \vec{H}_i = 0 \qquad (4.2\text{-}1)$$

The boundary conditions would be:

$$\theta(x, -\infty) = \pi \; ; \; \theta(x, +\infty) = 0$$

$$\theta(x_+, o) = \pm \pi/2 : \theta(x_-, o) = \mp \pi/2$$

The point (0, 0) introduces a difficulty: there the magnetization must obviously point out of the plane. Rather than bringing a third dimension into the problem, a small circle of radius r could "isolate" mathematically this singular point at a "B" site, and the boundary condition would be that $\vec{M}$ be tangent to that circle . At an "A" site, the circle would be replaced by a diamond-shaped boundary (Fig. 4-13). The field $H_i(x,y)$ could be expressed by an integral such as (from eq. 2.3-4):

$$H_i(x,y) = \int\int \frac{\rho(x',y')\, dx'dy'}{4\pi[(x-x')^2 + (y-y')^2]}$$

with $$\rho(x,y) = -\frac{\partial M_x}{\partial x} - \frac{\partial M_y}{\partial y}$$

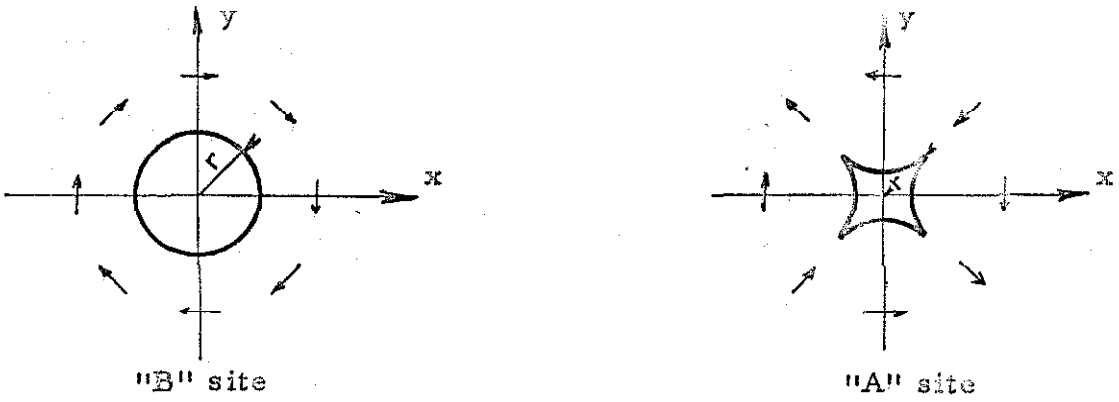

Fig. 4-13 Boundary conditions proposed for the singular points on the x axis at "A" and "B" sites

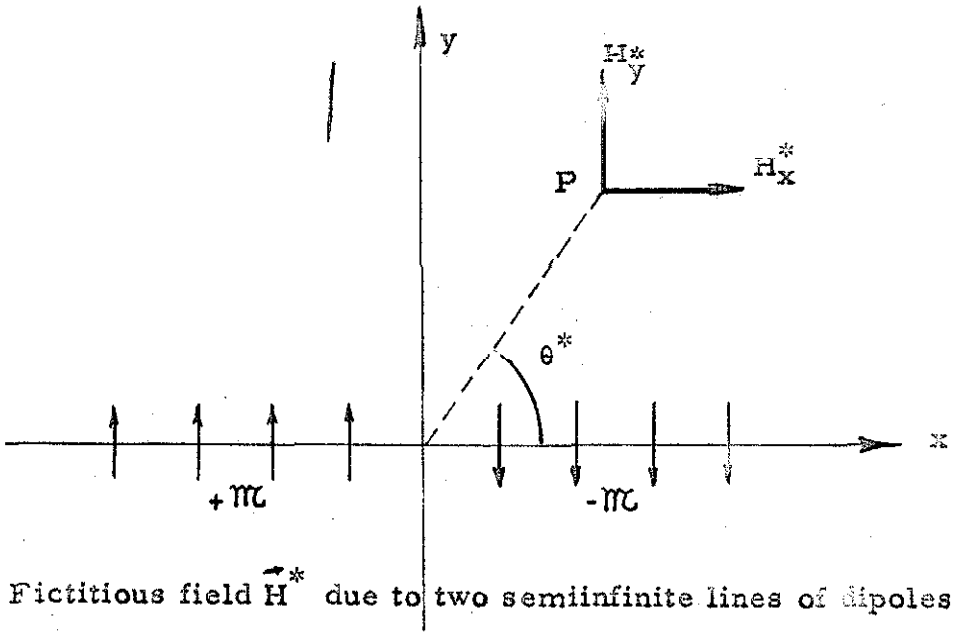

Fig. 4- 14 Fictitious field $\vec{H}^*$ due to two semiinfinite lines of dipoles

Such calculations would be complex and lengthy. The range of ordinates of y to be taken into account would be of the same order as that used in the Néel wall problem. For large x, the solution would tend towards the unidimensional one obtained in Chapter 3, which could therefore be used as a boundary condition permitting one to limit the extent of the x axis.

4.2.3 Magnetostatic Origin of "A" and "B" Sites

In this section it will be shown qualitatively how "A" and "B" sites originate and what energy variations they produce. The internal field in an infinite Néel wall has been determined accurately; it is produced by magnetic poles not only concentrated at the center of the wall, but also spread out in the slow rotation regions (Section 3.2). When two semi-infinite walls of opposite polarities are juxtaposed, the field at large x is not modified, but for small x, a component H_x appears. The difficulty in calculating $\vec{H}_i$ in that region is that the pole distribution $\rho(x,y)$ is not known. In order to nevertheless obtain an approximate evaluation of the field and magnetization configurations, a fictitious field $\vec{H}^*$ will be considered which is created by two lines of dipoles of strength $\pm$ $\mathfrak{M}$ centered upon the x axis, as indicated on Figure 4-14. It is calculated as follows.

The field due to a unit dipole, situated at the origin and directed along the y axis, is given by the following formulas in polar coordinates (from 2.3-5)

$$V = -\frac{\partial}{\partial y}\left(\frac{1}{4\pi r}\right) = \frac{\sin\theta}{4\pi r^2}$$

and $$H_r = -\frac{\partial V}{\partial r} = \frac{2\sin\theta}{4\pi r^3}, \quad H_\theta = -\frac{\partial V}{r\partial\theta} = -\frac{\cos\theta}{4\pi r^3}$$

Thus:

$$H_x = H_r\cos\theta - H_\theta\sin\theta = \frac{3\sin\theta\cos\theta}{4\pi r^3}$$

$$H_y = H_r\sin\theta + H_\theta\cos\theta = \frac{2 - 3\cos^2\theta}{4\pi r^3}$$

In the configuration of Figure 4-15a, the field at P is:

$$H_y = -\frac{m}{2\pi}\int_0^x \frac{2 - 3\cos^2\theta}{r^3}\,dx =$$

$$= -\frac{m}{2\pi}\int_0^x \left(\frac{2}{r^3} - \frac{3x^2}{r^5}\right)dx$$

$$= -\frac{m}{2\pi y^2}\cos\theta^*\left(1 + \sin^2\theta^*\right)$$

In the configuration of Figure 4-15b, the field at P is:

$$H_x = \frac{m}{2\pi}\int_{-\infty}^x \frac{3\sin\theta\cos\theta}{r^3}\,dx = \frac{}{2\pi}\int_{-\infty}^x \frac{3xy}{r^5}\,dx$$

$$= \frac{m}{2\pi y^2}\sin^3\theta^* \qquad (4.2\text{-}2)$$

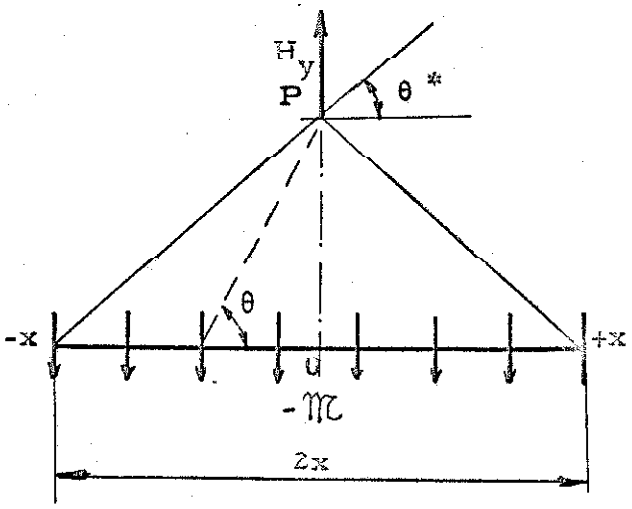

Fig. 4-15a Field at P due to the dipole distribution $\mp \mathfrak{M}$ in the intervals -x, 0 and 0, +x

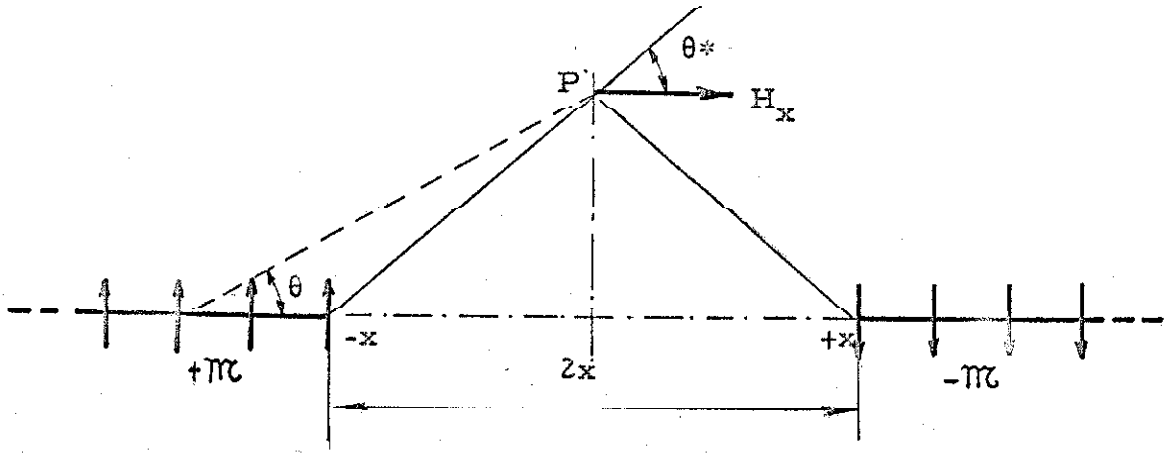

Fig. 4-15b

Field at P due to the dipole distribution $\pm \mathfrak{M}$ in the intervals $-\infty$, -x and x, $+\infty$

In Figure 4-14, at P, the y and x components of the field $\vec{H}^*$ are those of Figure 4-15a and b, respectively. Thus, the field distribution due to the juxtaposition of the two semi-infinite lines of dipoles is given by:

$$H^*_x = \mp \frac{\mathfrak{M}}{2\pi y^2} \sin^3\theta$$

$$H^*_y = \mp \frac{\mathfrak{M}}{2\pi y^2} \cos\theta\,(1 + \sin^2\theta)$$

The upper sign is valid for a "B" site and the lower one for an "A" site (see Fig. 4-11). The field lines appear in Figure 4-16. In particular, along the y axis, $H_y = 0$, and the field is parallel to the easy direction of the material.

When the magnetization distribution, valid for a Néel wall, is superimposed onto Figure 4-16, the two cases that lead to sites "A" and "B" are clearly distinguishable. Either the orientation of the domains, separated by the wall, coincides with the direction of the field along the y axis or it is opposed to it.

In the first case, the magnetostatic energy $-\frac{\mu_o}{2}\,\vec{M}\cdot\vec{H}_i$ is negative everywhere except evidently in the central portions of the Néel walls. Under the influence of the field $\vec{H}^*$, some rearrangement will take place in the $\vec{M}$ distribution, so that at every point an equilibrium is reached between the anisotropy and the magnetostatic torque. Just as in the case of the unidimensional Néel wall, the

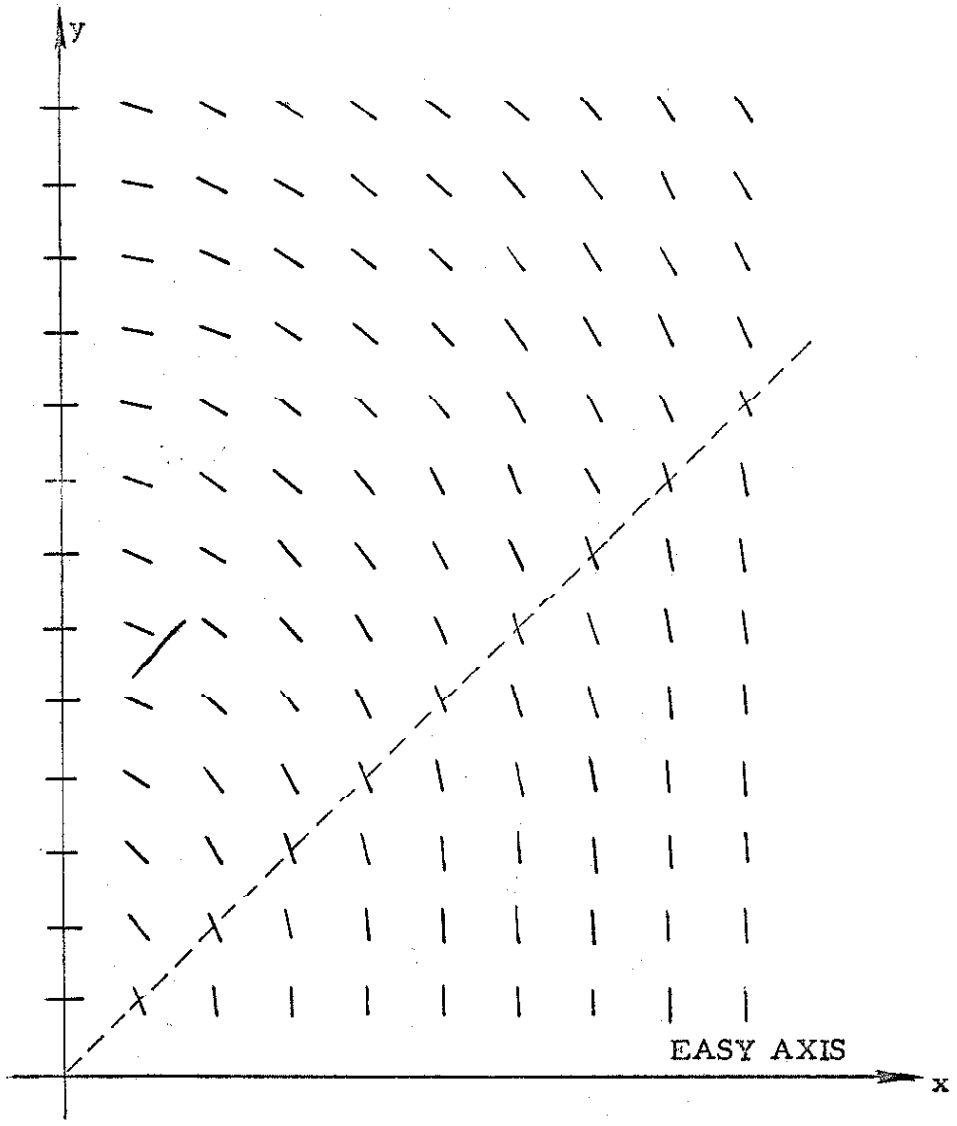

Fig. 4-16
Direction of the fictitious field $\vec{H}^*(x, y)$

exchange torque is neligible as a first approximation. In Section 2.4, the diagram of Figure 2-4 shows the direction of the $\vec{M}$ vector for any field applied. Unlike the case of Chapter 3, where $\vec{H}_i$ was parallel to the hard axis and therefore systematically less than H_k, $\vec{H}_i$ can now reach high values, and $\vec{M}$ will simply tend to point in the same direction. It is therefore possible to obtain a sizable reduction of energy by replacing an infinite Néel wall by two semi-infinite ones having the proper polarities. Indeed, the energy density is equal to (from eqs. 2.3-6 and 2.4-1)

$$\epsilon(\theta) = K \sin^2\theta - \frac{\mu_o}{2} H_i M \cos(\alpha-\theta) \qquad (4.2\text{-}4)$$

For any value of $|\alpha|$ smaller than 90°, the energy ϵ is negative, and this can be seen easily in Figure 4-17: the angle θ being constant, if $|\alpha| = 90°$, then $H_i = H_k \sin\theta$, and $\epsilon = 0$ (see Section 3.4), but for any smaller value of $|\alpha|$, H_i increases as well as $\cos(\alpha - \theta)$, which tends towards unity. Therefore, from (4.2-4), it is clear that ϵ is negative whenever $-\pi/2 < \alpha < \pi/2$, which is the case everywhere at a "B" site, except, of course, in the very center of the wall, on the axis. The gain of energy ΔE_b (negative value) can thus be appreciable, since there is no theoretical limit a priori for the value of H_i. This study does not permit the evaluation of ΔE_b.

The second case where $\vec{M}$ and $\vec{H}^*$ are opposed along the y axis is evidently much more complex. Here it is found that the angle

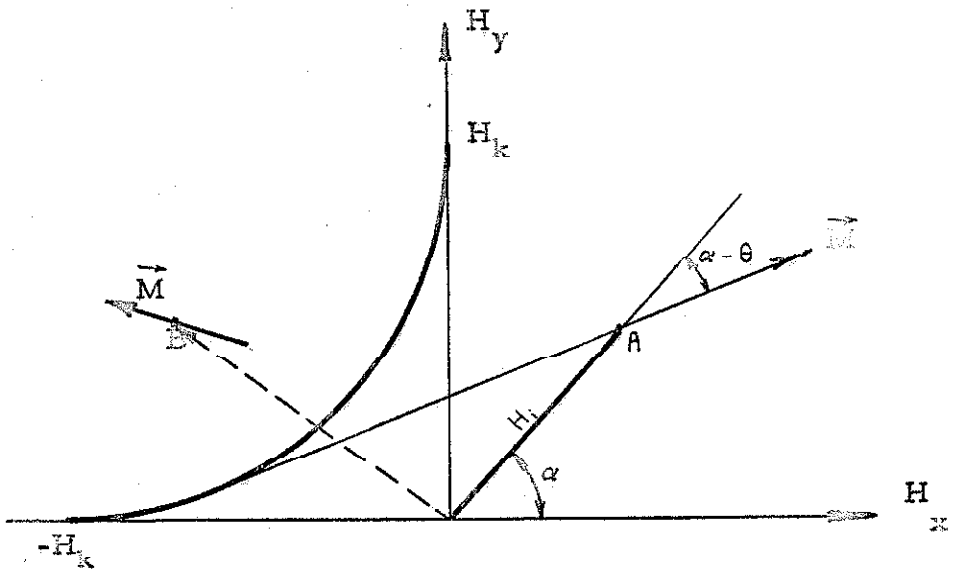

Fig. 4-17 Direction of $\vec{M}$ corresponding to a given $\vec{H}_i$ when the exchange torque is neglected

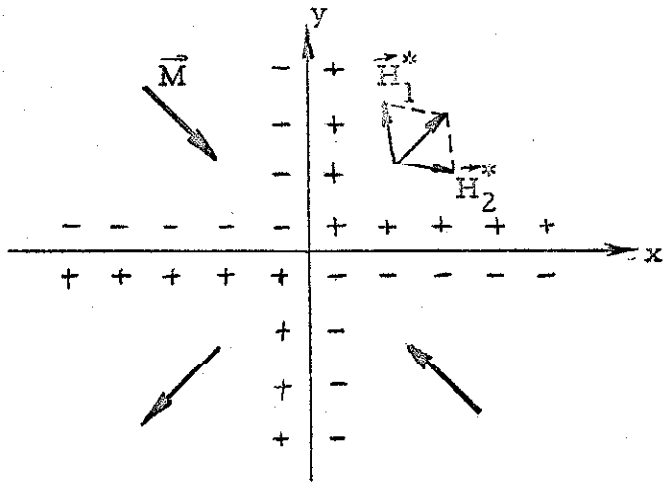

Fig. 4-18 Internal field at an "A" site determined by the poles along the crosswall and the main wall

$|\alpha|$ is larger than $\pi/2$. Using Figure 4-17 again, it can be seen that the energy would now be positive. Furthermore, and most important, the value of H_i is limited by the critical curve $(H_x/H_k)^{2/3} + (H_y/H_k)^{2/3} = 1$ (eq. 2.4-6). For larger values of H_i, no equilibrium between the anisotropy and magnetostatic torques is possible unless the magnetization switches to the stable direction (point B on Fig. 4-17), but the latter is not compatible with the boundary condition. Thus, under the influence of the field $\vec{H}^*$ of two semi-infinite lines of dipoles, the configuration not only presents a high positive magnetostatic energy but is also unstable. But actually, along the y axis, a transverse wall is created. This cross-tie is of the Néel type, that is to say $\vec{M}$ rotates in the plane of the film; the total angle of rotation is less than 180° and decreases for increasing y. The internal field is very different from the configuration of Figure 4-16; it must now be thought of as the superimposition of $\vec{H}^*_1$ due to the main wall, and $\vec{H}^*_2$ due to the transverse wall (Fig. 4-18). For instance, at a point such as A situated on the diagonal, close to the center 0, the magnetization and the field now point almost in the same direction. The field $\vec{H}^*_2$ is difficult to evaluate, being created by two finite lines of dipoles of decreasing strength $\mathfrak{M}$ (y). The strength $\mathfrak{M}$ (y) will be such as to minimize the magnetostatic and anisotropy energies in the large area outside the central portions of the longitudinal and transverse walls.

It is likely that again the angle $|\alpha|$ between the field and the x axis is smaller than $\pi/2$ everywhere. This would insure that the energy in the slow rotation region is negative also, as in the case of a "B" site. The central portion of the transverse wall is, of course, a region of high positive energy density, but its area is limited. It does not seem possible to decide a priori whether, on the whole, an "A" site represents a gain or a loss of energy ΔE_a with respect to an infinite wall.

4.2.4 Length and Frequency of Repetition of Crosswalls

As to the length $2\ell_o$ of such a transverse wall, in other words, the length of the corresponding Bitter trace, it is determined by the fictitious field $H^*_1(o,y)$. When H^*_1 reaches the threshold value H_o at a distance ℓ_o from the x axis, the break in the magnetization direction becomes so small that the trace disappears. It is not possible to determine H_o, nor even to know when the colloid stops being sensitive to the change in direction of the $\vec{M}$ vector.

It has been shown that a "B" site is accompanied by a decrease ΔE_b in the total energy of the wall. The influence of the reversal of polarity at x = 0 is felt up to a certain distance along the x axis of the order of the width of the Néel wall. Therefore, several "B" sites will occur along the length of the wall, each one corresponding to an energy variation $-|\Delta E_b|$. Evidently, two sites "B" imply the presence of an "A" site separating them. Thus, for each pair of "A" and "B"

sites, the energy variation is $\Delta E_a + \Delta E_b$, a negative quantity above the thickness t_{cl} (see Fig. 3-4). The frequency with which cross-tie walls appear along the longitudinal wall is determined by minimizing the total energy. If n_a and n_b are the numbers of "A" and "B" sites per unit length of wall and E_n the energy per unit length in a pure Néel wall (calculated in Section 3.7), the energy E of the cross-tie wall will be

$$E = E_n - n \left| \Delta E_a + \Delta E_b \right| = E_n - n \left| \Delta E \right| \qquad (4.2\text{-}5)$$

where $n = n_a = n_b$ and $\Delta E = \Delta E_a + \Delta E_b$.

Actually, when n becomes large, neighboring sites "A" and "B" start interacting, which reduces the energy balance $|\Delta E|$. This quantity $|\Delta E|$ is a function of n as represented in Figures 4-19a and 4-19b. The minimum of energy corresponds to the value n_o although, in practice, the number of cross walls will be less because local energy minima exist for smaller values of n due to imperfections in the film along the wall. This fact can be demonstrated by applying a small ac field perpendicular to the cross-tie wall, that is, along the hard direction. By "shaking" the wall, an increase in density of transverse walls is observed.

The length $2\ell_o$ of a transverse wall produced by two semi-infinite Néel walls is directly connected to the width $2a$ of an infinite Néel wall, since the fictitious fields $\vec{H}^*$ along the y axis for an infinite or two semi-infinite Néel walls are equal in amplitude, that is to say:

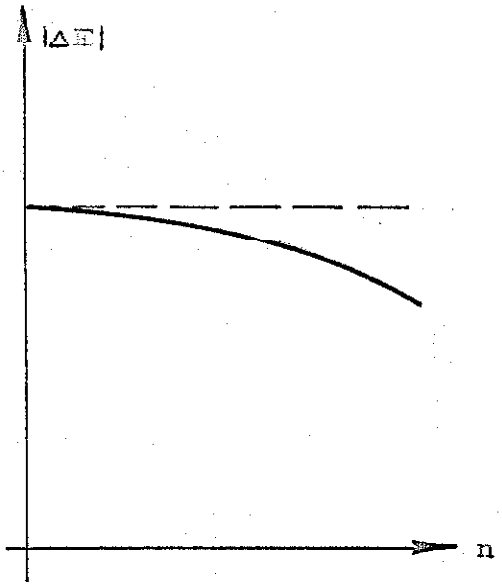

Fig. 4-19a
Variation of energy per crosswall as a function of their density n

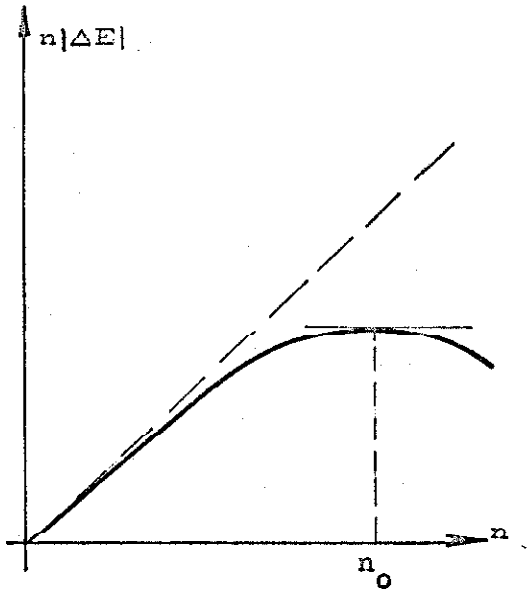

Fig. 4-19b
Variation of energy per unit length as a function of n

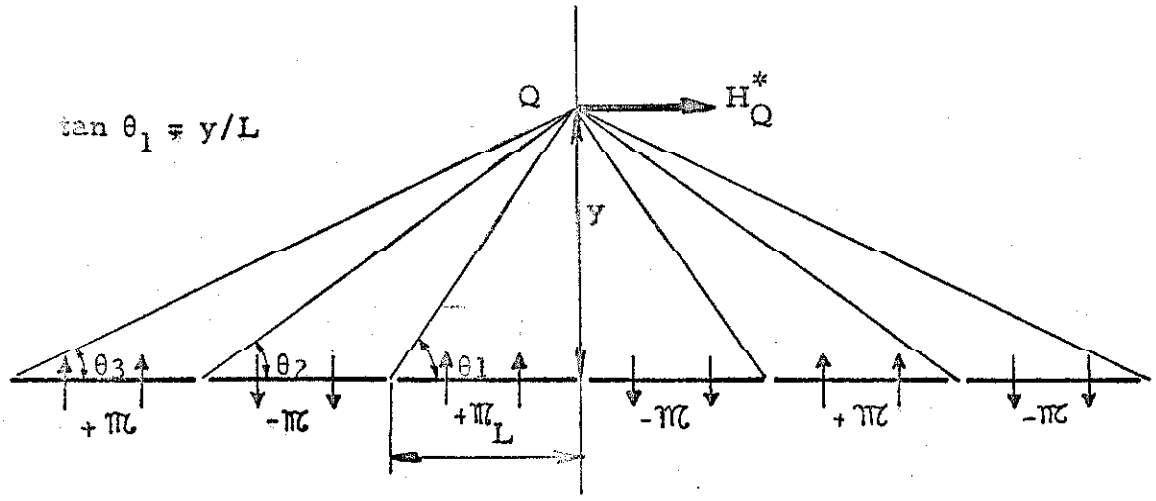

Fig. 4-20 Fictitious field at Q due to a succession of Néel wall segments of alternating polarities

$$H^*(o,y) = \frac{\pi\zeta}{2\pi y^2} = H^*(\infty,y)$$

Actually, the reduced field $h^* = H^*/H_k$ is the determining factor. It follows immediately that an increase in H_k results in a decrease in h^*, and therefore in ℓ. This phenomenon has been observed by Middelhoek (11), who, by bending a magnetostrictive film, artificially increased the anisotropy field. He found that ℓ is almost inversely proportional to H_k which, as a first approximation, follows from equations (3.6-4) and (3.6-5).

Cross-tie walls appear along the main wall with such a frequency that their interaction not only provokes a decrease in the energy variation $|\Delta E|$ (Fig. 4-19a) but also a decrease in their length 2ℓ. This variation of 2ℓ with $2L = 1/n$ can be expressed semiquantitatively as follows. Considering Figure 4-20, where the succession of dipole lines represents the main longitudinal wall, excluding the cross-ties, the field at a point such as Q is equal to (from 4.2-2):

$$H^*_Q = \frac{\pi\zeta}{2\pi y^2}\left[(1-\sin^3\theta_1)-(\sin^3\theta^*_1-\sin^3\theta_2)+(\sin^3\theta_2-\sin^3\theta_3)\ldots\right]$$

with $\sin\theta_n = y/(y^2+n^2L^2)^{\frac{1}{2}}$

Thus $$H^*_Q = \frac{\pi\zeta}{2\pi y^2} \cdot f(y/L) \qquad (4.2\text{-}6)$$

The function $f(y/L)$ is shown in Figure 4-21. If L is infinite, the length of a cross-tie is $2\ell_o$, determined by the threshold field $H_o = \mathcal{M} / 2\pi\ell_o^2$ introduced earlier. When L decreases (its optimum value equals $1/n_0$ as in Figure 4-19b), this fictitious field is modified according to equation (4.2-6). It is logical to assume that the length 2ℓ is determined by the same critical value H_o below which no trace is apparent on the Bitter pattern. Thus the value of ℓ should be related to L by an equation such as follows (Fig. 4-22):

$$\frac{\mathcal{M}}{\pi\ell_o^2} = H_o = \frac{\mathcal{M}}{2\pi\ell^2} \cdot f(\ell/L)$$

$$\ell = \ell_o \sqrt{f(\ell/L)}$$

In order to obtain meaningful quantitative results, the rigorous equation (4.2-1) should be solved along the lines of Chapter 3, but in two dimensions. The present limited study explains clearly, it is hoped, the various characteristics of cross-tie walls.

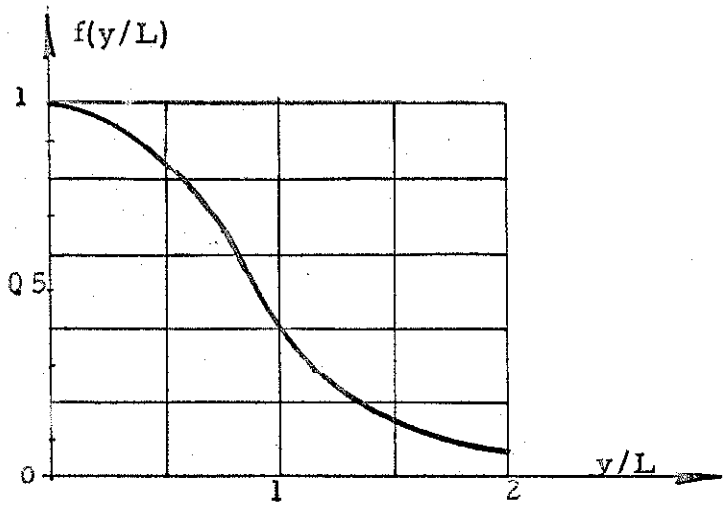

Fig. 4-21 Function f(y/L) (Equation 4.2-6)

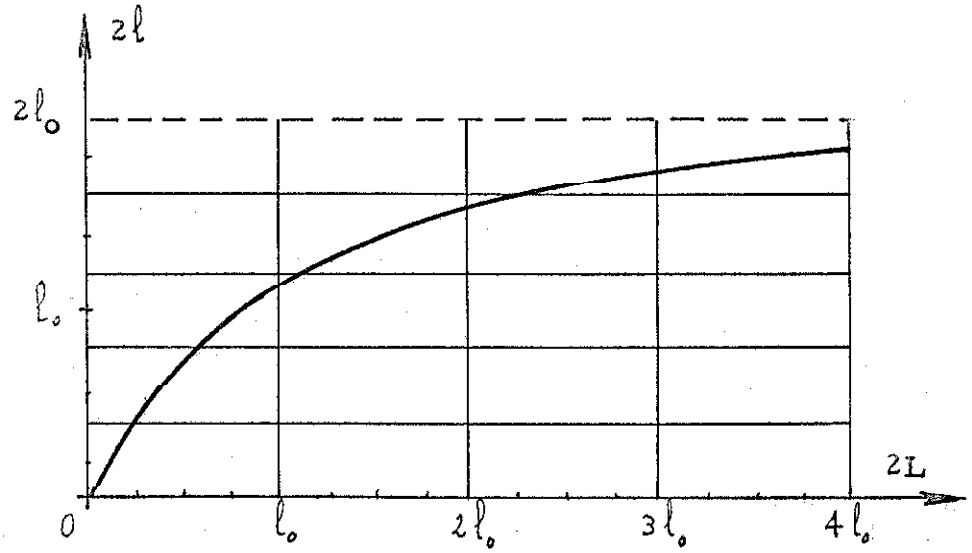

Fig. 4-22 Variation of the length of crosswalls with the distance separating them (see Fig. 4-8)

5. INTERNAL FIELDS AND REVERSAL OF MAGNETIZATION

5.1 Internal Field in Thin Magnetic Films

The nature of the magnetic flux reversal in a film has been found to depend upon the value of the applied field (6). Actually, the switching phenomenon is sensitive to the total effective field, which varies in magnitude and direction over the plane (x, y) of the layer. This field $\vec{H}_{eff}$ is the sum of the external field $\vec{H}_{ex}$ and $\vec{H}_i(x,y)$, the internal field due to the magnetic poles appearing principally at the film edges or, more generally, wherever div $\vec{M}$ is not zero (eq. 2.1-1). A detailed understanding of flux reversal must involve a correct knowledge of the internal field.

5.1.1 Field in the Interior of the Film

Although the existence of the internal field originating in the poles at the edges has always been recognized, it is usually assumed to be negligible except in the thicker films. In such films, for instance, the hysteresis loop in the easy direction (presumed square for a thinner sample) will appear distorted, as in Figure 5-1. If the shape of the sample is approximated by an ellipsoid (30) or an elliptical cylinder (11), in the cases of circular and rectangular

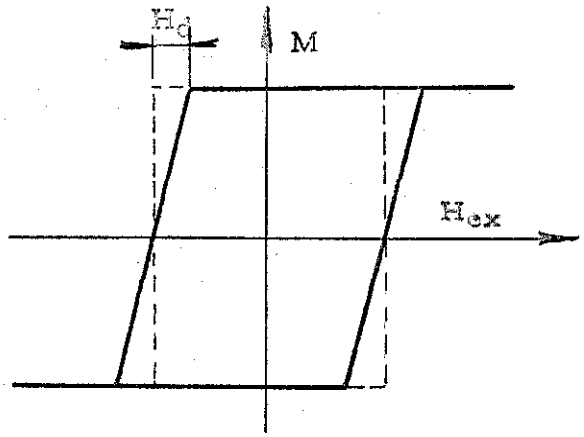

Fig. 5-1

Effect of average demagnetizing field on hysteresis loop along easy direction

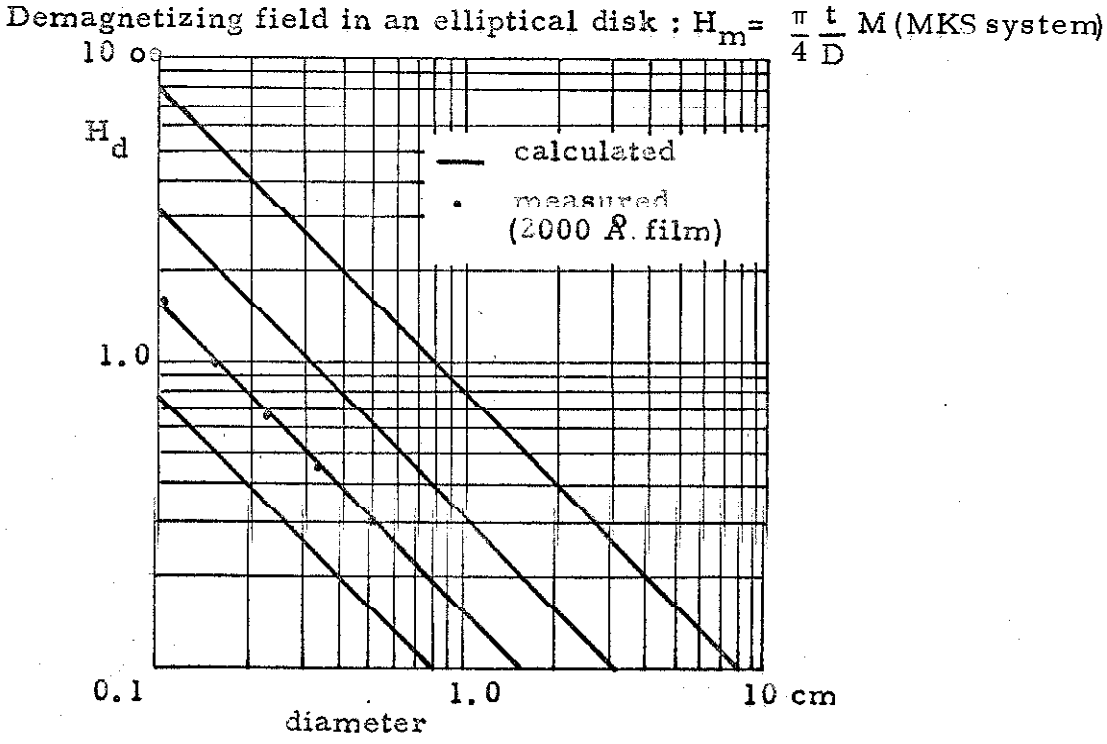

Fig. 5-2

Average demagnetizing field calculated and observed (reproduced from reference 30)

films, respectively, and if the state of magnetization is represented at every moment during a cycle through a hysteresis loop by an average vector $\vec{M}$ of constant direction parallel to the easy axis but varying smoothly from +M to -M, then a linear distortion of the loop can readily be calculated. The effect of this linear distortion can be seen in Figure 5-1. The computed and measured values of H_d are in reasonable agreement, as can be seen in Figure 5-2. However, such an analysis does not predict any fundamental modification of the M versus H curve, and the apparent distortion is due to the fact that H_{ex} rather than H_{eff} is represented in the abscissa.

Since an ellipsoid is the only case leading to a uniform demagnetizing field, and since films, in fact, do not have such a simple geometry, it is interesting to study the variations of the field $\vec{H}_i$ in the plane of the layer when the film is uniformly magnetized, this state being the starting point of the flux reversal. The magnetization $\vec{M}$ is assumed everywhere parallel to the same direction, which is actually the case when a saturating field is applied. The film is considered of uniform thickness t, and the presence of imperfections such as holes is ignored. Poles will therefore appear at the edges only and, viewed from some distance, their distribution is equivalent to lines of pole density λ. Figure 5-3 represents different shapes for which the field H_m at the center of the film can be calculated. (The formulas are analogous to those of electrostatics as mentioned in

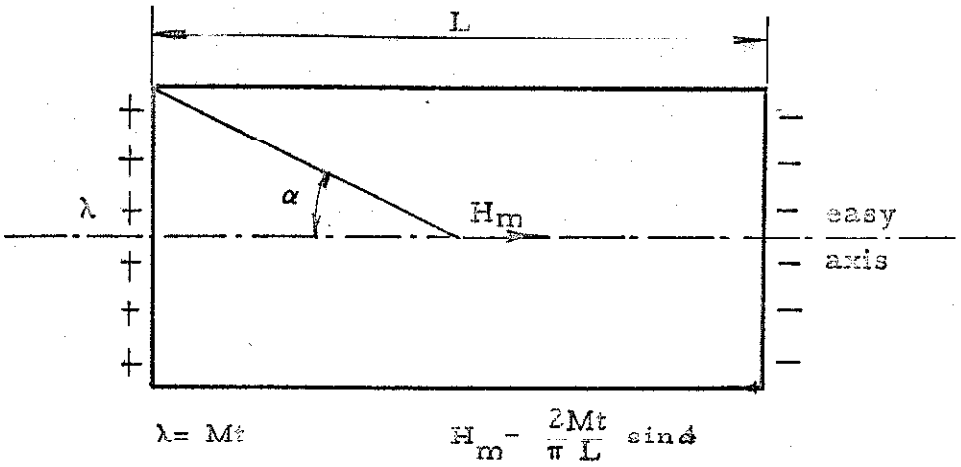

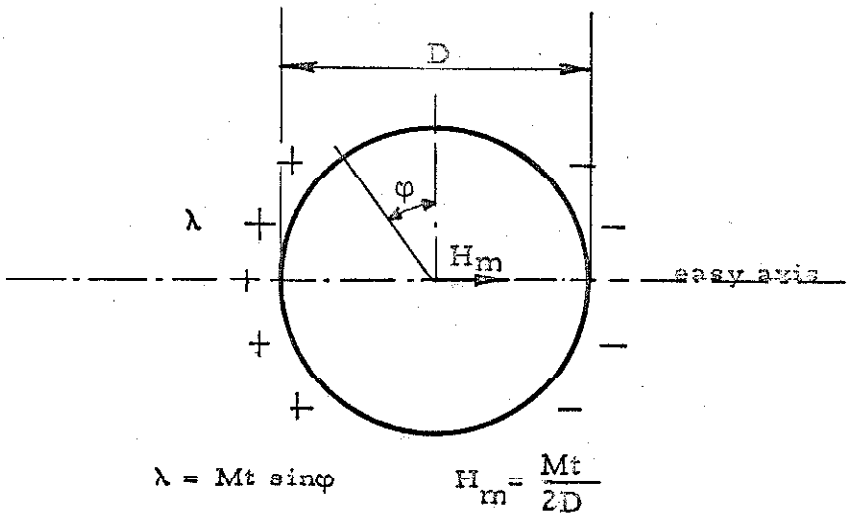

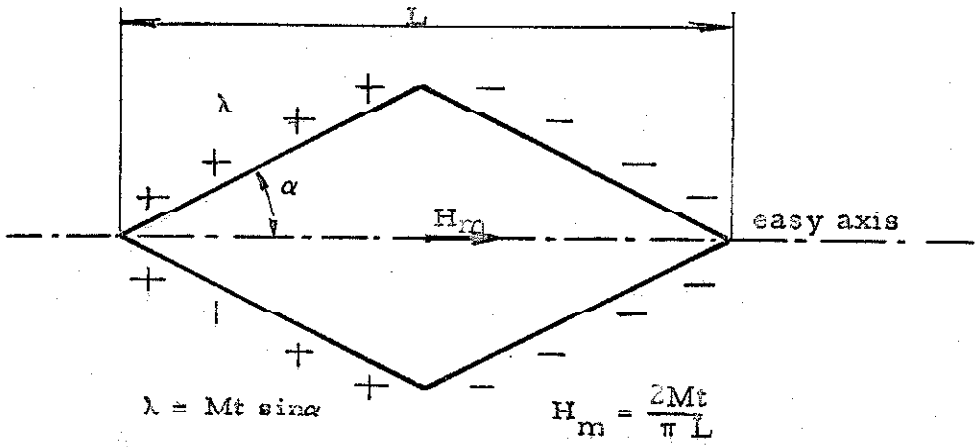

Fig. 5-3

Internal field at center for different shapes of films

Section 2.3). For example, in a circular film made of Permalloy 80-20 with a 3000-Å thickness and a 5-mm diameter, the demagnetizing field at the center would be $H_m = 0.3$ oe.

However, H_i increases away from the center along the easy direction. Figure 5-4 shows the relative values of the demagnetizing field along the symmetry axis of a square film. Except close to the edges (Section 5.1.2), this field is given by

$$H_i = \frac{Mt}{2\pi} \left(\frac{\sin \varphi_1}{x} + \frac{\sin \varphi_2}{L - x} \right)$$

and, at the center

$$H_m = \frac{(2)^{\frac{1}{2}}}{\pi} \cdot \frac{Mt}{L}$$

5.1.2 Field at the Edge of the Film

In the immediate neighborhood of the edge, which is assumed perpendicular to the easy axis, the one-dimensional line charge is no longer an acceptable approximation, since it would predict an infinite value at the edge. In a geometrically perfect layer, i.e., a layer whose edge structure is an abrupt step (Fig. 5-5), H_i would reach the maximum value $M/2$ at $x = 0$ (from eq. 2.3-3). In reality, the profile of the film around $x = 0$ is by no means abrupt, and the thickness $\delta(x)$ varies continuously from t to 0 over a distance $2D$, which is considerably larger than t (Fig. 5-6). A quantitative

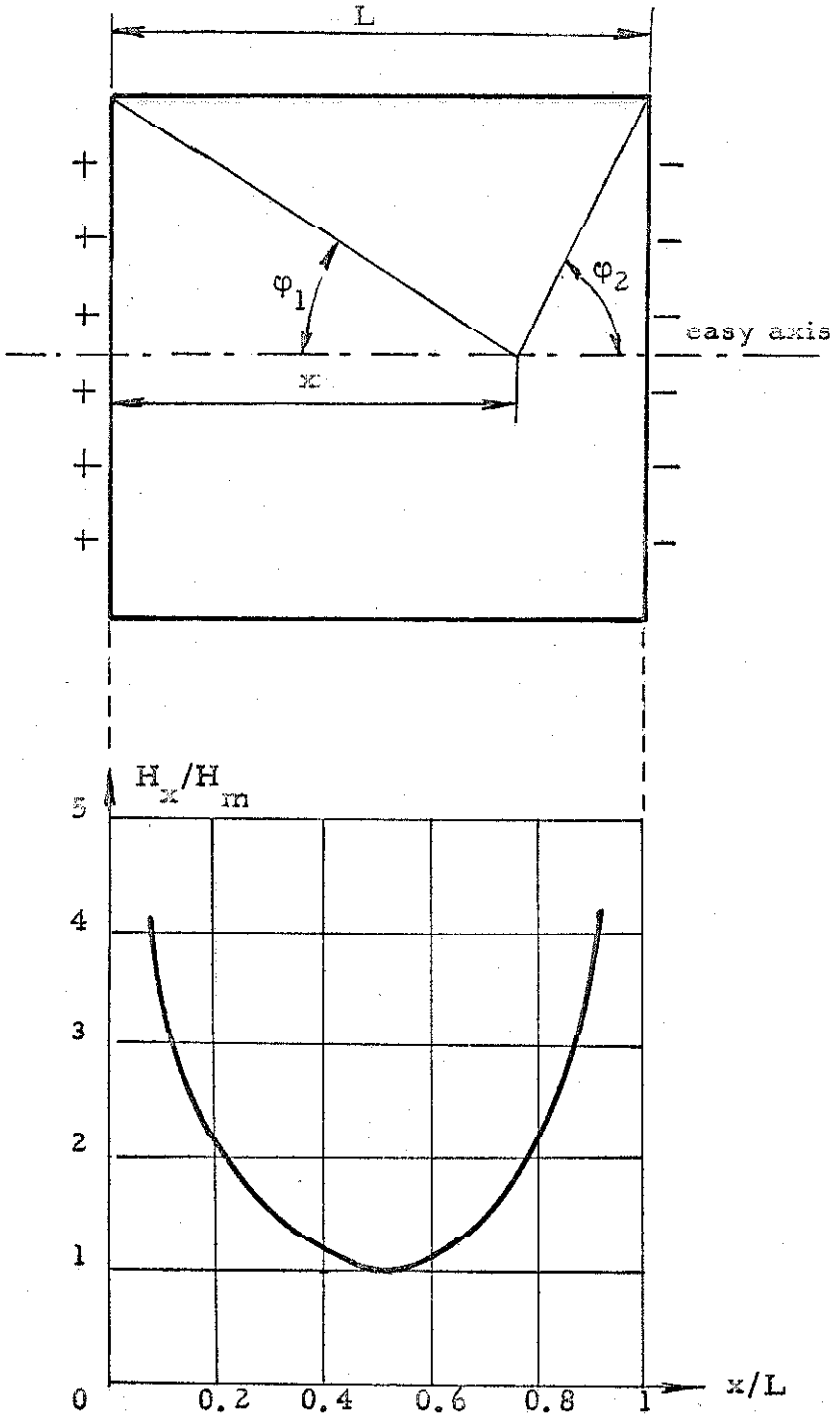

Fig. 5-4

Internal field along the symmetry axis of a square film

analysis of the function $H_i(x)$ is of special interest at the edge, since it is there that the internal field is the highest and that nucleation of reverse domains is therefore likely to occur first. Magnetic poles appear at the surface of the film over the distance 2D. Their surface density is $\sigma(x) = Md\delta/dx$. A mathematical expression $\sigma(x)$, which is reasonably close to reality and permits an analytical treatment of the problem, has been chosen in the interval (-D, +D) to be:

$$\sigma(x) = A\left(1 - \frac{x^2}{D^2}\right) \qquad (5.1\text{-}1)$$

where

$$A = \frac{3}{4}\,\frac{Mt}{D}$$

so that

$$\int_{-D}^{+D} \sigma(x)\,dx = Mt\ .$$

The corresponding expression for the thickness is:

$$\delta(x) = t\left(\tfrac{1}{2} + \tfrac{3}{4}\,\frac{x}{D} - \tfrac{1}{4}\,\frac{x^3}{D^3}\right) \qquad (5.1\text{-}2)$$

In the case of a purposely tapered edge, 2D is several orders of magnitude larger than t, and the fact that these charges are on a sloped surface can be neglected. The internal field $H_i(x)$ in the plane of the film is, from equation (2.3-1):

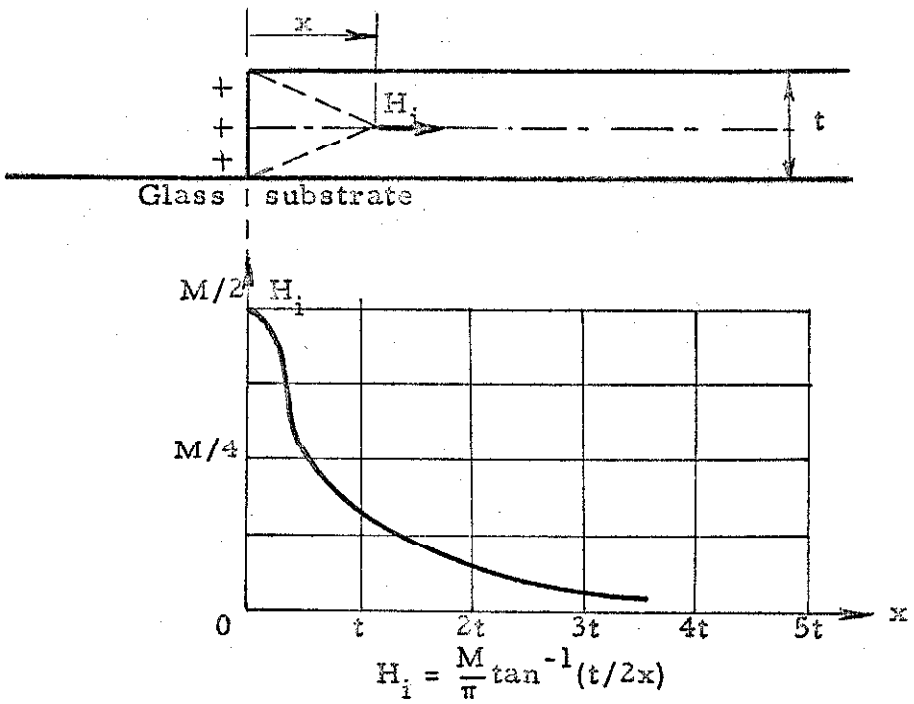

Fig. 5-5

Internal field at an abrupt edge

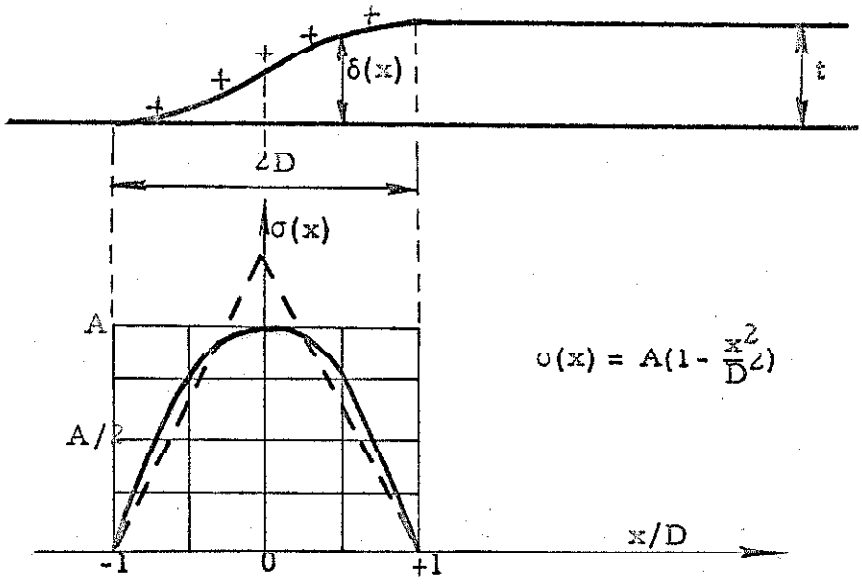

Fig. 5-6

Tapered profile and pole distribution

$$H_i(x) = \int_{-D}^{+D} \frac{\sigma d\xi}{2\pi(x-\xi)}$$

or, by symmetry,

$$H_i(x) = \int_o^D \frac{x\sigma\, d\xi}{\pi(x^2-\xi^2)} = \frac{x}{\pi} \cdot \frac{3\,Mt}{4\,D} \int_o^D \frac{(1 - \xi^2/D^2)d\xi}{x^2 - \xi^2}$$

$$= \frac{3x\,Mt}{4\pi D} \left[\frac{1}{2x} \ell n \left| \frac{x+\xi}{x-\xi} \right| + \frac{1}{D^2} \left(\xi - \frac{x}{2} \ell n \left| \frac{x+\xi}{x-\xi} \right| \right) \right]_o^D$$

$$- \frac{Mt}{2\pi} \cdot \frac{3}{2D} \left[\frac{x}{D} + \frac{1}{2} \left(1 - \frac{x^2}{D^2}\right) \ell n \left| \frac{x+D}{x-D} \right| \right] \qquad (5.1\text{-}3)$$

At large x, of course, this expression reduces to

$$H_i = \frac{Mt}{2\pi x}$$

Figure 5-7 represents the configuration of this internal field, which reaches its maximum positive value $H_{i\,max}$ at $x \simeq 0.75D$. For the shape assumed in this analysis, $H_{i\,max} = k(Mt/2\pi D)$, with $k \simeq 1.8$. The coefficient k will vary with the shape chosen for the tapered profile. If, for instance, $\sigma(x) = (Mt/D)(1 - |x|/D)$ in place of equation (5.1-1) (dashed line of Fig. 5-6), the new calculated value of k is 1.76 (at $x \simeq 0.68D$). This field $H_{i\,max}$ is proportional to t and inversely proportional to D. Table 5-I demonstrates that

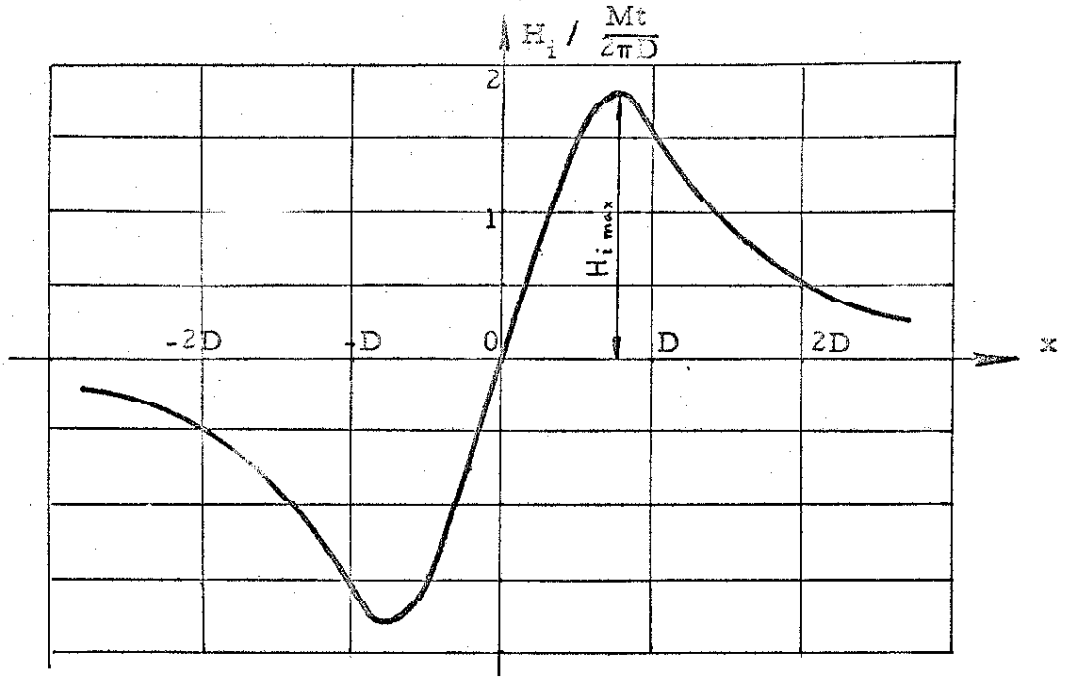

Fig. 5-7 Internal field at the edge (tapered profile)

Table 5-I

Maximum internal field $H_{i\,max}$ (in oersteds) at $x \approx 0.75D$

Thickness t	D= 0	D = 0.01mm	D= 0.1mm	D= 1mm
100 Å	5000	2.9	0.29	0.03
1000 Å	5000	29	2.9	0.29
2000 Å	5000	58	5.8	0.58
3000 Å	5000	145	14.5	1.45

1 Oe = 79.58 amp-turns/m

80-20 Permalloy : $M = 8 \cdot 10^5$ amp-turns/m

it is possible to obtain very low values for $H_{i\,max}$ by giving a sufficient slope to the edge profile. Such a control on the demagnetizing field could be highly desirable. The magnetostatic energy associated with the internal field

$$E_i = -\frac{\mu_o}{2} \int_V \vec{H}_i \cdot \vec{M}\, dv$$

is similarly drastically reduced when the edges are tapered.

5.2 Formation, Growth and Propagation of Walls

5.2.1 General

Any static domain observed in a film under the influence of a given field corresponds to a minimum of energy. However, this energy value does not necessarily correspond to the lowest energy state of the film, but most often to a local minimum. Such is the situation, for instance, when a negative field, less than the coercive force, is applied along the easy axis of the film and the magnetization still points in the positive direction. Similarly, in the absence of an external field, the state of equilibrium will depend upon the previous field history and many states between a fully magnetized (1) and fully demagnetized (3) sample may be reached (Fig. 5-8).

The evaluation of the total energy stored in the film is feasible only for very simple domain and external field configurations. Therefore, in most instances, the shape of a hysteresis loop in the easy

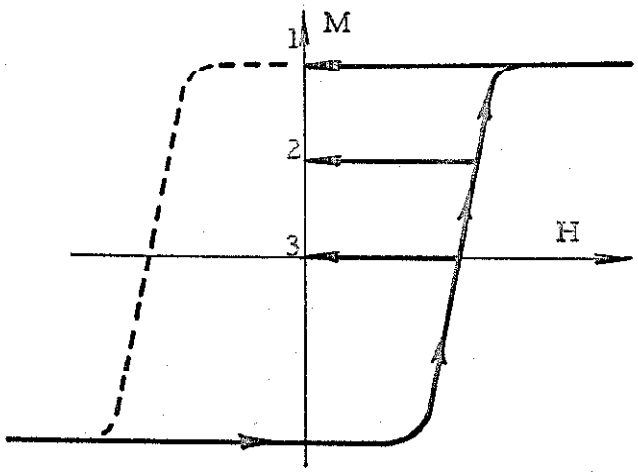

Fig. 5-8

Possible states of magnetization of a film in a zero field (from fully saturated to fully demagnetized)

direction cannot be predicted quantitatively, but it is possible to understand schematically all its features.

Any domain configuration other than uniform magnetization (single domain) implies the presence of domain walls with which energy is associated. A variation in stored energy corresponds to a variation in shape or position. Two phenomena can be distinguished:

1. The formation of a nucleus of reverse magnetization and its subsequent growth, where the wall length and configuration change.
2. The lateral propagation of a wall, where only its position is modified.

"Nucleation" occurring in a uniformly magnetized body is the phenomenon by which an elementary volume of material of reverse magnetization is created and grows under the influence of a field favoring its expansion. The details of the nucleation mechanism are not known yet. It may simply be assumed that whenever the effective field reaches a given value H_n, the nucleation field, a nucleus is created.

"Wall propagation" refers to the lateral translation of a wall, the shape of which is otherwise unaltered. As in the preceding case, it is first necessary to establish the graph of E_w, wall energy per unit length, as a function of the translation x. In an ideal film, E_w would be a constant ($E_w = E_{wo}$). However, small-scale imperfections

always occur in the geometrical and physical properties of the layer: thickness variations, polycrystalline structure, amplitude and directional dispersion of the anisotropy, etc. The actual function $E_w = E_{wo} + \Delta E_w$ will therefore oscillate probably with an average wavelength of the order of the crystallite dimension (a few hundred Angströms).

In a zero field, the wall will stabilize itself at a minimum energy location (1, 2, 3 on Fig. 5-9). When a field is applied favoring domain M_1, the variation of magnetostatic energy per unit length is:

$$dE = 2\mu_o MH\ t\ dx = -k\,H\ dx \qquad (5.2\text{-}1)$$

Again the position of the wall will be determined by the equation

$$\frac{dE}{dx} = \frac{d\Delta E_w}{dx} - k\,H = 0 \quad .$$

For small positive and negative fields, the wall will not move appreciably, but rather oscillate reversibly around position 1, for instance. However, as soon as H_{ex} equals $\frac{1}{k}\left(\frac{d\Delta E_w}{dx}\right)_{max}$ (Fig. 5-10), the wall will jump irreversibly from A to B with a loss of energy ultimately dissipated as heat:

$$E_A - E_B = E_{wA} - E_{wB} + kH\Delta x \quad .$$

The propagation field at location 1 is defined as follows:

$$H_w = \frac{1}{k}\left(\frac{d\Delta E_w}{dx}\right)_{max} \qquad (5.2\text{-}2)$$

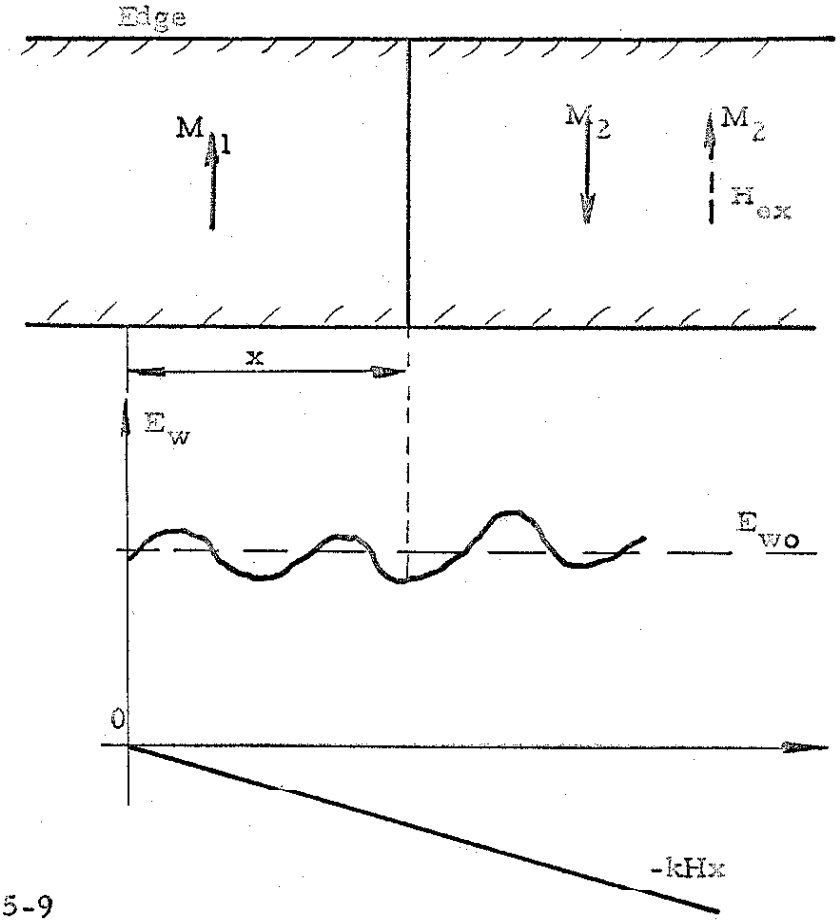

Fig. 5-9

Variation of wall energy with displacement

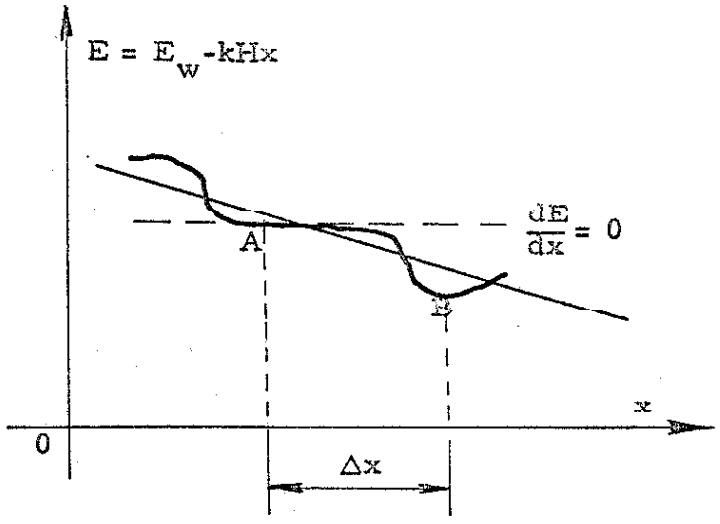

Fig. 5-10

Energy loss corresponding to a translation Δx of the wall under the influence of an external field

It varies throughout a given film and, in some very non-uniform films, "islands" of high propagation field are present which switch last, at larger fields.

It is important to recognize that, even when the field H is greater than H_w, it does not necessarily follow that switching will occur. Indeed the wall must first be created before propagation can take place at all. The creation of a wall implies the formation of a nucleus at some location in the film, which itself requires a minimum field H_n as previously stated.

5.2.2 Magnetic Flux Reversal by Wall Motion

Figure 5-11 represents the hysteresis curve along the easy axis of a rectangular film, 2500 Å thick and 1 cm long, with normal edges (mask in contact with substrate during deposition). When magnetization reversal is observed by means of the Kerr optical effect, "peaks" of reverse magnetization appear at the edges while the external field H_{ex} is still negative (point "A" on the hysteresis loop). When the field reaches a zero value ("B"), these peaks have increased in length and, finally, at some positive field ("C"), characterizing the knee of the M-H loop, some of them join with others from the opposite edge. From there on, the film proceeds to switch largely by lateral wall motion. The coercive force H_c (at "D"), which should be equal to H_w (wall propagation), corresponds to a half

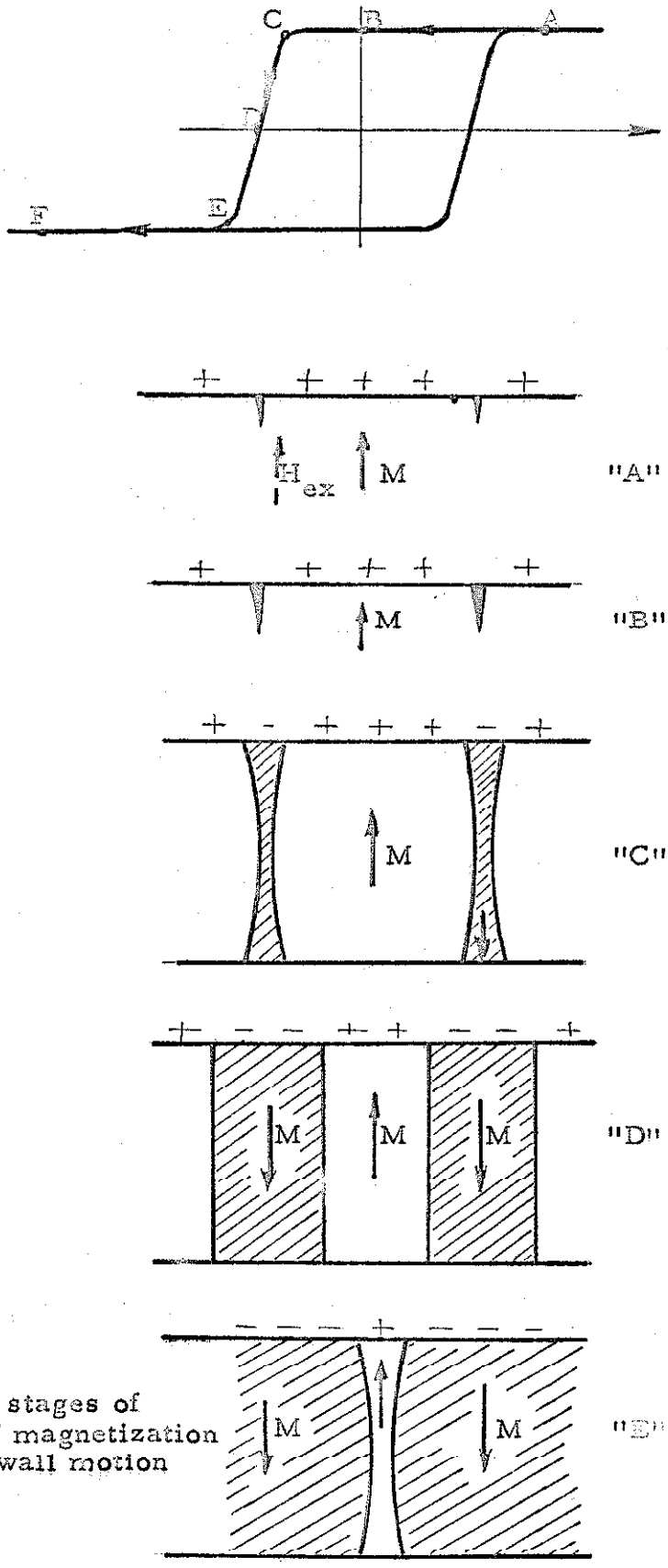

Fig. 5-11

Successive stages of reversal of magnetization by domain wall motion

switched film. At "E," areas remain where the magnetization is not reversed yet and the situation is very similar to that of Figure 5-11C. The hysteresis curve exhibits a slope between points "C" and "E," whose origin, as mentioned previously, is due to the average demagnetizing field inside the layer. Thus, the thinner the film, the squarer the M-H loop, at least if the wall propagation field H_w is uniform over the whole sample. With increasing positive field, the unswitched "wedges" diminish in size and, finally, at "F," become undetectable with the Kerr effect.

This sequence of events is easily understood qualitatively: close to the edges a sizable demagnetizing field H_i is superimposed on the external field. Nuclei of reverse magnetization appear at a point such as "A," where $|H_{ex} + H_i|$ equals H_n, the nucleation field (Section 5.2.1). At "B," the effective field in the neighborhood of the edges is positive rather than zero, so as to favor the growth of the nuclei. Between "E" and "F," the internal field is now negative and tends to maintain the presence of unswitched areas along the edges.

A semiquantitative analysis is given here which describes the variation of size of such a wedge as in cases "A," "B," and "E" under the influence of an external field. The resistance to propagation of the walls is taken into account. Simplifying hypotheses are made. One reverse domain only is considered, that is, the interaction between

neighboring domains is neglected. The shape of the wedge is supposed to remain similar to itself and it will therefore be uniquely determined by its length "ℓ." A nucleus is supposed to exist initially, and its creation is not examined, for it is a process which takes place at the very edge of the film. The dimension "ℓ" is taken to be much larger than 2D (see Section 5.1.2) and this study is independent of the profile of the edge. The configuration of Figure 5-12a is equivalent to that of 5-12b and c. The total energy is $E = E_m + E_i + E_w$, where E_m represents the magnetostatic energy associated with the external field H_{ex}, E_i the internal magnetostatic energy, and E_w the wall energy. The anisotropy and exchange energies are zero outside the walls themselves. Thus:

$$E_m = -\mu_o \int_V \vec{H}_{ex} \cdot \dot{M}\, dv$$

or, on the basis of Figures 5-12b and c, S being the area of the wedge,

$$E_m = -\mu_o \int_V H_{ex} M\, dv + 2\mu_o M H_{ex} S t$$

The internal magnetostatic energy can be written in the same way:

$$E_i = -\frac{\mu_o}{2} \int_V \vec{M}(x,y) \cdot \vec{H}_i\, dv = -\frac{\mu_o}{2} \int_V \vec{M} \cdot (\vec{H}_{i1} + \vec{H}_{i2})\, dv$$

$$= \frac{\mu_o}{2} \int_V M H_{i1}\, dv - \frac{\mu_o}{2} \int_S 2M H_{i1}\, dv - \frac{\mu_o}{2} \int_V \vec{M} \cdot \vec{H}_{i2}\, dv$$

$$= \frac{\mu_o}{2} \int_V M H_{i1}\, dv - \alpha M^2 t^2 \ell + \beta M^2 t^2 \ell$$

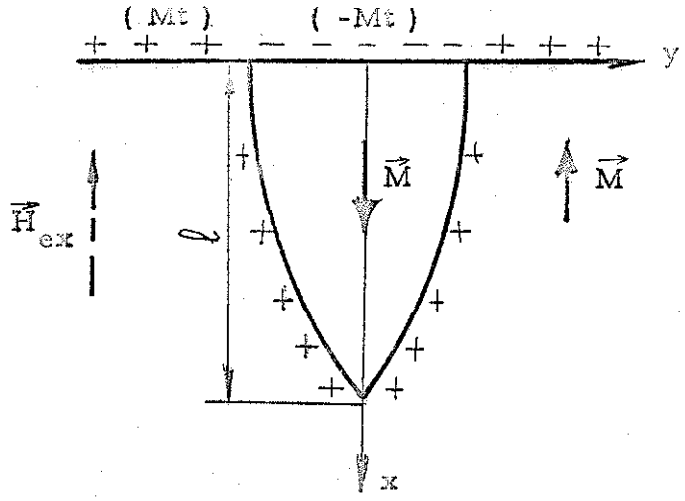

Fig. 5-12a

Wedge domain of reverse magnetization at the edge

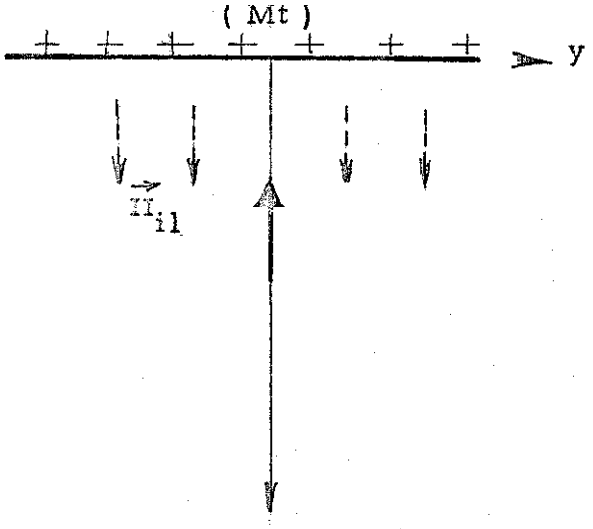

Fig. 5-12b

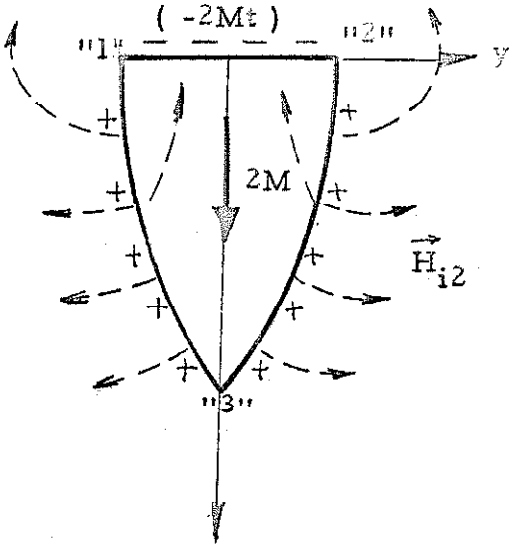

Fig. 5-12c

The first term is a constant for a given film, the other two are obtained as follows: The field $\vec{H}_{i2}$, for instance, due to the pole distribution of Figure 5-12c, can be written in general:

$$\vec{H}_i = \frac{Mt}{\ell} \cdot \vec{f}\left(\frac{x}{\ell}, \frac{y}{\ell}\right)$$

for a given shape of the reverse domain. Indeed, a field due to line charges is inversely proportional to distances. Therefore:

$$-\frac{\mu_o}{2}\int_V \vec{M}\cdot\vec{H}_{i2}\,dv = -\frac{\mu_o}{2}\,\frac{Mt^2\ell^2}{\ell}\int_V \vec{M}\cdot\vec{f}\left(\frac{x}{\ell},\frac{y}{\ell}\right)d\left(\frac{x}{\ell}\right)d\left(\frac{y}{\ell}\right)$$

$$= M^2t^2\ell\left[-\frac{\mu_o}{2}\int_V \frac{\vec{M}}{M}\cdot\vec{f}\,d\left(\frac{x}{\ell}\right)d\left(\frac{y}{\ell}\right)\right]$$

$$= \beta M^2t^2\ell \ .$$

As far as the wall energy is concerned, it is assumed to be composed of three terms. The first one, proportional to the perimeter of the wedge, is written $\ell\delta(t)$. A constant term E_{wc} accounts for the additional energy stored at the corners 1, 2, and 3 (Fig. 5-12c). Furthermore, a variable term ΔE_w must be added, although its average over space is zero. It represents the variation of energy giving rise to a non-zero propagation field H_w for the translation of the wall. Thus:

$$E_w = E_{wc} + \Delta E_w + \ell\delta(t)$$

By definition of the propagation field, the following relationship exists between H_w and ΔE_w (eq. 5.2-1 and 2):

$$\left| \frac{d(\Delta E_w)}{dS} \right|_{max} = 2\mu_o Mt H_w$$

where ΔE_w is expressed in terms of S, the surface area of the wedge. The total energy $E = E_m + E_i + E_w$ assumes a minimum for every value of the external field H_{ex}. The equilibrium is given by the equation: $\frac{\partial E}{\partial \ell} = 0$ or $\frac{\partial E}{\partial S} = 0$. Since the reverse domain remains similar to itself, it is equivalent to describe its size by its length or area: $S = A\ell^2$ where A is a constant depending on the exact shape of the wedge.

$$\frac{\partial E}{\partial \ell} \equiv 4A\mu_o Mt H_{ex} \ell - \alpha M^2 t^2 + \beta M^2 t^2 + \delta(t) + 2A\ell \frac{\partial(\Delta E_w)}{\partial S} = 0$$

This equation gives for continuously increasing (- sign) or decreasing (+ sign) fields H_{ex}:

$$4A\mu_o Mt\ell (H_{ex} \pm H_w) = M^2 t^2 (\alpha - \beta) - \delta(t)$$

Therefore,

$$\ell = \frac{M^2 t^2 (\alpha - \beta) - \delta(t)}{4A\mu_o Mt(H_{ex} \pm H_w)} = \frac{Bt^2 - \delta(t)}{Ct(H \pm H_w)} \qquad (5.2\text{-}3)$$

where α, β and A are geometrical factors depending upon the detailed shape of the domain.

Figure 5-13 represents the variations of ℓ with the external field. The propagation field H_w, i.e., the coercive force, is indicated on the abscissa axis. When H_{ex} decreases toward $-H_w$, the formula

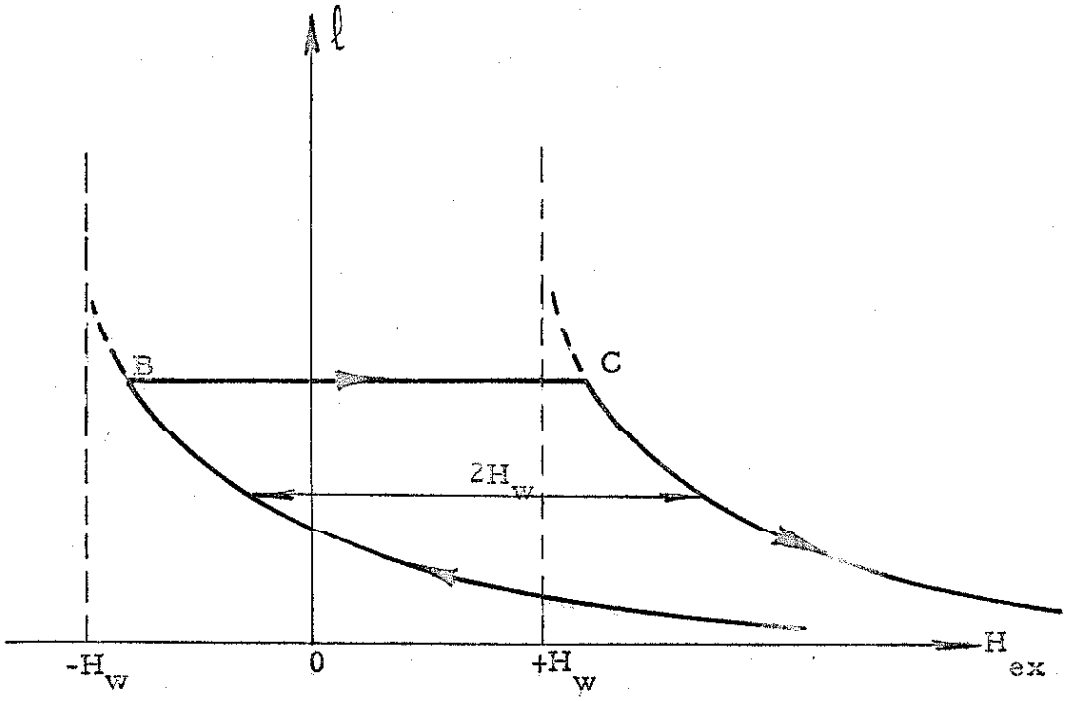

Fig. 5-13 Variation of length of edge domain with increasing and decreasing external field

indicates that ℓ tends to infinity; in fact, peaks from opposite edges grow toward each other and join to form longitudinal walls parallel to the easy axis. If the variation of H_{ex} is reversed, the peaks disappear, but with some hysteresis represented by the horizontal line BC. This too is predicted by the formula obtained.

It is observed experimentally that such reverse domains appear spontaneously only above a minimum film thickness. Equation (5.2-3) also predicts this, since the numerator of the expression given for ℓ becomes zero when $Bt^2 = \delta(t)$. Thus, above a critical thickness $t_c = \sqrt{\frac{\delta(t_c)}{B}}$, peaks of reverse magnetization will be present. A calculation of coefficients B and C, as well as the energy density $\delta(t)$, in the walls, would be rather meaningless because of the inaccuracy of the numerical results due to the simplified model considered and the necessarily approximate computations. The preceding semi-quantitative analysis explains, however, the observed growth and disappearance of these edge domains.

5.3 Hysteresis Curves of Films with Tapered Edges

5.3.1 Tapering of Edges

Inside the vacuum chamber where the deposition takes place, the Permalloy source is a slug 2 cm in diameter and placed 13 cm below the substrate. If the mask determining the shape of the film is not in contact with the glass, the edges of the sample will be tapered

over the region situated in the penumbra of the mask, as shown in Figure 5-14. For instance, if the spacing δ between substrate and mask is 1 cm, the width $2D = \delta\ell/L$ should be of the order of 1 mm. The profile of such an edge is easily observed with an interferometer. The shape of the interference lines is a replica of the edge itself. Figure 5-15 reproduces the interference pattern of a 2500 Å film. It is not possible to choose a mathematical expression that would describe such a profile rigorously. Because of reflections inside the vacuum jar, not all atoms reaching the glass follow a straight trajectory between slug and substrate; also, the slug is circular and the contribution to the evaporation of slices "A," "B," and "C" of different sizes will vary (Fig. 5-14). Thus, such factors as bouncing of atoms against the equipment inside the deposition chamber and the shape of the alloy source, account for the fact that the tapered edge presents rounded extremities rather than a constant slope. The function $\delta(x) = t(\frac{1}{2} + 3x/4d - x^3/4D^3)$ has been chosen in Section 5.1.2 to describe this profile (Fig. 5-6).

5.3.2 Hysteresis Curves

Several experimentalists (31, 32) have produced layers with edges tapered or otherwise treated. Methfessel et al. (32) have, for instance, observed in such films magnetic characteristics somewhat similar to those reported here. Never, however, was the internal

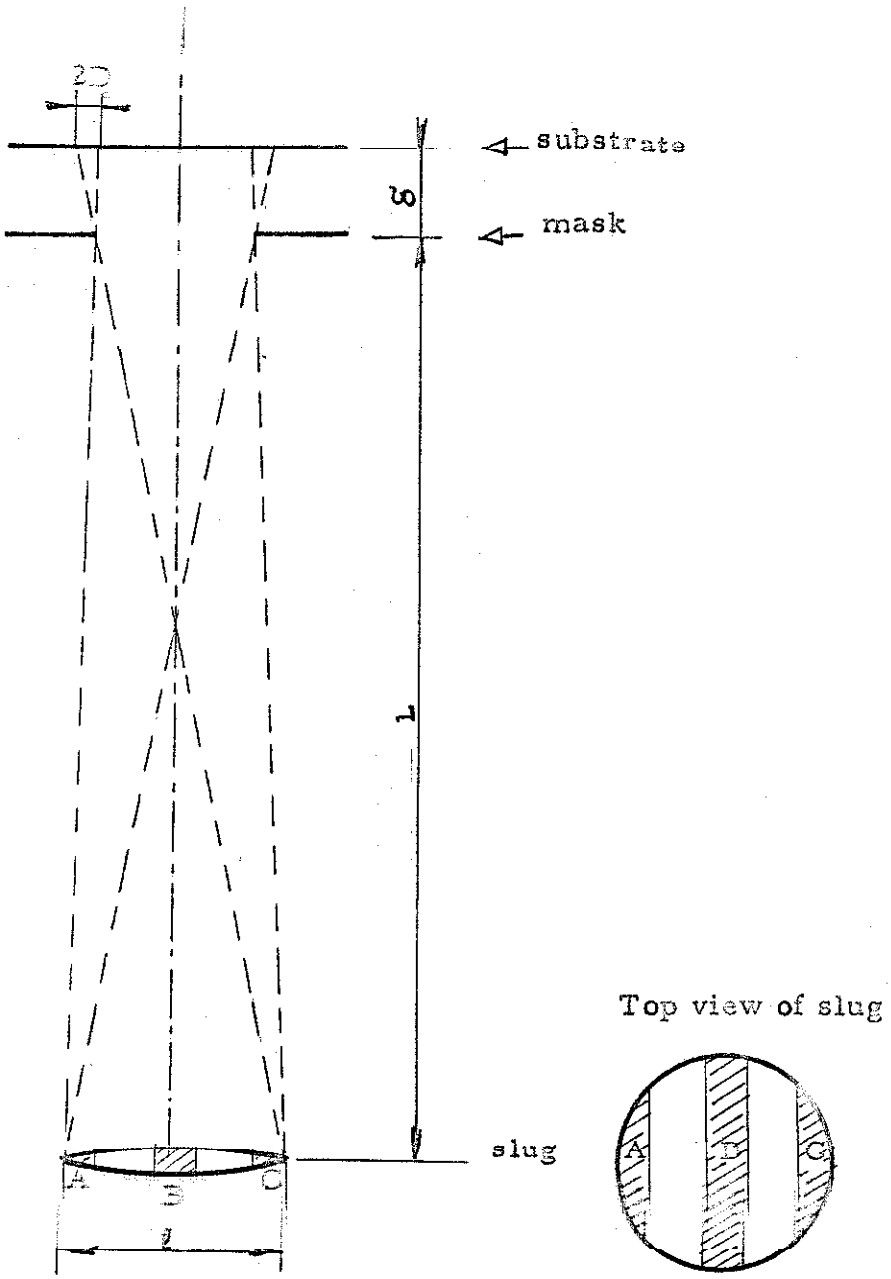

Fig. 5-14

Geometrical arrangement of mask with respect to substrate producing a tapered edge

field distribution (Section 5.1.2) taken into consideration in order to explain the results.

If the tapering is sufficiently pronounced, the M-H curve along the easy direction will be drastically altered. Figure 5-16 shows two loops obtained with the same film (of the order of 2000 Å). Curve "a," a perfectly square loop, is characteristic of an abrupt switching; curve "b" is the figure normally observed for a film of such thickness. In the first case, "a," all edge domains have been erased by an external field: nucleation of a reverse domain occurs at a negative field $-H_1$, and propagation across the entire film follows immediately; if the alternating drive field exceeds a given minimum value, at each alternation the film will be forced back into a single domain including the edges. For the second case, "b," the drive is reduced so that even when the flux apparently reaches saturation, nuclei of reverse magnetization such as those described in Section 5.2.2 are still present along the edges (point B on the curve). Thus, growth of these domains and propagation of the walls will readily follow the variations of the external field. Of course, if the tapered edges are etched away, a type "b" hysteresis loop will be obtained at high as well as at low drives.

Observations with the Kerr apparatus confirm the absence of any peaks of reverse magnetization in case "a" for decreasing fields between points A and C. The switching occurs suddenly when the

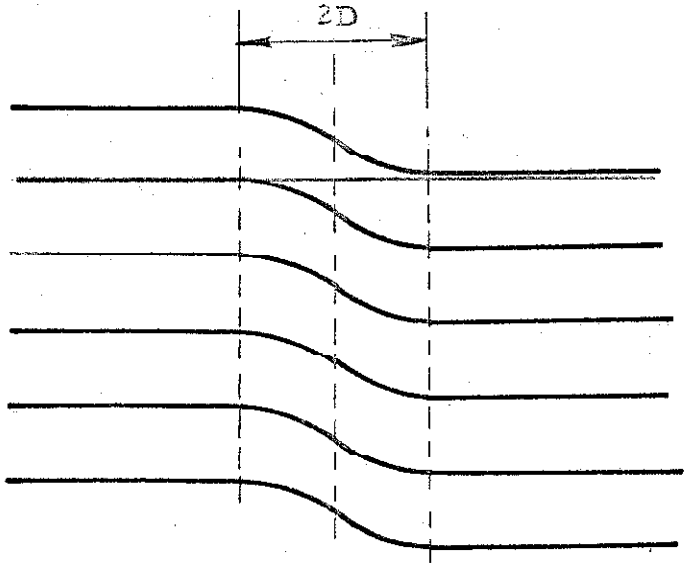

Fig. 5-15

Interference pattern at a tapered edge
(half-wavelength of light : 2675 Å)

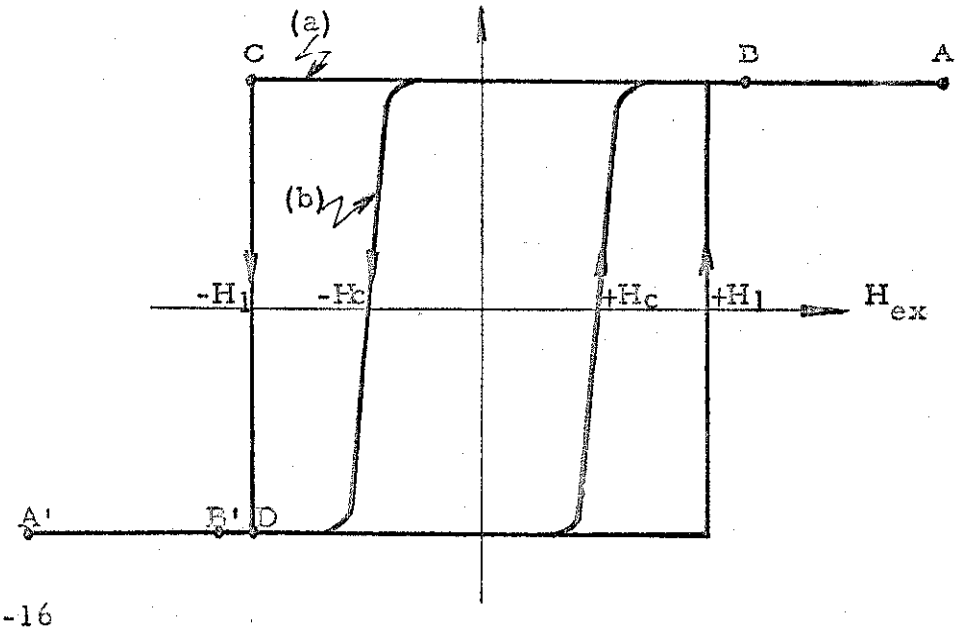

Fig. 5-16

Hysteresis curves of a film with tapered edges
curve (a) : at high drive along the easy axis
curve (b) : at low drive along the easy axis

field reaches a critical value $-H_1$, and it is impossible to observe any intermediate state of magnetization between points C and D. At D, some small areas along the edges are still unswitched, and are erased by the application of a larger negative field.

For a smaller drive corresponding to the hysteresis loop "b," the situation is that pictured in Figure 5-11, where the movement of the walls can be observed continuously.

An explanation of the type "a" hysteresis loop is that, if nucleation is inhibited, propagation--that is, reversal--cannot take place. Creation of a nucleus, as stated previously, is governed by the equation (the fields H_{ex} and H_i being parallel to the easy direction):

$$H_{ex} + H_i = - H_n$$

The nucleation field H_n is an intrinsic property of the film (Section 5.2.1). If H_n is assumed uniform over the film, the maximum $|H_i(x,y)|$ will determine the critical field H_1 at which the film will switch abruptly:

$$H_1 = -H_n - H_{i_{1\,max}} \qquad (5.3\text{-}1)$$

Little, if anything, is known about the mechanism by which a nucleus of reverse magnetization is formed. Experimental observation indicates that nuclei appear generally at the edges perpendicular to the easy direction where the internal field H_i reaches a maximum

value (Section 5.1.2). This field could also reach high values accidentally at inclusions or scratches and irregularities along the lateral sides of the film, parallel to the easy direction (Fig. 5-17), and nuclei are, at times, observed at such locations.

The magnetization rotation of 180°, occurring at the site where a nucleus is formed, will most likely take place within the plane (x,y) of the layer rather than outside it, where the demagnetizing field would reach high values of the order of $-M_z$. This phenomenon is probably controlled by the planar anisotropy $\varepsilon_a = K \sin^2\theta$, among other factors such as the demagnetization and the wall energies associated with the rotation. If the average anisotropy energy were the only term to be considered, in this local magnetization rotation, the nucleation field would theoretically be H_k (Section 2.4). The value of the anisotropy K as well as the easy direction, however, vary from one point to the other, so reversal will occur where H_k is the smallest and the angular dispersion of the easy axis maximum, or, more correctly, where the combination of these two factors is most favorable (Fig. 5-18). Contributing also to the phenomenon of nucleation are the demagnetization and exchange energies due to the interaction of the nucleus with the surrounding domain. The nucleation field H_n will actually be higher than the value determined on the basis of the local anisotropy only. An accurate prediction of the field H_n

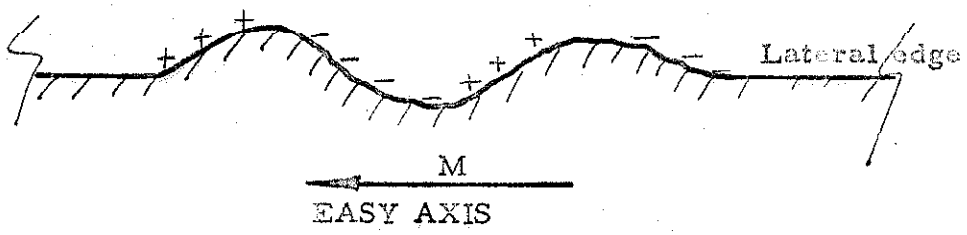

Fig. 5-17 Lateral edge parallel to the easy direction with irregularities producing internal fields

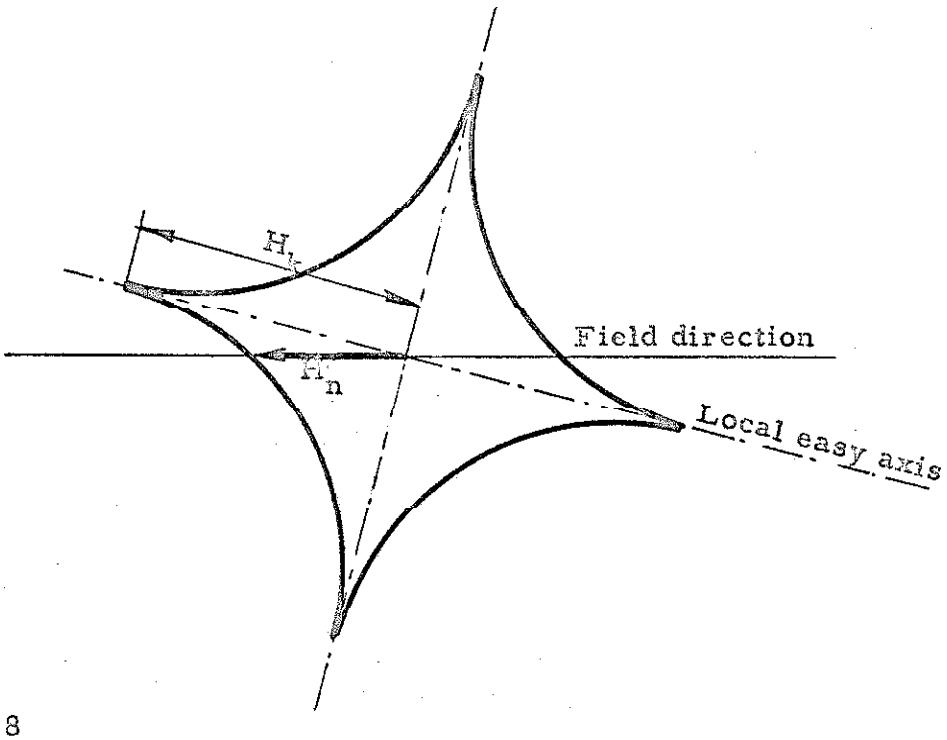

Fig. 5-18 Influence of dispersion of the easy axis on nucleation field

does not seem feasible, and it is assumed that $H_n = n H_k$, with n probably of the order of unity.

The effective field exerting an action on the magnetization vector is the sum of the externally applied field $\vec{H}_{ex}$ and the internal field $\vec{H}_i$. Thus, a map of $\vec{H}_i$ is also a necessary item of information. The direction and amplitude of the field $\vec{H}_{eff}$ varies from one location to the next. The preceding discussion of the nucleation field H_n was relative to the easy direction and applies only when $\vec{H}_{eff}$ is parallel to the x axis. Actually, a different nucleation field exists for every possible direction of the effective field and, therefore, $\vec{H}_n$ should be represented by a polar diagram. A nucleus of reverse magnetization would then appear whenever the vector $\vec{H}_{eff}(x,y)$ falls outside the diagram of $\vec{H}_n(\alpha)$ (Fig. 5-19). The "reversal" of the $\vec{M}$ vector is defined in the most general way as occurring when the direction of $\vec{M}$ changes quadrant.

The field $\vec{H}_i(x,y)$ has been investigated at regular points in the interior of the film (Section 5.1.1) and at the edges perpendicular to the easy axis (Section 5.1.2) where it is highest. Thus, from equation (5.3-1):

$$H_l = - n H_k + k \frac{Mt}{2\pi D}$$

where n and k are both of the order of unity. If the edge has not been purposely tapered, $H_{i\,max}$ is extremely large (see Table 5-I)

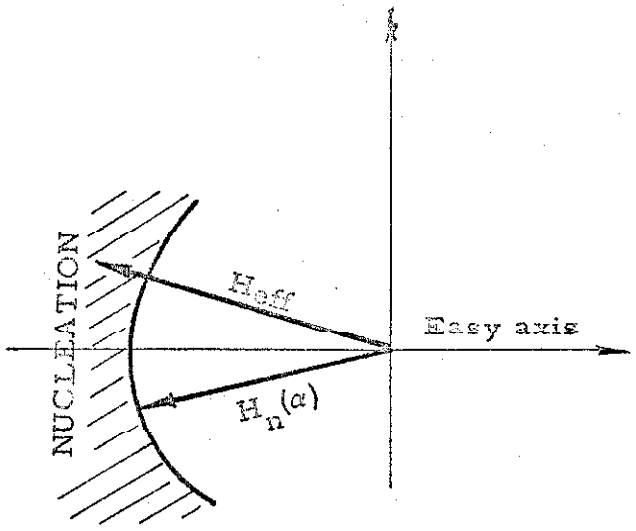

Fig. 5-19

Nucleation field varying with direction of effective field

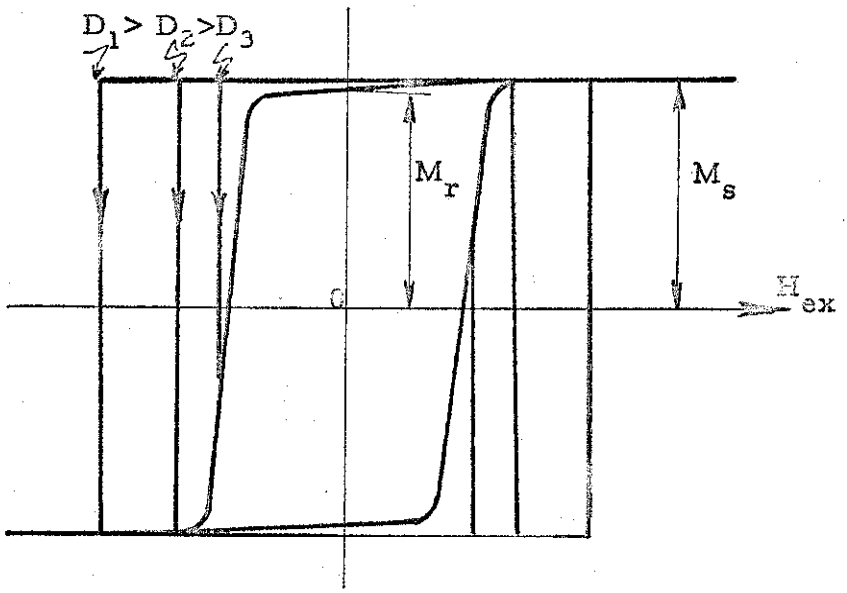

Fig. 5-20

Variation of M-H curve with profile of edge

$H_1 \simeq H_{i\,max}$; nuclei systematically appear under positive external fields. On the other hand, for small enough ratios t/D, H_1 becomes negative and tends toward $-H_n$. It is when $|H_1|$ becomes larger than the propagation field H_w that the M-H loop takes the very square shape of curve "a" in Figure 5-16. For films of identical thickness but varying profiles, $|H_1|$ should increase with increasing D, as shown in Figure 5-20.

As far as the nucleation field H_n is concerned, the understanding of it cannot even be considered to have reached the qualitative level and numerical data are scarce (33). Thus, the reproducibility of H_n is not insured from one series of films to another fabricated under seemingly identical conditions. Because of the present lack of knowledge about the formation of nuclei, the only meaningful experimental results will be those obtained when comparing films deposited during the same evaporation and of identical thickness. In that case, it is logical to assume that H_n varies within narrow limits. The propagation field itself is very dependent on thickness (Fig. 5-21). Nucleation being as complex, if not more so, than propagation, appreciable variation with thickness is very probable.

In an experiment four films (80% Ni) are evaporated onto a common substrate in order to avoid imhomogeneity in the glass. The four thicknesses are equal (1800 Å). A different spacing between glass and mask is chosen for each film: mask 1 is in contact with the

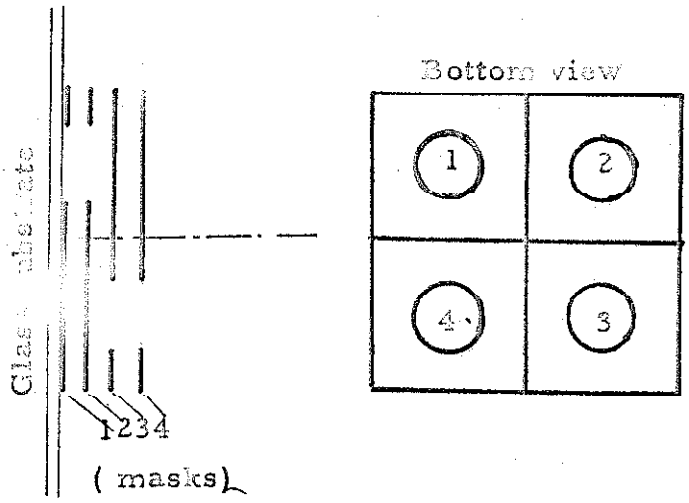

Fig. 5-22

Masks with different spacings δ from the substrate

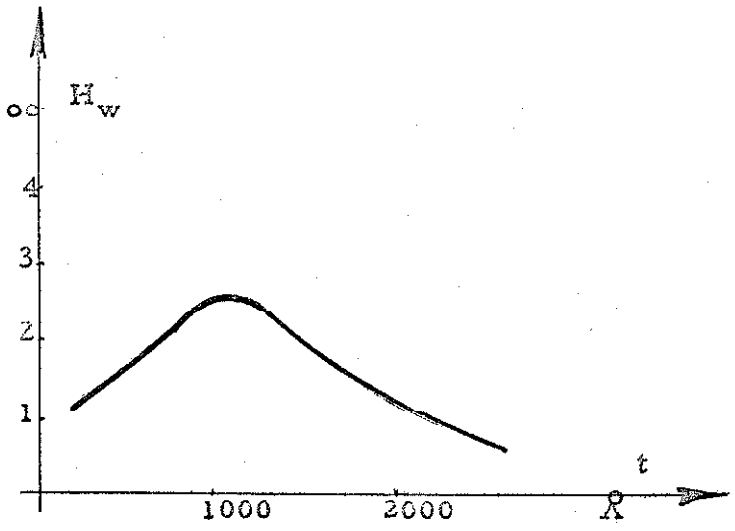

Fig. 5-21

Variation of propagation field with thickness

substrate so as to create the usual sharp edges; masks 2, 3 and 4 are away from it with increasing spacing and therefore increasing width 2D of the edge (Fig. 5-22).

Observation with the Kerr apparatus and hysteresis loop along the easy direction confirm the theory. In film 1 (sharp edge), the reversal occurs by slow wall motion: reverse peaks of magnetization grow towards the center. Films 2, 3 and 4 will switch abruptly and in succession, since H_i decreases (Table 5-I) and H_l increases (Table 5-II and Photographs D-2, 3, 4, 5 in Appendix D). Of course, if the thickness were large enough, the demagnetizing field H_i would be sufficient in films 2, 3 and finally 4, to create nuclei before wall propagation can take place; in this case, normal magnetic characteristics would be obtained.

Table 5-II

Film	H_k(oe)*	H_w(oe)*	H_l(oe)*	D	H_i(oe)**	H_n(oe)***
#1	8.5	1.2	---	$\simeq 0$	---	---
#2	8.5	1.2	-3.2	$\simeq$ 0.15mm	-3.5	6.7
#3	8.5	1.2	-3.7	$\simeq$ 0.30mm	-1.8	5.5
#4	8.5	1.4	-4.7	$\simeq$ 0.45mm	-1.2	5.9

* measured on hysteresis loop

** theoretical value

*** $H_n = |H_i| + |H_l|$

Some films, otherwise normal, present "soft" spots where nucleation occurs earlier. Such has often been the case in rectangular films where the nucleation expected at the edges perpendicular to the easy direction is masked by earlier nucleation along the sides parallel to it. As indicated previously, the creation of a nucleus along the side involves less wall energy, and irregularities, such as a serrated edge (Fig. 5-17) create appreciable demagnetization where none would appear if the sides were perfectly straight. In order to do away with such a difficulty, the films in the previous experiment were circular with a tapered edge all around.

The usefulness of such magnetic characteristics as those of Photographs D-3, 4, and 5 along the easy direction is evident:

1) There is no demagnetization effect in a zero field: The remanent magnetization M_r is equal to the saturation value M_s. The squareness ratio M_r/M_s is one. This allows working with much higher thicknesses and therefore higher signals. For instance, if one observes a 4000 Å film with a normal edge in the Kerr apparatus with no field applied, it appears in a substantially demagnetized state. On the other hand, if the edge is sufficiently tapered, the film appears as a single domain.

2) The switching threshold H_1 is clearly defined: below it, no change in magnetization occurs at all; above it, the whole film switches at once. In this way, ill-defined switching fields due to

inhomogeneities of the propagation field over the sample disappear.

As far as the mode of reversal of the film is concerned, it is still by wall motion for low fields, the minimum velocity of the walls being determined by the effective drive field $(H_1 - H_w)$ (34). There is no apparent reason why switching at high fields, in regions II and III as defined by Humphrey and Gyorgy (6), should be affected unless demagnetizing effects have some influence on the mode of switching in the intermediate region II; this, however, has not been shown.

6. PRINCIPLE OF AN ANISOTROPY RECORDER

6.1 General

In Section 2.4, the uniaxial anisotropy, induced in a Permalloy film during vacuum deposition in the presence of an external field parallel to the plane of the substrate, was characterized by an energy $\epsilon_a(\theta)$, a function of the direction of the magnetization in the plane (x,y) of the film. If $\epsilon_a(\theta)$ is identical at all points in the film, and if the external field is uniform, the $\vec{M}$ vector is everywhere parallel to the same direction and the state of magnetization of the film is then determined by a single parameter θ, the angle between $\vec{M}$ and the easy axis of the sample. The function $K \sin^2\theta$ is usually chosen to approximate the anisotropy energy density $\epsilon_a(\theta)$, in which case the equilibrium state of the film is given by equation (2.4-5) with its graphical interpretation in Figure 2-4. In particular, this function accounts for the almost linear M-H curve found in most films when the drive field is applied along the hard axis.

Even if the anisotropy is in fact of the form $K \sin^2\theta$ at all points, the amplitude K, as well as the local direction of the easy axis, might well vary from one point to the next. Such dispersion

has been observed in actual films (35). These variations result in changes of direction of $\vec{M}$ throughout the film. Rounded corners and opening of the hysteresis loop in the hard direction can be explained by dispersion of, respectively, the coefficient K and the direction of the easy axis. The concept of a film with uniform direction of magnetization is therefore a somewhat simplified picture. Thus, when studying a sample with such instruments as a hysteresis loop tracer, a torquemeter or the apparatus to be described in this section, it should be kept in mind that the quantities measured represent in some sense average values over the whole of the film.

In a single domain under the influence of a uniform field $\vec{H}$, the energy density is given by the following equation (from Sections 2.3 and 2.4):

$$\epsilon(\theta) = \epsilon_a(\theta) - \mu_o HM \cos(\alpha-\theta) \qquad (6.1\text{-}1)$$

where θ and α determine the directions of $\vec{M}$ and $\vec{H}$ in the plane (x,y) of the film (Fig. 6-1). At equilibrium, this energy is minimal and the torques are equal and opposite. (In a circular film, oriented as a single domain, the demagnetizing field is directly opposed to $\vec{M}$, and does not produce any torque.)

$$\frac{\partial \epsilon}{\partial \theta} = \frac{\partial \epsilon_a}{\partial \theta} - \mu_o HM \sin(\alpha-\theta) = 0 \qquad (6.1\text{-}2)$$

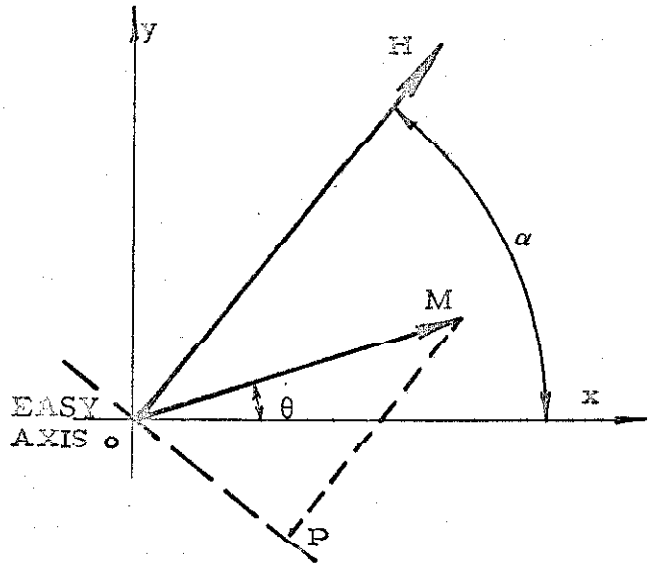

Fig. 6-1 Positions of vectors H and M in the plane of the film

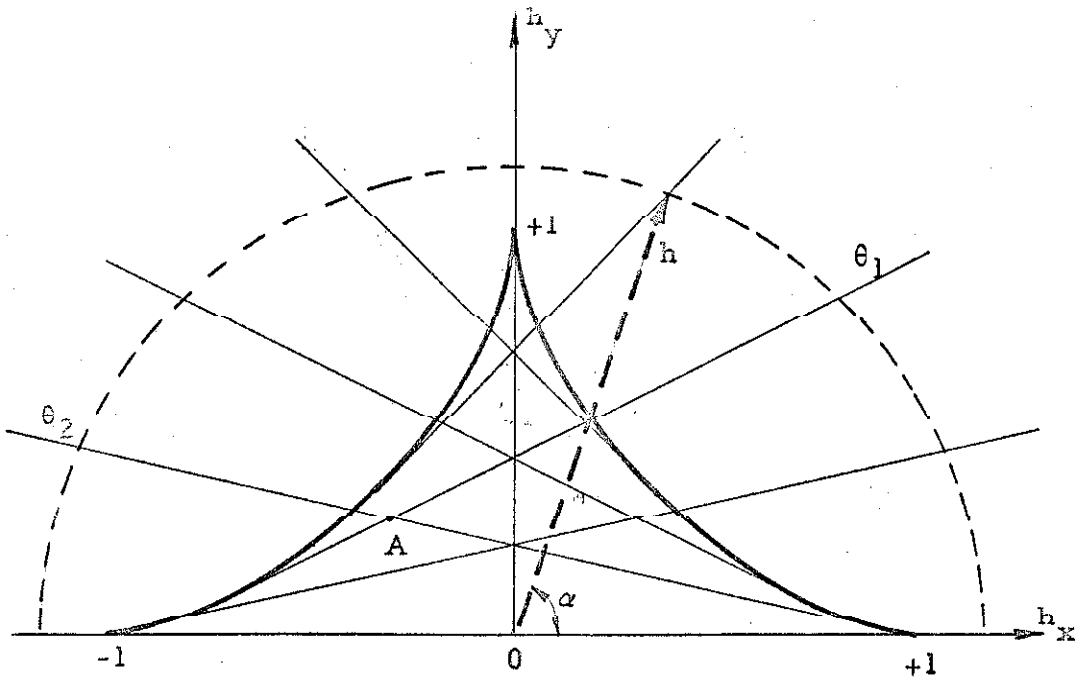

Fig. 6-2 Polar diagram of the reduced field h showing angle θ at equilibrium

The main features of diagram 2-4 are reproduced in Figure 6-2. Similar graphs would be obtained for more complicated anisotropy energies. The general property of interest is that there will always be a minimum field H_a ($H_a = 2K/\mu_o M$ if $\epsilon_a = K \sin^2\theta$) above which, regardless of the value of α, the direction of magnetization is uniquely determined (only one value of θ corresponds to a stable equilibrium).

At present, the anisotropy energy, or rather its first derivative, can be determined by several methods. The M versus H curve along the hard direction of the material gives complete information provided the single domain state is preserved. Indeed, the vertical ordinate of the M-H curve is $M \cos(\alpha-\theta)$, and the quantity $(\alpha-\theta)$ is all that is needed to compute $\partial\epsilon_a/\partial\theta$, H being known. However, in the majority of cases, in which the sample does not behave as a single domain, this procedure is inapplicable. Rossing and Stolen (36), in studying thin films, have used a procedure where the angle $(\alpha-\theta)$ is measured point by point for all directions α of the field, preserving at all times a single domain state.

Another method for analyzing the anisotropy uses a torquemeter (37). Penoyer (38) has proposed an automatic version of such an instrument, recording $\partial\epsilon_a/\partial\theta$ directly, while $\vec{H}$ is rotated by 2π. Boyd (39) improved the sensitivity by supporting the sample with a fiber instead of a bearing, and by using damping oil baths against lateral vibration. Humphrey and Johnston (13) have recently constructed

an automatic torque balance using a fused-silica torsion fiber. The quality of design of this apparatus is such that they were able to reach a sensitivity of 10^{-6} dyn-cm, a value very well adapted to the study of ferromagnetic films and several orders of magnitude better than previous instruments of the same type.

The torsion pendulum method (41) and other indirect experimental procedures such as measurement of ferromagnetic resonance, permit study of the regional behavior of the anisotropy around the state of equilibrium (e.g., study of stiffness $\partial^2\epsilon/\partial\theta^2$).

The new method presented here for the measurement of $\partial\epsilon_a/\partial\theta$ is particularly suitable for thin ferromagnetic films. It offers simplicity of design and is not affected by vibrations. Its sensitivity is as high as that of a hysteresis loop tracer, to which it is somewhat related.

6.2 Principle of the Method

Equation (6.1-2) may be written:

$$\frac{1}{\mu_o M} \cdot \frac{\partial \epsilon_a}{\partial \theta} = H \sin(\alpha-\theta) \qquad (6.2\text{-}1)$$

The quantity $\sin(\alpha-\theta)$ is proportional in Figure 6-1 to the segment OP, or physically to the flux in the direction perpendicular to $\vec{H}$.

The magnetic film of circular form is rotated around its center at a constant speed ω. A fixed dc field $\vec{H}$ is applied to the rotating

sample. A coil, at right angles to the field, is located above the film. The flux Φ through this coil is proportional to the component of $\vec{M}$ which is perpendicular to $\vec{H}$. Because the sample is circular, rotates around its center, and is a single domain, the proportionality between $\sin(\alpha-\theta)$ and Φ is insured. Indeed, if these three conditions are fulfilled, the geometrical factor between sample and coil remains constant for any orientation of $\vec{M}$. Hence, it is permissible to rotate the film rather than the field.

If the field is greater than H_a, as defined in Section 6.1, the movement of $\vec{M}$ will be an oscillation around $\vec{H}$ of period π/ω. In Figure 6-2, the points on the circle of radius $h = H/H_a$ determine the variation of $\vec{M}$. The angle $(\alpha-\theta)$ decreases when h increases and the maximum sensitivity will be achieved when $H = H_a$.

When the sample is saturated along its easy direction, and then rotated in the absence of a field, a sine wave $M \sin \omega t$ appears on the oscilloscope, displaying the integrated signal ($e = -d\Phi/dt$) from the pickup coil.

Finally, it should be noted that $M \sin(\alpha-\theta)$ appears on the oscilloscope as a function of $\alpha = \omega t$, the angle between the field and the easy direction $\theta = 0$ in the film. The value of $\sin(\alpha-\theta)$ is obtained by dividing $M \sin(\alpha-\theta)$ (curve b of Fig. 6-3) by the maximum amplitude of $M \sin \omega t$ (curve a). The values of α and $\sin(\alpha-\theta)$ being known, θ is then obtained by a straightforward calculation:

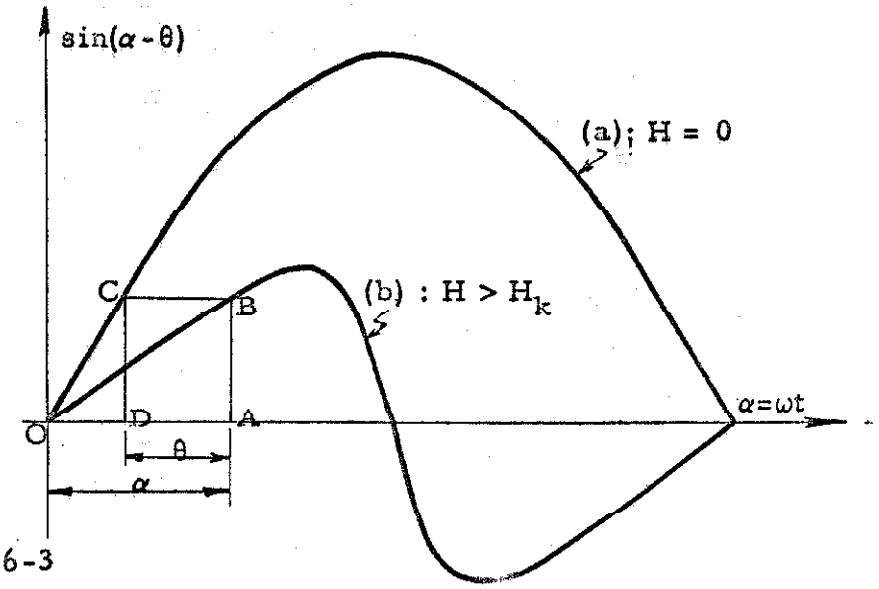

Fig. 6-3

Graphical method to determine the angle θ corresponding to a given α

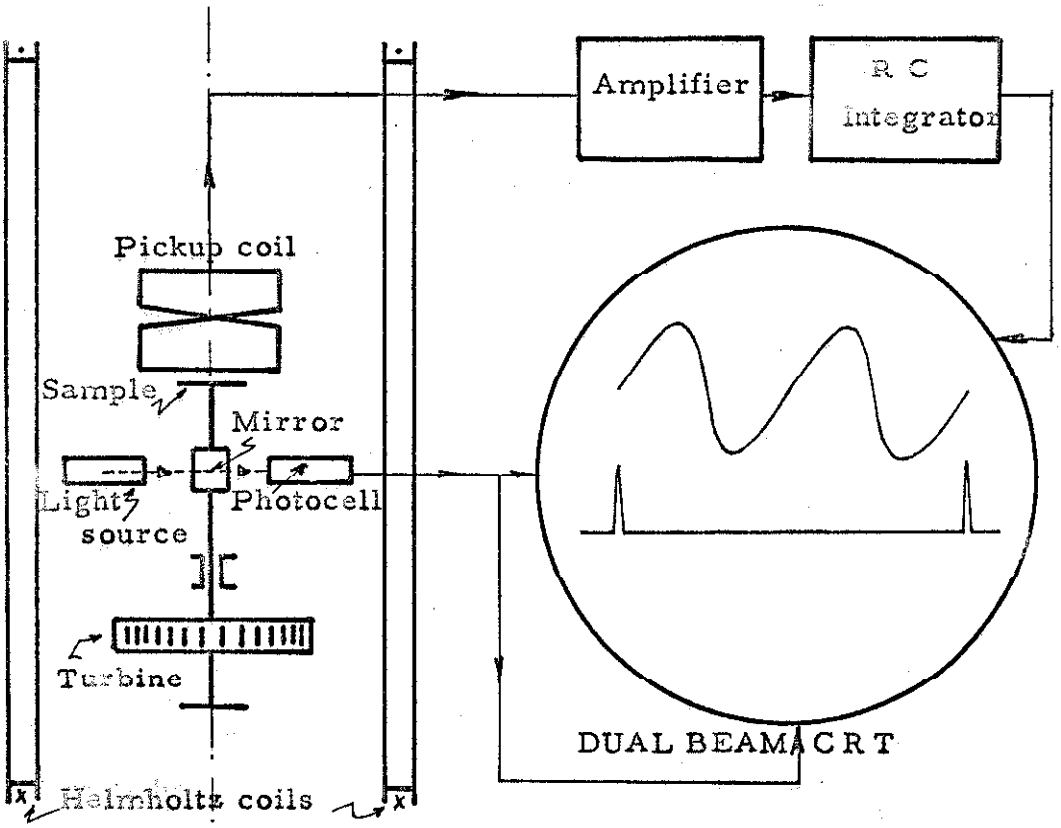

Fig. 6-4 | Schematic representation of anisotropy recorder and related electrical circuit

$$\theta = \alpha - \arcsin(\sin(\alpha-\theta)) \qquad (6.2-2)$$

A graphical method may be used to determine θ. It is rapid but lacks accuracy. Figure 6-3 shows the simple steps involved: α = OA and $\sin(\alpha-\theta)$ = AB = CD; thus, $(\alpha-\theta)$ = OD and, finally, θ = DA.

6.3 Apparatus

A schematic of the instrument is given in Figure 6-4. A uniform dc field $\vec{H}$ is produced at the center of a pair of Helmholtz coils. The current passing through that circuit is supplied by a set of batteries. In normal operating conditions, the axis of the pickup coil is perpendicular to the field; this is easily accomplished by searching for a zero reading in an ac field. In order to cancel most of the ambient 60 cycle field, the coil is composed of two identical parts. The flux through the lower part of the coil is composed of the flux of the rotating film as well as the 60 cps magnetic noise. The upper part wound in the opposite direction balances the noise (within approximately 1%) without reducing appreciably the useful signal. This "figure 8" coil is connected to a preamplifier (gain: 1000, bandwidth: 2 to 40,000 cycles), followed by an RC integrator (time constant: 0.1 sec). The circular film, one cm in diameter, is fixed on a platform parallel to the field $\vec{H}$. The axis of rotation should coincide with the center of the film. An extremely simple air turbine equipped with air bearings and built out of Lucite

eliminates the presence of magnetic materials and of an electric motor. The turbine is operated at 200 cps (non-critical) either clockwise or anti-clockwise. Its speed is regulated with a fine adjustment valve. A light source, a mirror fixed to the shaft of the turbine, and a photocell provide a triggering signal for the oscilloscope. The unit containing the light source and photocell can be rotated manually around the axis of the turbine so as to permit triggering at any time during a cycle. The earth's field is canceled, as required when working with very soft ferromagnetics.

6.4 Accuracy and Sensitivity

The accuracy depends on the exactness of the readings on the photograph. If the linearity of the oscilloscope is not satisfactory, the instrument can be calibrated. Only relative values of the deflections are meaningful: the vertical signal is calibrated by the maximum amplitude of the sine wave (Fig. 6-3, curve a) and the horizontal one by the distance corresponding to half a period of rotation displayed on almost the entire width of the screen. It is possible to read distances on the photograph within 0.25 mm. If 180° corresponds to 8 cm horizontally and the amplitude of the curve $M \sin \omega t$ is of the order of 3 cm (optimum values), then α and $\sin(\alpha - \theta)$ can be measured within, respectively, ± 0.75 degree and ± 0.01. The computed angle θ can thus be determined within 1 to 2 degrees. If the vertical signal

is too small when displaying sin $(\alpha-\theta)$, which is the case when H is much greater than H_a, the gain can be increased using the calibrated attenuator of the vertical amplifier of the oscilloscope (accuracy 1%), unless, of course, the noise becomes appreciable.

The bandwidth of the amplifier is limited to 40 kc; the integrator further reduces the high frequency noise. It is the 60 cps magnetic flux through the sensing coil and the low frequency flickering of the preamplifier which limit the signal-to-noise ratio. This particular instrument is able to detect 10^{-11} Wb in terms of magnetic flux inside the sample; at this value, corresponding to a 10 Å, 80% Ni film, one cm in diameter, the useful signal is comparable to the amplitude of the 60 cycle noise. Photograph D-6 (Appendix D) is an example of a 150 Å film (70% Ni). The range of thicknesses over which this instrument can operate extends from about 100 Å to several thousands (the thicker films should have tapered edges to prevent demagnetization).

If extremely small or thin samples were to be studied acurately, the following modifications might improve the sensitivity of the instrument. The number of turns in the pickup coil should be increased in order to obtain a signal sufficiently larger than the intrinsic noise of the preamplifier. In an attempt to reduce the ambient 60 cycle field, a Mumetal shield could be used to protect the anisotropy recorder. As a further improvement, the lower part of

the pickup coil could tightly surround the sample, thus increasing the useful flux together with decreasing the 60 cps noise. Such an arrangement would very much complicate the design of the apparatus if one keeps in mind that the film should rotate inside the coil.

6.5 Utilization and Examples

On the screen of the oscilloscope (Appendix D, Photograph D-7), $M \sin(\alpha-\theta) = (\mu_o H)^{-1}(\partial \epsilon_a / \partial \theta)$ is displayed as a function of α. The sine wave is obtained by saturating the film along the easy axis and then rotating it in a zero field. Its maximum amplitude equal in fact to the remanent magnetization M_r, rather than the saturation magnetization M_s, provides a calibration of the vertical deflection. In the thinner films or those with tapered edges (Section 5.3.2 and Photographs D-3, 4 and 5), the ratio M_r/M_s, as deduced from the hysteresis loop along the easy direction, is very close to one. A correction should be introduced if it is otherwise. The easy axis corresponding to the point $\theta = \alpha = 0$ is most easily determined on the sine curve $M \sin \omega t$.

As already mentioned, the pickup coil can be oriented with its axis parallel to the field. This arrangement permits use of the instrument as a hysteresis loop tracer, which may be useful when comparison is being made between the anisotropy function and hysteresis curves at different angles. In this case, α is constant, i.e., the sample is at rest, and the dc field is replaced by an alternating one. The pickup coil, wound as a "figure 8," insures

attenuation down to 1% of the unwanted signal due to the uniform sinusoidal field. Complete compensation for this signal can easily be obtained with a small auxiliary bucking coil. In summary, the transformation from an anisotropy recorder to an M-H curve tracer is accomplished by rotating the pickup coil by 90° and applying an ac field to the Helmholtz coils. The pickup coil circuit remains essentially unmodified.

As an example, a 60% Ni film (obtained from a slug containing 70% Ni) will be considered. Its thickness is 2500 Å and its edges are tapered. This film features usual hysteresis loops along the easy and hard axes. The anisotropy field H_k (eq. 2.4-4), measured on the hysteresis curve of the film along the hard direction, is about 6 oe. The dc field H_1 used to trace the $\sin(\alpha-\theta)$ curve is equal to 7.4 oe. Table 6-I reproduces the data measured on the recording obtained with the anisotropy recorder (Appendix D, Photograph D-7). The value of θ is computed for each α according to equation (6.2-2). The experimental function $\sin(\alpha-\theta) = (\mu_o MH)^{-1} (\partial \epsilon_a / \partial \theta)$ is represented in Figure 6-5 as a function of θ, and within the limits of precision of the method is a sine wave.

If $\epsilon_a = K \sin^2\theta$, and if equilibrium is established, then, from equation (6.1-2):

$$\frac{1}{\mu_o M} \frac{\partial \epsilon_a}{\partial \theta} = H_k \frac{\sin 2\theta}{2} = H \sin(\alpha-\theta)$$

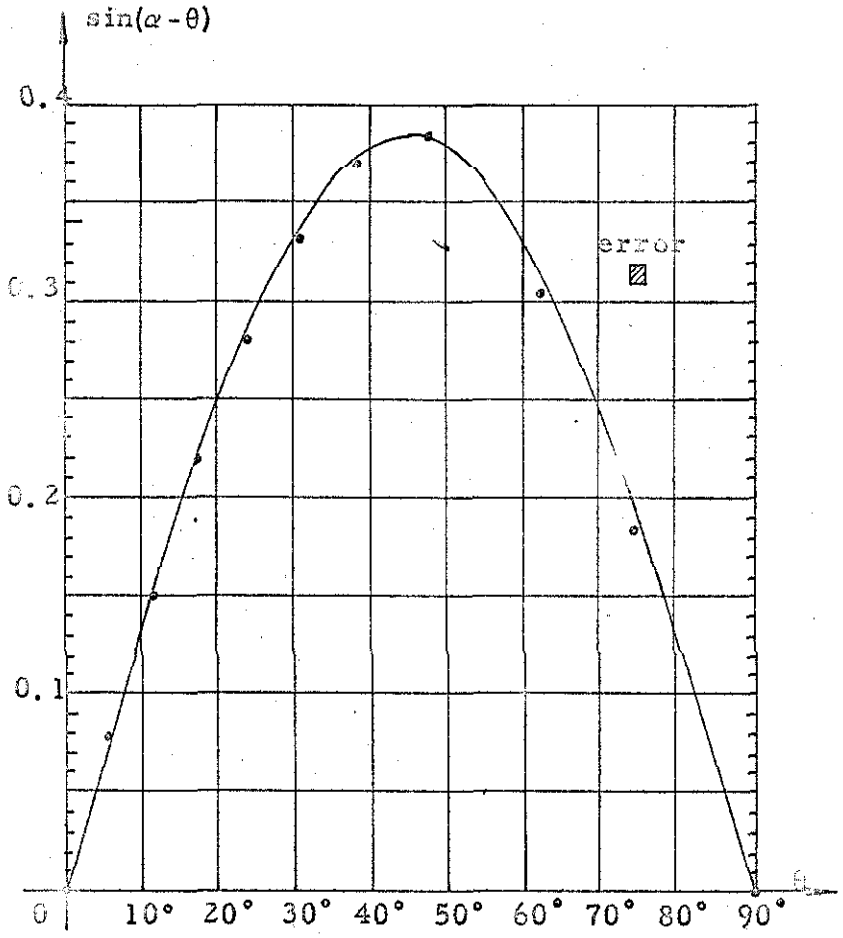

Fig. 6-5 sin $(\alpha-\theta)$ as a function of θ (Table 6-I)
the solid line represents a pure sine wave

and $H_k = 2H[\sin(\alpha-\theta)]_{max}$ at $\theta = 45°$. The value of H being known, H_k is deduced extremely easily from Photograph D-7 where $[\sin(\alpha-\theta)]_{max}$ can be measured without calculating θ.

Table 6-I

α	$\sin(\alpha-\theta)$	$\alpha-\theta$	θ
0°	0.00	0	0
10	0.08	4°.6	5°.4
20	0.15	8 .6	11°.4
30	0.22	12 .7	17°.3
40	0.28	16 .2	23°.8
50	0.33	19 .1	30°.9
60	0.37	21 .7	38°.3
70	0.385	22 .6	47°.4
80	0.305	17 .8	62°.2
85	0.183	10..5	74°.5
90	0	0	90°

The product $2H[\sin(\alpha-\theta)]_{max}$ should in principle be a constant. This product (Table 6-II) is reproduced on Figure 6-6 as a function of H, showing a variation of about 5% which could result from dispersion in either K or the local easy axis throughout the sample. With the increasing external field being applied, the dispersion of $\vec{M}$ becomes less and less pronounced. Photograph D-8 in Appendix D is the domain pattern of the demagnetized film; a slight dispersion of the

easy axis is noticeable, at least if one assumes that the direction of the walls is parallel to the easy axis at every point.

Figures 6-7 (Table 6-III) and 6-8 (Table 6-IV) represent the case of two other films containing, respectively, 53% Ni and 60% Ni. The $\sin(\alpha-\theta)$ curves (53% Ni film). corresponding to various values of H, appear on Photograph D-9 (Appendix D). Dispersion seems to be present in most films, and especially when departing from the 80-20 composition.

Table 6-II (60% Ni)

H	$\sin(\alpha-\theta)_{max}$	H_k
7.4 oe	0.385	5.7 oe
8.3	0.346	5.8
9.5	0.318	6.05
9.9	0.305	6.06
11.9	0.255	6.08

H_k deduced from B-H loop: 6 oe

Table 6-III (53% Ni)

H	$\sin(\alpha-\theta)_{max}$	H_k
10 oe	0.395	7.9 oe
11.9	0.352	8.40
15.9	0.278	8.85
19.9	0.226	9

H_k deduced from B-H loop: 8.5 oe

Table 6-IV (60% Ni)

H	$\sin(\alpha-\theta)_{max}$	H_k
7.6 oe	0.457	7.10 oe
11.6	0.305	7.10
16.2	0.220	7.15
18.	0.200	7.2
22.	0.166	7.3

H_k deduced from B-H loop: 7.2 oe

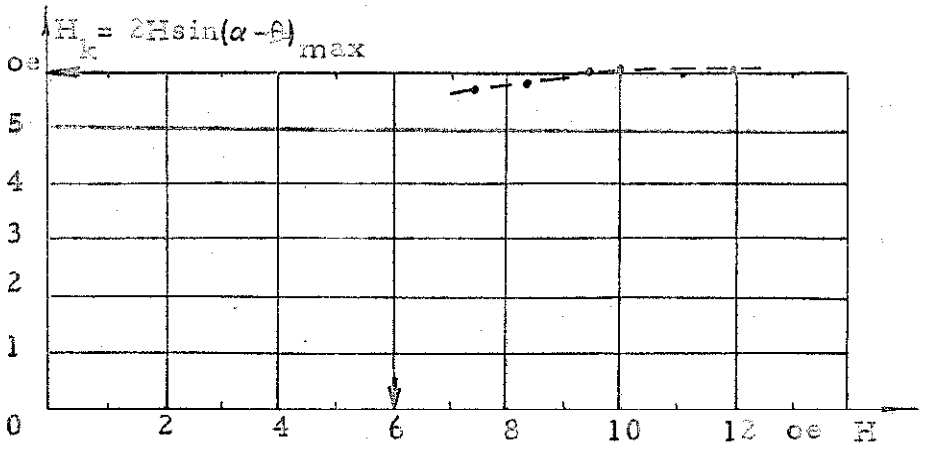

Fig. 6-6 60% Ni film. H_k as a function of H (Table 6-II)
(H_k=6 oe, deduced from MH loop)

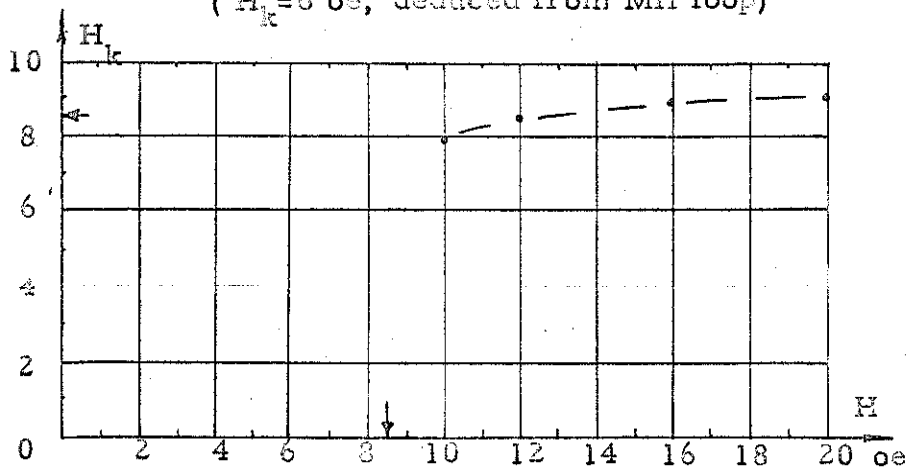

Fig. 6-7 53% Ni film. H_k as a function of H (Table 6-III)
(H_k = 8.5 oe, deduced from MH loop)

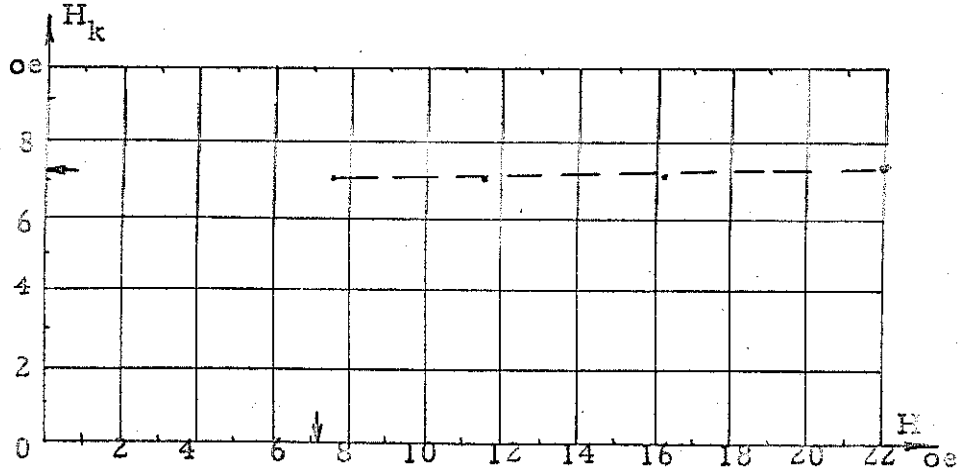

Fig. 6-8 60% Ni film. H_k as a function of H (Table 6-IV)
(H_k= 7.2 oe , deduced from MH loop)

6.6 Conclusion

The method presented here is only applicable to the study of films under small fields, since the amplitude of the signal tends toward zero for increasing H. Investigation at large fields requires the use of a torquemeter. For values of H of the order of the anisotropy field , the present instrument permits a rapid analysis of the anisotropy over the 360° range. The simplicity and small cost of this apparatus are evidently its attractive features. It is somewhat more complicated to build than an hysteresis loop tracer, but certainly simpler than a torquemeter.

The value of H_k (and its variation with H) determined with this recorder to an accuracy of about 2% reflects probably more nearly the anisotropy of the film than the hysteresis loop tracer, since the measurement is made in the single domain state.

APPENDIX A

Alternate Procedure for Solving the Torque Equation (3.6-4)

The method sketched hereafter has actually not been used, the first one proposed having proved to be successful. Therefore, it is not certain that the process as such would lead to convergent approximations of the function $\theta(y)$. Just as in Section 3.6, it might be necessary to introduce some modifications to insure stability and therefore convergence. This alternate method would have the advantage of not necessitating several trials in order to satisfy the boundary condition at infinity.

The equation to be solved is of the type:

$$\ddot{\theta}(y) = g(y)$$

with $g(y) \equiv \cos \theta(y) \cdot [\sin \theta(y) - h(y)]$, tending to zero when y tends towards infinity $[\dot{\theta}(\infty) = \ddot{\theta}(\infty) = 0]$. The boundary conditions are: $\theta(0) = \frac{\pi}{2}$ and $\theta(\infty) = 0$. It can easily be checked, by two successive differentiations, that the solution of this two-point boundary problem is of the form:

$$\theta(y) = A + By + \int_o^y (y - \eta)\, g(\eta)\, d\eta$$

$$\dot{\theta}(y) = B + \int_o^y g(\eta) d\eta$$

$$\ddot{\theta}(y) = g(y)$$

The boundary condition $\theta(0) = \frac{\pi}{2}$ will be satisfied by letting $A = \frac{\pi}{2}$. Also $B = -\int_o^\infty g(\eta)\, d\eta$ since $\dot{\theta}(\infty) = 0$, which automatically insures that $\theta(\infty) = 0$. Therefore:

$$\theta(y) = \frac{\pi}{2} - y \int_o^\infty g(\eta) d\eta + \int_o^y (y - \eta) g(\eta) d\eta$$

The function g(y) appearing inside the integrands is not known a priori, but a previous approximation of $\theta(y)$ may be used to compute an approximate g(y). The following formulas could thus be the base for the determination of $\theta(y)$ at a given thickness by successive interations:

$$g_n(y) = \cos \theta_n(y) \left[\sin \theta_n(y) - h_n(y)\right]$$

and $$\theta_{n+1}(y) = \frac{\pi}{2} - y \int_o^\infty g_n(\eta) d\eta + \int_o^y (y - \eta)\, g_n(\eta) d\eta$$

with h(y) derived from $\theta_n(y)$ as in equation (3.6-5).

The integrals could be computed step by step for increasing y by the Simpson's rule. For the purpose of limiting the abscissa axis, a finite value Y_∞ must be substituted to infinity, and this might introduce difficulties in matching $\theta(y)$ and h(y) at that point .

APPENDIX B

Numerical Solution of the Torque Equation of a Néel Wall

The functions $\sin\theta(y^*)$ and $h(y^*)$ are represented by tables of 201 values, as indicated in Section 3.6.1. The field given by equation (3.6-5) is calculated as follows:

$$h_i = C \sum_{j=1}^{100} \rho^*_j \left[\tan^{-1} \frac{t^*}{2(y^* - \eta^*)} - \tan^{-1} \frac{t^*}{2(y^* + \eta^*)} \right] \Delta\eta^*_1$$

$$+ C \sum_{j=101}^{200} \rho^*_j \left[\tan^{-1} \frac{t^*}{2(y^* - \eta^*)} - \tan^{-1} \frac{t^*}{2(y^* + \eta^*)} \right] \Delta\eta^*_2$$

where $\rho^*_j = \dfrac{\sin\theta_j - \sin\theta_{j+1}}{\Delta\eta^*}$ (defined at midpoints)

$$\eta^* = (j \pm \tfrac{1}{2})\,\Delta\eta^*_1 \text{ or } 100\,\Delta\eta^*_1 + (j - 100 - \tfrac{1}{2})\,\Delta\eta^*_2$$

However, due to the change of interval size at $y^* = Y_1$, a deformation appears in the h curve at that abscissa because of the abrupt change in the summation terms from $\tan^{-1}(t^*/\Delta y^*_1)$ to $\tan^{-1}(t^*/y^*_2)$. It is corrected by dividing the interval Y_1 to $Y_1 + \Delta y^*_2$ into p subintervals Δy^*_1 and assuming for these additional points a linear variation of ρ^*. Figure B-1 indicates the subdivision of Δy^*_2

as described above. In the new summation, negative and positive terms around $y^* = Y_1$ compensate each other to produce a smooth variation of $h(y^*)$. Thus, for $y^* \leq Y_1$ only, that is, $n \leq 101$, h will be given by

$$h_i = C\left[\sum_{j=1}^{100}(\rho^*_j\cdots)\Delta\eta^*_1 + \sum_{j=1}^{p}(\rho^*_j\cdots)\Delta\eta^*_1 + \sum_{j=102}^{200}(\rho^*_j\cdots)\Delta\eta^*_2\right]$$

with, in the interval Y_1 to $Y_1 + \Delta\eta^*_2$

$$\rho^*_j = \rho^*_{100} + \left[\frac{2(\rho^*_{101} - \rho^*_{100})}{\Delta\eta^*_1 + \Delta\eta^*_2}\right] j\Delta\eta^*_1$$

Another deformation appears at Y_∞ because the integration of $\rho^*(y^*)$ terminates at that abscissa. There, the curve $h(y^*)$ goes anomalously upwards, and this is corrected by substituting extrapolated values to the last ten h_i's calculated by integration. This extrapolation above i = 191 is of the form $A/(y^* - B)$, where A and B are chosen so that $h(y^*)$ and its first derivative are continuous at i = 191 (Fig. B-2). The boundary condition (3.6-7) is thus based on an extrapolated value h_{201}. The tail of the curve being of no physical significance, such a procedure is acceptable and does not introduce detectable errors at lower abscissae.

In solving the differential equation (3.6-4), the procedure followed in order to satisfy the boundary conditions is as explained

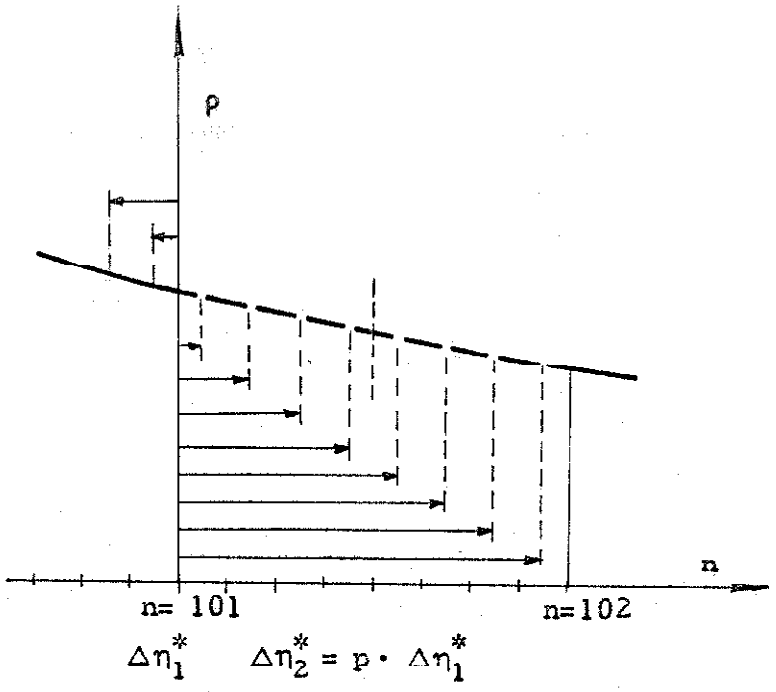

Fig. B-1 Interpolation of the ρ distribution in the interval Y_1 to $Y_1 + \Delta\eta_2^*$

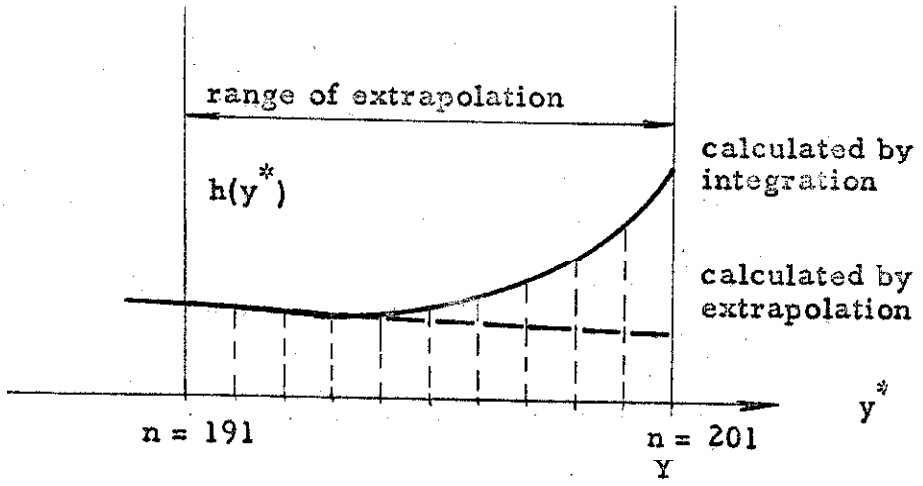

Fig. B-2 Extrapolated values adopted for $h(y^*)$ between n = 191 and n = 201

Section 3.6. The actual solution of the equation for a given $h(y^*)$ and a given slope $\dot{\theta}(o)$ at the origin is obtained with the help of a standard subroutine using the Runge-Kutta-Gill method to start the integration process and the Adams-Moulton predictor-corrector formulas for each integration step thereafter. The integration steps, smaller than $\Delta\eta^*$, are selected automatically so as to limit the truncation error to a predetermined maximum value. In between two consecutive values of the table defining the function $h(y^*)$, the field is assumed to vary linearly.

The iteration process starts at a zero thickness. A table of 201 values of $\sin\theta$ is first computed according to formula (3.5-3) valid for $t^* = 0$.

$$\sin\theta_i = \sin\left[2\tan^{-1}\left(e^{-y^*}\right)\right]$$

For $t^* \leq 0.02$, the interval sizes are $\Delta y^*_1 = 0.05$ and $\Delta y^*_2 = 0.4$, with $Y_1 = 5$ and $Y_\infty = 45$. For $t^* > 0.02$, the intervals are 0.04 and 0.8, with $Y_1 = 4$ and $Y_\infty = 84$. The transition at $t^* = 0.02$, from the first set of intervals to the second, is done with the help of simple interpolation formulas and an extrapolation of the type $\sin\theta = A/(y^*-B)$ between $y^* = 45$ and 84, the function and its first derivative being continuous at $y^* = 45$. An auxiliary program performs these operations.

The successive thicknesses chosen are, at the start, $t^* = 0$; 0.0008; 0.0013; 0.0024; 0.0036 and, thereafter, increasing in steps of 25%.

The correlation between the quantities appearing in Section 3.6 and their Fortran homologues is as follows:

h_i = H(I)	$\sin\theta_i$ = COSTH (I)
$\sin\theta'$ = PHO(I)	ρ^*_i = STHTA(I)
$t^*/2$ = HALFT	y^* = T
Δy^*_1 - DETA	Δy^*_2 = DELETA
Y_1 = A	Y_∞ = B
η = ETA	

THETA (1) and THETA (2): First two trial values of slope at origin.

JOY is the index used in numbering the successive trials of initial slopes at $y^* = 0$, or Y', Y'', etc.

JUY is the index used in dividing the abscissa axis in segments O to Y' (JUY = 0), Y' to Y'' (JUY = 1); Y'' to Y''' (JUY = 2), etc. (Section 3.6.2)

JAY is the index used in numbering each whole cycle expressed by the system of equations(3.6-6)

FORTRAN PROGRAM FOR THE IBM 7090 COMPUTER

```
      DIMENSION H(1001), ANGLE(1C01)
      DIMENSION PHONEG(50),DELNEG(50),PHOPOS(50),DELPOS(50)
      DIMENSION G(1001), Y(2), YDOT(2), PHOPRM (50), DELTA(50),
     1 PHO(1001),SUM(8),THETA(2),STHTA(1001),COSTH(1001)
     2,TEMPY(2),STHTB(100)
  500 FORMAT (I5, F10.6, 5F10.4)
  501 FORMAT  (  2F12.8)
   10 READ INPUT TAPE 5, 500, N, HALFT , A, B, C, ALPHA, BETA
      READ INPUT TAPE5,501,TEMPY
  502 FORMAT( 2I1C )
      READ INPUT TAPE 5,502, KARO,LARO
  510 FORMAT (25H1  NUMBER OF INTERVALS = I5, 7H   C = F10.2,
     17H   A = F10.2, 7H   B = F10.2, 9H   .5T = E13.6, 13H   EPSILON =
     2E13.6//)
  511 FORMAT (25H  INITIAL VALUES OF THETA//)
  512 FORMAT (//8H       Y, 17H             THETA,25H            1ST DERIV
     1ATIVE, 21H       2ND DERIVATIVE, 18H        SIN(THETA),
     215H            H(Y)//)
  513 FORMAT (F10.4, 5E20.8)
  514 FORMAT (5E20.6)
  515 FORMAT (23H       THETAPRIME(0) = E13.6)
      JAY = 0
      EPSLON=0.005
      WRITE OUTPUT TAPE 6, 510, N, C, A, B, HALFT, EPSLON
      CN = N
      DELYA = A/CN
      DELYB = (B-A)/CN
      DETA = DELYA
      DELETA = DELYB
      ETA = DETA*.5
      MN = N+1
      JACK = 2*N
      LM = MN+1
      ETA = 0.
      JOKE = JACK + 1
      JULES = 10
      READ INPUT TAPE 5, 5222, (COSTH(I) , I=1, JOKE)
      WRITE OUTPUT TAPE 6,518
      DO 1000 IJ = 1,JOKE,5
      NR = IJ+4
      WRITE OUTPUT TAPE 6,5160,IJ,(COSTH(I),I=IJ,NR)
 1000 CONTINUE
  100 JT = N+1
      NTWO=JOKE-JULES
      CJULES=JULES
      CONE=B
      DO 25 I = 2, MN
      STHTA(I-1) = -(COSTH(I)-COSTH(I-1))/DETA
   25 CONTINUE
      IF (BETA) 37,37,26
   26 CONTINUE
      DO 35 I = LM, JOKE
      STHTA(I-1) = -(COSTH(I)-COSTH(I-1))/DELETA
   35 CONTINUE
   37 CONTINUE
      WRITE OUTPUT TAPE 6, 517
```

```
 517 FORMAT (//30H          VALUES OF O(-SIN)/DETA )
     DO 1005 IJ = 1,JOKE,5
     NR = IJ+4
     WRITE OUTPUT TAPE 6,5160,IJ,(STHTA(I),I = IJ,NR)
1005 CONTINUE
5160 FORMAT (I10,5E20.8)
     DT = DETA
     T = 0.0
5000 FORMAT (4E20.8)
     DO 140 I = 1,JOKE
     SUM (1) = 0.0
     SUM (2) = 0.0
     SUM(3)=0.
     SUM(4)=0.
     ETA = DETA*0.5
     DO 120 KAY = 1, N
 115 G(KAY) = STHTA(KAY) * (ATANF(HALFT/(T-ETA))-ATANF(HALFT/(T+ETA)))
 116 ETA = ETA+DETA
     SUM(1) = SUM(1) + G(KAY)
 120 CONTINUE
     SUM(1) = SUM(1) * DETA
5111 FORMAT (1H I10,2E20.8)
     KO=DELETA/DETA
     SPRIME=2.*(STHTA(N+1)-STHTA(N))/(DELETA+DETA)
     DO122 KAY=1,KO
     CKAY=KAY
     STHTB(KAY)=STHTA(N)+SPRIME*CKAY*DETA
 122 CONTINUE
     DO 121 KAY=1,KO
     G(KAY)=STHTB(KAY)*(ATANF(HALFT/(T-ETA))-ATANF(HALFT/(T+ETA)))
     ETA=ETA+DETA
     SUM(3)=SUM(3)+G(KAY)
 121 CONTINUE
     SUM(3)=SUM(3)*DETA
 150 ETA = ETA+(DELETA-DETA) * 0.5
     DO 160  KAY=LM,JACK
     G(KAY)=STHTA(KAY)*(ATANF(HALFT/(T-ETA))-ATANF(HALFT/(T+ETA)))
     ETA=ETA+DELETA
     SUM(2)=SUM(2)+G(KAY)
 160 CONTINUE
     SUM(2)=SUM(2)*DELETA
     ETA=A+DELETA*.5
     SUM(4)=STHTA(N+1)*(ATANF(HALFT/(T-ETA))-ATANF(HALFT/(T+ETA)))
     SUM(4)=SUM(4)*DELETA
     IF(I-MN) 141,142,143
 141 H(I)=(SUM(1)+SUM(2)+SUM(3))*C
     T=T+DETA
     GO TO 140
 142 H(I)=(SUM(1)+SUM(2)+SUM(3))*C
     T=T+DELETA
     GO TO 140
 143 H(I)=(SUM(1)+SUM(2)+SUM(4))*C
     T=T+DELETA
     GO TO 140
 140 CONTINUE
     DTWO=B-CJULES*DELETA
```

```
      HTWO=H(NTWO)*DELETA/(H(NTWO)-H(NTWO-1))
      GTWO=HTWO+DTWO
      FTWO=-HTWO*H(NTWO)
      T=DTWO
      DO 600 I=NTWO,JOKE
      H(I)=FTWO/(T-GTWO)
      T=T+DELETA
  600 CONTINUE
      WRITE OUTPUT TAPE 6,519
  519 FORMAT (// 15H    VALUES OF H/)
      DO 1010 IJ = 1,JOKE,5
      NR = IJ+4
      WRITE OUTPUT TAPE 6,5160,IJ,(H(I),I = IJ,NR)
 1010 CONTINUE
      IF(JAY-8) 50,50,10
   50 CONTINUE
      JUY=0
      TJUY=0.0
      DELJUY=DETA
      KARJUY=0
      YJUY=1.5707963
      THETA(1)=TEMPY(1)
      THETA(2)=TEMPY(2)
   52 JOY=1
      DELJOY=0.0
      DELTOY=0.
      KAT=0
      MAT=0
      Y(2)=THETA(1)
      PHOTWO=THETA(1)
   51 T=TJUY
      Y(1)=YJUY
      KAR=KARJUY
      DELT=DELJUY
  520 FORMAT(//3E15.6)
   53 CALL DEQ(K, 2, T, Y, YDOT, DELT, 0.0001)
      GO TO (200, 300, 300, 400), K
  200 YDOT(1) = Y(2)
      IF(T-A) 201,201,202
  201 AT=T/DETA+1.0
      GO TO 203
  202 AT=CN+1.0+(T-A)/DELETA
      GO TO 203
  203 II=AI
      CIT = IT
      CAT = AT-CIT
      HY = (H(IT+1)-H(IT)) * CAT + H(IT)
      SINEY = SINF(Y(1))
  220 YDOT(2) = COSF(Y(1))*(SINEY-HY)
      CONTINUE
      CALL DEQ2
  300 IF(JOY-30) 306,306,299
  299 WRITE OUTPUT TAPE 6, 513, T, Y(1), Y(2), YDOT(2), SINEY, HY
  306 KAR = KAR +1
      PHO(KAR)=SINEY
  310 IF(DELT-DELETA) 311,326,326
```

```
 311 IF(ABSF(T-A)-0.0005) 325,325,326
 325 DELT=DELETA
     KAR=N
     GO TO 53
 326 IF((T+.00005)-CONE) 320,330,330
 320 CALL DEQ1
     GO TO 310
 330 DELTWO=Y(I)-1.005*ASINF(HY)
 521 FORMAT (8E15.6)
 522 FORMAT (/12H      JOY1 = I10)
     IF(ABSF((DELTWO-DELJOY)/DELTWO)-0.000001) 1440,301,301
1440 JARO=KARO+JUY*LARO
     WRITE OUTPUT TAPE 6, 522, JOY
     WRITE OUTPUT TAPE 6, 666, (PHONEG(I), DELNEG(I), I = 1, KAT)
     WRITE OUTPUT TAPE 6, 667, (PHOPOS(I), DELPOS(I), I = 1, MAT)
 666 FORMAT( 2E18.6)
 667 FORMAT (2E20.6)
     DO 1200 IJ=1,JOKE,5
     NR=IJ+4
     WRITE OUTPUT TAPE 6,5160, IJ,( PHO(I), I=IJ,NR)
1200 CONTINUE
     CJARO=JARO
     TJUY=A+(CJARO-CN-1.)*DELETA
     KARJUY=JARO-1
     YJUY=ASINF(PHO(JARO))
     YPRIME=(ASINF(PHO(JARO+1))-ASINF(PHO(JARO-1)))/(2.*DELETA)
     THETA(1)=YPRIME+0.1*ABSF(YPRIME)
     THETA(2)=YPRIME-0.1*ABSF(YPRIME)
     JUY=JUY+1
     DELJUY=DELETA
     IF(TJUY-CONE) 52,10,10
 301 IF(ABSF((DELTWO-DELTOY)/DELTWO)-0.000001) 1440,302,302
 302 GSIN=ASINF(HY)
     DELTOY=DELJOY
     DELJOY=DELTWO
     CONST = ABSF(DELTWO/GSIN)
     IF(CONST-EPSLON) 340, 350, 350
 340 JAY = JAY + 1
     GO TO 410
 350 IF(DELTWO) 1350, 1350, 1380
1350 KAT = KAT + 1
     PHONEG(KAT) = PHOTWO
     DELNEG(KAT) = DELTWO
     IF(JOY-2) 360, 1355, 1355
1355 PHOMAX = 0.
     DO 1370 I = 1, MAT
     IF(ABSF(PHOPOS(I))-ABSF(PHOMAX)) 1370, 1360, 1360
1360 PHOMAX = PHOPOS(I)
     DELMAX = DELPOS(I)
1370 CONTINUE
     PHOONE = PHOMAX
     DELONE = DELMAX
     GO TO 380
1380 MAT = MAT+1
     PHOPOS(MAT) = PHOTWO
     DELPOS(MAT) = DELTWO
```

```
      PHCONE = PHOTWO
      DELONE = DELTWO
      IF (JOY-2) 360, 1385,1385
 1385 PHOMIN = PHONEG(1)
      DO 1400 I = 1, KAT
      IF(ABSF(PHONEG(I))-ABSF(PHOMIN)) 1390, 1390, 1400
 1390 PHOMIN = PHONEG(I)
      DELMIN = DELNEG(I)
 1400 CONTINUE
      PHOTWO = PHOMIN
      DELTWO = DELMIN
      GO TO 380
  360 JOY = JOY + 1
      Y(2) = THETA(2)
      DELONE = DELTWO
      PHOONE = PHOTWO
      PHOTWO = THETA(2)
  361 CONTINUE
      IF(JOY-40)51,51,10
  380 THETA(2) = (PHCONE+PHOTWO)*.5
  523 FORMAT  (I10, 2E18.6)
  390 CONTINUE
      IF(THETA(2)) 360,391 ,360
  391 THETA(2) = -1.0
      JOY = 1
      GO TO 360
  400 WRITE OUTPUT TAPE 6, 516
  516 FORMAT(/31H           ERROR RETURN FROM DEQ)
      GO TO 10
  410 CONTINUE
  518 FORMAT(/25H     VALUES OF SIN(THETA)/)
      DO 1015 IJ = 1,JOKE,5
      NR = IJ+4
      WRITE OUTPUT TAPE 6,5160,IJ,(PHO(I),I=IJ,NR)
 1015 CONTINUE
 5222 FORMAT (4E15.8)
      DO 420 I=1,JOKE
      IF(JAY-5) 419,418,419
  418 COSTH(I) = (COSTH(I)+PHO(I))/2.
      GO TO 420
  419 COSTH(I)=(13.*COSTH(I)+PHO(I))/14.
  420 CONTINUE
      DO  1016  IJ=1,JOKE,5
      NR=IJ+4
      WRITE OUTPUT TAPE 6,5160,IJ,(COSTH(I),I=IJ,NR)
 1016 CONTINUE
      DO 425 I = 1, KAT
      PHONEG(I) = 0.
      DELNEG(I) = 0.
  425 CONTINUE
      DO 430 I = 1, MAT
      PHOPOS(I) = 0.
      DELPOS (I) = 0.
  430 CONTINUE
  450 WRITE OUTPUT TAPE 7,5222,(COSTH(I),I = 1,JOKE)
      GO TO 100
      END(1,0,0,0,0,0,0,0,0,1,0,0,0,1,0)
```

APPENDIX C

Computation of the Energy Density in a Néel Wall

The function sin $\theta(y^*)$ representing the shape of the wall is defined by a table of 201 values corresponding to 201 abscissae y^* in the ranges 0 to Y_1, divided in 100 intervals Δy^*_1, and Y_1 to Y_∞, divided in 100 intervals Δy^*_2. Maximum numerical accuracy being unnecessary, as indicated in section 3.7, the trapezoidal rule is used for the integration process. The integrand $I(y^*) = (\dot{\theta}^2 + \ddot{\theta} \tan \theta)$ is calculated at midpoints inside the intervals using simple interpolation formulas as those below:

$$\dot{\theta}_{n+\frac{1}{2}} = \frac{\theta_{n+1} - \theta_n}{\Delta y^*}$$

$$\ddot{\theta}_n = \frac{\dot{\theta}_{n+\frac{1}{2}} - \theta_{n-\frac{1}{2}}}{\Delta y^*}$$

with $\Delta y^* = \Delta y^*_1$ for $1 \leq n \leq 100$ and $\Delta y^* = \Delta y^*_2$ for $101 \leq n \leq 201$.

At $y^* = Y_1 (n = 101)$, $\ddot{\theta}_{101} = \dfrac{\ddot{\theta}_{100}\, \Delta y^*_2 + \ddot{\theta}_{102}\, \Delta y^*_1}{\Delta y^*_1 + \Delta y^*_2}$

and finally, defining $\alpha_n = \ddot{\theta}_n \tan \theta_n$:

$$I_{n+\frac{1}{2}} = \dot{\theta}^2_{n+\frac{1}{2}} + \frac{\alpha_n + \alpha_{n+1}}{2}$$

As determined previously in Section 3.7, $\alpha_1 = 1 + |h(0)|$, value completing the table of α's at $y^* = 0$, and which is derived from the internal field calculation of Section 3.6.5 (Fig. 3-23).

The integration is pursued up to $y^*_{171} = 100\ \Delta y^*_1 + 70\ \Delta y^*_2$, where $\tan\theta \simeq \theta < 0.1$ for all thicknesses considered here. Thus:

$$\gamma^*/2 = \sum_{n=1}^{100} I_{n+\frac{1}{2}}\ \Delta y^*_1 + \sum_{n=101}^{170} I_{n+\frac{1}{2}}\ \Delta y^*_2 - \theta_{171}\cdot\dot{\theta}_{171}$$

Table C-I summarizes the input data and results.

Table C-I

t^*	Y_1	Δy^*_1	Y_∞	Δy^*_2	α_1	γ^*
0.0	5	0.05	45	0.4	1	3.86
0.0084	5	0.05	45	0.4	13.25	10.84
0.020	5	0.05	45	0.4	38.8	17.61
0.040	4	0.04	84	0.8	99.5	27.92
0.060	4	0.04	84	0.8	169.5	36.58
0.080	4	0.04	84	0.8	242.5	43.65

The correlation between the quantities appearing in the preceding formulas and their Fortran homologues is as follows:

$\sin\theta_n$ = STHETA (I)	$\ddot{\theta}_n$ = THE TWO (I)	Δy^*_2 = DELETA
θ_n = THETA (I)	α_n = ALPHA (I)	$\gamma^*/_2$ = SUM
$\dot{\theta}_{n+\frac{1}{2}}$ = THEONE (I)	Δy^*_1 - DETA	$I_{n+\frac{1}{2}}$ = G(KAY)

FORTRAN PROGRAM FOR THE IBM 7090 COMPUTER

```
DIMENSION STHETA(300), THETA(300), THEONE(300), THETWO(300),
     1ALPHA(300),G(300)
      ALPHA(1)=1.0
      DETA=0.05
      DELETA=0.4
  100 FORMAT(4E15.8)
      READ INPUT TAPE 5,100,(STHETA(I),I=1,201)
  200 FORMAT(I10,5E20.8)
      DO 1000 IJ=1,201,5
      NR=IJ+4
      WRITE OUTPUT TAPE 6,200,IJ,(STHETA(I),I=IJ,NR)
 1000 CONTINUE
      DO 1001 I=1,201
      THETA(I)=ASINF(STHETA(I))
 1001 CONTINUE
      DO 1002 I=2,101
      THEONE(I=1)=(THETA(I)-THETA(I-1))/DETA
 1002 CONTINUE
      DO 1003 I=102,201
      THEONE (I-1)=(THETA(I)-THETA(I-1))/DELETA
 1003 CONTINUE
      DO 1004 I=2,100
      THE TWO (I)=(THEONE(I)-THEONE(I-1))/DETA
 1004 CONTINUE
      DO 1005 I=102,200
      THE TWO(I)=(THEONE(I)-THEONE(I-1))/DELETA
 1005 CONTINUE
      THE TWO(101)=(DELETA*THETWO(100)+DETA*THETWO(102))/
                                              DETA+DELETA)
      DO 1006 I=2,200
      ALPHA(I)=THE TWO(I)*TANF(THETA(I))
 1006 CONTINUE
      SUM = 0.0
      DO 1007 KAY=1,100
      G(KAY)=THEONE(KAY)*THEONE(KAY)+(ALPHA(KAY+1)+
                                              ALPHA(KAY))/2.
      SUM=SUM+G(KAY)*DETA
 1007 CONTINUE
      DO 1008 KAY=101,170
      G(KAY)=THEONE(KAY)*THEONE(KAY)+(ALPHA(KAY+1)+
                                              ALPHA(KAY))/2.
      SUM=SUM+G(KAY)*DELETA
```

```
1008 CONTINUE
     SUM=SUM-THETA(171)*(THEONE(170)+THEONE(171))/2.
 300 FORMAT (10X6HSUM=E15.8)
     WRITE OUTPUT TAPE 6,300,SUM
     CALL EXIT
     END(1,0,0,0,0,0,0,0,0,1,0,0,0,1,0)
```

APPENDIX D

Photographs

Fig. D-1b

Double wall in same film with external field applied (H=13 oe)

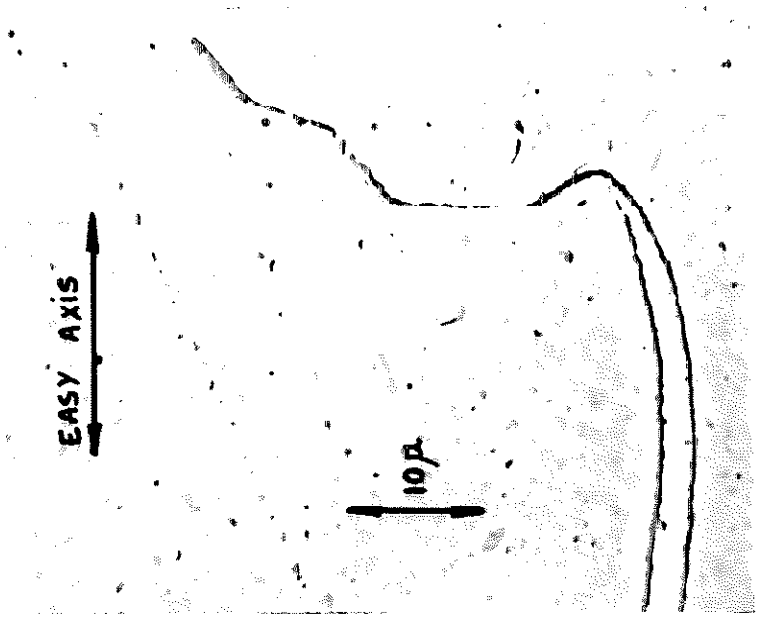

Fig. D-1a

Double wall in a 100 Å film (H= 0)

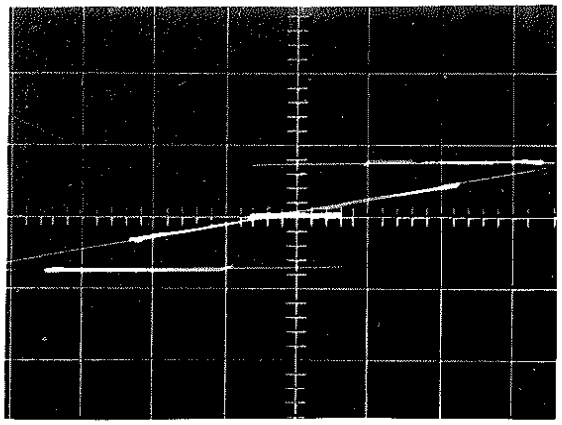

Fig. D-2 Film 1

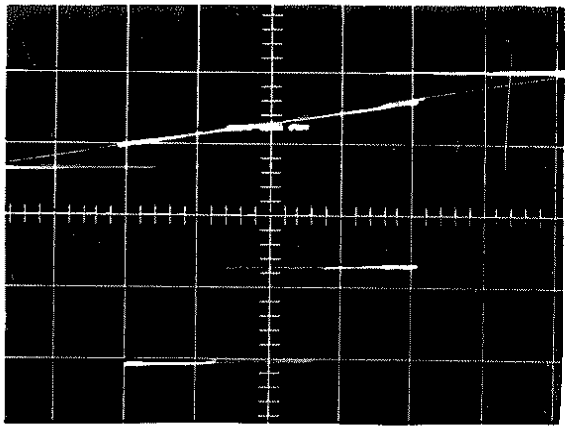

Fig. D-3 Film 2

Horizontal scale : 2 oersteds / division

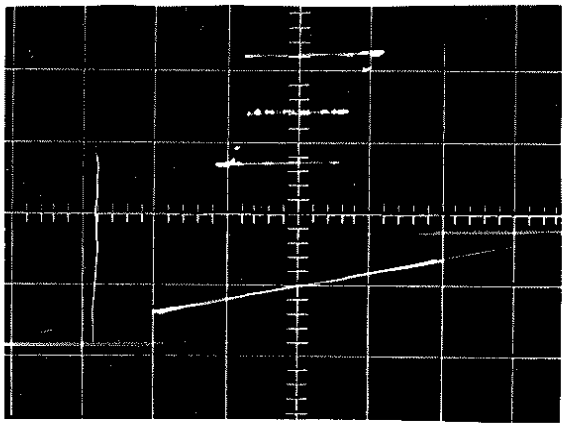

Fig. D-4 Film 3

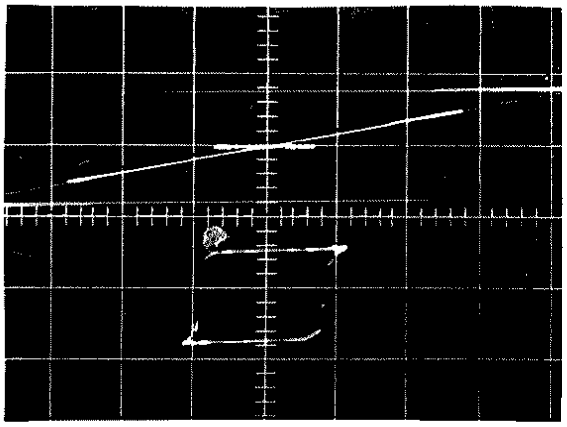

Fig. D-5 Film 4

Films 1, 2, 3, 4 of Table 5-II . The photographs show the hysteresis curves along the easy direction (type "a" and "b" curves of Fig. 5-16) and along the hard direction.

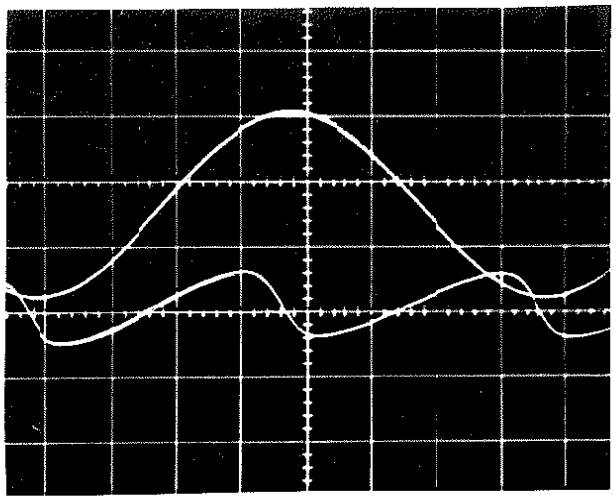

Fig. D-6 Recording of $M \sin(\alpha - \theta)$ in a 150 Å film (70% Ni) . $H \approx 1.5\ H_K$

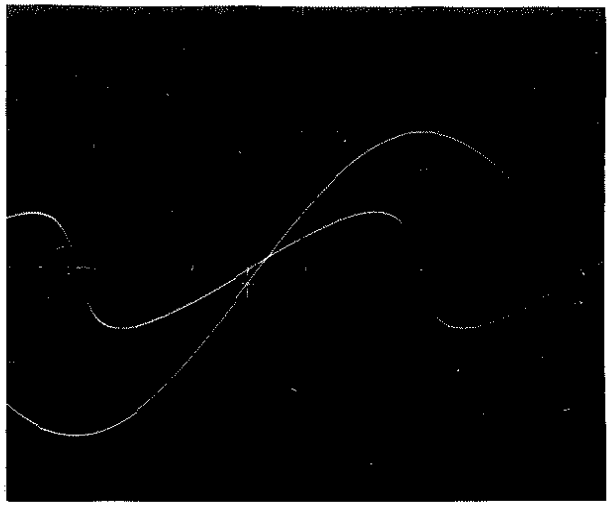

Fig. D-7 Recording of $M \sin(\alpha - \theta)$ in a 1800 Å film (60% Ni) . H=7.4oe (see Table 6-I)

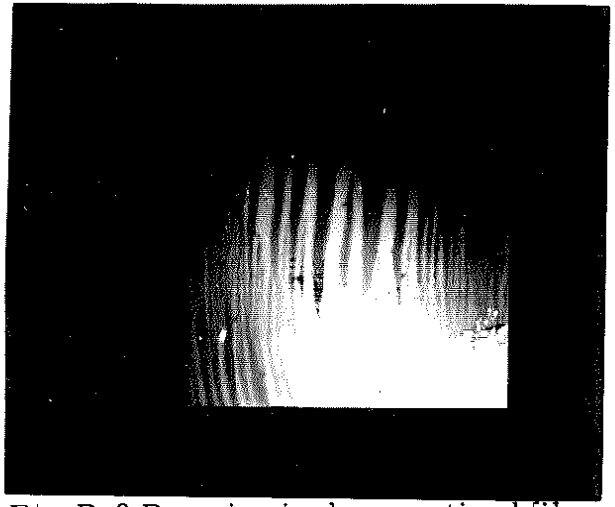

Fig. D-8 Domains in demagnetized film showing dispersion of the easy axis (same film as in Fig. D-7)

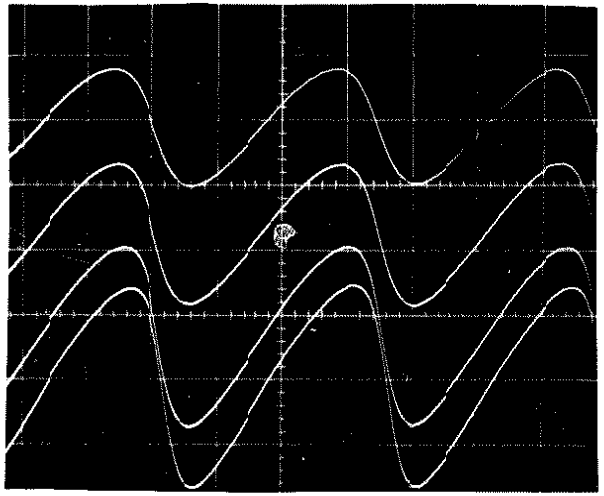

Fig. D-9 Recordings of $M \sin(\alpha - \theta)$ for different values of H in a 53% Ni film (Table 6-III). Amplitude of the calibrating sine wave : 36.5 mm.

REFERENCES

1. Weiss, P., J. Phys. (1907), Vol. 6, p. 661.
2. Bloch, F., Z. Physik (1932), Vol. 74, p. 295.
3. Kittel, C. and Galt, J. K., Solid State Physics (1956), Academic Press, Inc., New York, Vol. 3, pp. 437-564.
4. Blois, M. S., Jr., J. Appl. Phys. (1955), Vol. 26, pp. 975-980.
5. Olson, C. D., and Pohm, A. V., J. Appl. Phys. (1958), Vol. 29, pp. 274-282.
6. Humphrey, F. B. and Gyorgy, E. M., J. Appl. Phys. (1959), Vol. 38, pp. 935-939.
7. Takahashi, M., J. Appl. Phys. (1962), Vol. 33, pp.1101S-1106S.
8. Van Vleck, J. H., Ann. Inst. Henri Poincare (1947), Vol. 10, pp. 57-190.
9. Wolf, I. W., J. Appl. Phys. (1962), Vol. 33, pp. 1152S - 1159S.
10. Goodenough, J. B., and Smith, D. O., Magnetic Properties of Metals and Alloys (1958), American Society for Metals, pp. 112-145.
11. Middelhoek, S., Ferromagnetic Domains in Thin Ni-Fe Films (1961), Doctorate Thesis, University of Amsterdam.
12. Landau, L. and Lifshitz, E., Physik Z. Sowjetunion (1935), Vol. 8, pp. 153-169.
13. Humphrey, F. B. and Johnston, A. R., Rev. Sci. Instr. (1963), Vol. 34, pp. 348-358.

14. Stoner, E. C., and Wohlfahrt, E. P., Phil. Trans. Roy. Soc. London (1948), Vol. A240, pp. 599-643.

15. Smith, D. O., J. Appl. Phys. (1958), Vol. 29, pp. 264-273.

16. Lifshitz, E., J. Phys. USSR (1944), Vol. 8, pp. 337-346.

17. Néel, L., Compt. Rend. (1955), Vol. 421, pp. 533-535.

18. Huber, E. E., Jr., Smith, D. O. and Goodenough, J. G., J. Appl. Phys. (1958), Vol. 29, pp. 294-295.

19. Moon, R. M., J. Appl. Phys. (1959), Vol. 30, pp. 82S-83S.

20. Methfessel, S., Middelhoek, S. and Thomas, H., IBM J. Research Develop. (1960), Vol. 4, pp. 96-106.

21. Thomas, H. and Dietze, H. D., Z. Physik (1961), Vol. 163, pp. 523-534.

22. Fuller, H. W. and Hale, M. E., J. Appl. Phys. (1960), Vol. 31, pp. 1699-1705.

23. Fuchs, E., Z. angew. Physik. (1962), Vol. 14, pp. 203-209

24. Williams, H. J. and Sherwood, R. C , J. Appl. Phys. (1957) Vol. 28, pp. 548-555.

25. Behringer, R. E., J. Appl. Phys. (1958), Vol. 29, pp. 1380-1381.

26. Fuller, H. W., Rubinstein, H. and Sullivan, D. L., J. Appl. Phys. (1961), Vol. 32, pp. 286S - 287S.

27. Feldtkeller, E. and Liesk, W., Z. angew. Physik (1962), Vol. 14, pp. 195-199.

28. Rubinstein, H. and Spain, R. J., J. Appl. Phys. (1960), Vol. 31, pp. 306S-307S.

29. Liesk, W., Z. angew. Physik (1962), Vol. 14, pp. 200-203.

30. Humphrey, F. B., Reynolds, F. W. and Stilwell, G. R., Introduction to Magnetic Thin Films, Vacuum Symposium Transactions (1958), p. 204.

31. Beckerman, M. and Behrndt, K. H., IBM J. Research Develop. (1960), Vol. 4, pp. 198-201.

32. Methfessel, S., Middelhoek, S. and Thomas, H., J. Appl. Phys. Vol. 32, pp. 294S-295S.

33. Schuler, F., Nucleation, Wall Motion and Domain Morphology, (1961), ANIP Report, Servomechanisms Inc., Goleta, Calif.

34. Menyuk, N. and Goodenough, J. B., J. Appl. Phys. (1955), Vol. 26, pp. 8-18.

35. Alexander, R. G., J. Appl. Phys. (1959), Vol. 30, pp. 266S-267S.

36. Rossing, T. D. and Stolen, R., Rev. Sci. Instr. (1961), Vol. 32, pp. 752-753.

37. Bozorth, R. M., Ferromagnetism (1951), D. Van Nostrand Company, New York, p. 556

38. Penoyer, R. F., Rev. Sci. Instr. (1959), Vol. 30, pp. 711-714.

39. Boyd, E. L., IBM J. Research Develop. (1960), Vol. 4, pp. 127-129.